J. Fluid Mech. (2020), *vol.* 884, A10. © Cambridge University Press 2019
doi:10.1017/jfm.2019.909

Nonlinear evolution and acoustic radiation of coherent structures in subsonic turbulent free shear layers

Zhongyu Zhang[1] **and Xuesong Wu**[1,2,†]

[1]Laboratory of High-Speed Aerodynamics, School of Mechanical Engineering, Tianjin University, Tianjin 300072, PR China

[2]Department of Mathematics, Imperial College London, 180 Queen's Gate, London SW7 2AZ, UK

(Received 5 May 2019; revised 24 September 2019; accepted 28 October 2019)

Large-scale coherent structures are present in compressible free shear flows, where they are known to be a main source of aerodynamic noise. Previous studies showed that these structures may be treated as instability waves or wavepackets supported by the underlying turbulent mean flow. By adopting this viewpoint in the framework of triple decomposition of the instantaneous flow into the mean field, coherent motion and small-scale turbulence, a strongly nonlinear dynamical model was constructed to describe the formation and development of coherent structures in incompressible turbulent free shear layers (Wu & Zhuang, *J. Fluid Mech.*, vol. 787, 2016, pp. 396–439). That model is now extended to compressible flows, for which the coherent structures are extracted through a density-weighted (Favre) phase average. The nonlinear non-equilibrium critical-layer theory for instability waves in a laminar compressible mixing layer is adapted to analyse coherent structures in its turbulent counterpart. The strong non-parallelism associated with the fast spreading of the turbulent mean flow is taken into account and found to be significant. The model also accounts for the effect of fine-scale turbulence on coherent structures via a gradient type of closure model which now allows for a phase lag between the phase-averaged small-scale Reynolds stresses and the strain rates of coherent structures. The analysis results in an evolution system comprising of an amplitude equation, the critical-layer temperature and vorticity equations along with the appropriate initial and boundary conditions. The physical processes of acoustic radiation from the coherent structures are described by examining the far-field asymptote of the hydrodynamic fluctuations. We demonstrate that the nonlinearly generated slowly breathing mean-flow distortion radiates low-frequency sound waves. The true physical sources are identified. Equivalent sources in a Lighthill type of acoustic analogy context also arise, but they cannot be fully determined before the acoustic field is calculated, in which sense the radiated sound waves act back on the source. The numerical solutions to the evolution system show that coherent structures attenuate nonlinearly and their vorticity field rolls up to form the characteristic rollers. A study is also made of coherent structures represented by modulated wavetrains consisting of sideband modes, in which case nonlinear interactions generate components with frequencies that are combinations of those of the dominant modes. These components, especially the difference-frequency one, acquire significant amplitudes. Finally, the directivity

† Email address for correspondence: x.wu@imperial.ac.uk

https://doi.org/10.1017/jfm.2019.909 Published online by Cambridge University Press

and spectrum of the emitted acoustic field are calculated for both cases where the coherent structures consist of discrete, and a continuum of, sideband modes.

Key words: jet noise, critical layers, shear layer turbulence

1. Introduction

Coherent structures (CS), which exhibit a high degree of spatial and temporal order, are present in both free and wall-bounded turbulent shear flows (Cantwell 1981; Hussain 1983; Robinson 1991). They play an important role in sustaining turbulence (Hussain & Zaman 1985; Antonia *et al.* 1986), mixing or entrainment of fluids (Dimotakis & Brown 1976; Meyer, Dutton & Lucht 2006) and production of drag and noise (Crow & Champagne 1971; Liu 1974), and as such, have been a subject of extensive investigation for decades. Experimental studies have gathered a great deal of data concerning the kinematic and dynamic properties of CS, which were often extracted from the instantaneous field by suitable statistical means such as the phase average. Several theoretical approaches have been proposed, of which the relatively recent ones are the resolvent analysis and dynamical-system approach. In the former, the instantaneous flow is decomposed into a (locally parallel) mean field and a fluctuating part, and the full Navier–Stokes (N–S) equations are arranged into a 'linearised' form with the nonlinear terms of the fluctuations being treated as forcing (McKeon & Sharma 2010; McKeon 2017). CS are deemed to correspond to the largest possible response, which is calculated by performing singular value decomposition. Obviously, this approach is restricted to stable profiles because otherwise the response would be infinite. The dynamical-system approach seeks exact solutions to the N–S equations, which are of simple equilibrium type, consisting of travelling waves, streamwise vortices and streaks. These solutions are unstable in the full phase space, but form part of the boundary separating the attracting basins of the laminar and turbulent states. They are thought to be visited by, and moreover organise, the trajectories of fully time-dependent motions (Kerswell 2005; Kawahara, Uhlmann & Van Veen 2012). These exact solutions are mostly obtained numerically, but at high Reynolds numbers asymptotic theory can be constructed, providing crucial insight into the physical mechanisms, spatial structures as well as scaling properties (Hall & Sherwin 2010). The mean flow is generated by nonlinear interactions of the wave motion and computed as part of the solution, unlike the resolvent analysis, where the dynamics is primarily linear and the mean flow is prescribed as an input.

Another approach, which appeared much earlier, is based upon 'triple decomposition', namely, splitting the instantaneous flow into three constituents: a time-averaged mean field, a coherent part and small-scale fluctuations (Reynolds & Hussain 1972), and the idea is that CS can be treated as instability modes supported by the mean flow. This approach seems applicable to flows whose mean velocity profiles are inviscidly unstable, such as mixing layers, wakes and jets. CS in these flows were studied by a great number of experimentalists, and the major findings have been reviewed, e.g. by Hussain (1983) and Wygnanski & Petersen (1987), and a fairly detailed summary was given by Wu & Zhuang (2016). In particular, Gaster, Kit & Wygnanski (1985) found that the spatial and temporal characteristics (wavelength, propagation speed and transverse distribution) of CS in a mixing layer were fairly well predicted by linear instability analysis for the mean flow, suggesting that CS

https://doi.org/10.1017/jfm.2019.909 Published online by Cambridge University Press

may be treated as wavepackets of instability modes. The same conclusion was found to hold for CS in plane wakes (Marasli, Champagne & Wygnanski 1989, 1991) and jets (Hussain & Thompson 1980). The presence of CS in turbulent axisymmetric jets was established by the pioneering study of Crow & Champagne (1971), which preceded those on planar free shear layers. The propagation velocity of CS was found to be consistent with the temporal rather than spatial stability analysis of the mean flow modelled simplistically as a vortex sheet. Further hot-wire measurements and flow visualisations were carried out by Hussain & Zaman (1981), Zaman & Hussain (1980) and Hussain & Clark (1981), but the findings were not interpreted from the perspective of instability modes. The more recent experiments (Suzuki & Colonius 2006; Gudmundsson & Colonius 2011; Cavalieri *et al.* 2013) as well as the validated data from large-eddy simulations (Sasaki *et al.* 2017) provided overwhelming evidence supporting the notion of CS as instability modes on the background mean flows.

Once they have acquired a significant amplitude, CS exhibit nonlinear features, the most remarkable of which is the formation of concentrated spanwise vortices or roller structures (Brown & Roshko 1974). It has been found that nonlinear effects come into play near the neutral position (Gudmundsson & Colonius 2011; Cavalieri *et al.* 2013; Tissot *et al.* 2016; Jordan *et al.* 2017), similar to instability modes in laminar flows. Nonlinear interactions of CS generate a mean-flow distortion and harmonics. The former effect was accounted for either by employing the energy equation together with a shape assumption for the transverse distribution of the disturbance (Liu 1989), or by calculating iteratively at each streamwise location the correction to the mean flow and linear instability of the modified mean flow (Cohen, Marasli & Levinski 1994). With the approximations being made on an empirical rather than systematic asymptotic basis, these approaches are of a heuristic nature, but captured some of the observations, including nonlinear saturation of CS and the spreading of the shear-layer thickness. However, none of them can predict vortex roll-up. Wu & Zhuang (2016) noted that an asymptotic theory describing the nonlinear dynamics of CS may be developed from the nonlinear non-equilibrium critical-layer theory for spatially evolving laminar shear flows. The latter describes the continued nonlinear evolution of instability modes when their linear growth becomes diminished, and as a high-Reynolds-number approach is adopted in order to take into account systematically the effects of competing physical factors (nonlinearity, non-equilibrium, viscosity and non-parallelism), a critical layer arises near the transverse position where the mean-flow velocity equals the phase speed of the mode, and nonlinearity as well as viscous and non-equilibrium effects may all become important; a review of the subject was recently given by Wu (2019). For a planar mode in an incompressible mixing layer, Goldstein & Hultgren (1988) and Goldstein & Leib (1989) showed that the dynamics in the critical layer is of a strongly nonlinear nature, due to which all higher-order harmonics are excited simultaneously causing the vorticity field to roll up. This strongly nonlinear critical-layer theory was extended by Sparks & Wu (2008) first to the weakly, and then fully, compressible regimes. It successfully predicts the nonlinear amplitude evolution (Hultgren 1992), and moreover captures roll-up of the vorticity, and in the compressible case, of the temperature field as well. By accounting for both the effects of fine-scale turbulence and strong non-parallelism of the mean flow, Wu & Zhuang (2016) adapted this strongly nonlinear framework to incompressible turbulent free shear layers. The resulting theory reproduces the formation of Brown–Roshko rollers, and the predicted oscillatory saturation of CS is in qualitative, and sometimes quantitative, agreement with experimental measurements.

Experiments indicate that CS exist as well in compressible mixing layers (Papamoschou & Roshko 1988; Clemens *et al.* 1990; Elliott & Samimy 1990;

https://doi.org/10.1017/jfm.2019.909 Published online by Cambridge University Press

Clemens & Mungal 1992), wakes (Scarano & Van Oudheusden 2003) and axisymmetric jets (Thurow, Samimy & Lempert 2003). In the case of mixing layers, compressibility can be characterised by a so-called convective Mach number, M_c. For $M_c < 0.6$, the dynamics appears to be similar to the incompressible case, with the spanwise rollers remaining as the dominant structures (Samimy, Reeder & Elliott 1992; Elliott, Samimy & Arnette 1995), but dominant structures become three-dimensional when $M_c > 0.62$. The convection velocity of CS and the change over to three-dimensional character correlate well with the linear stability of the mean flow (Jackson & Grosch 1989; Ragab & Wu 1989; Sandham & Reynolds 1991). CS structures continue to play a key role in entrainment and mixing (Clemens & Mungal 1995). Experimental studies found that manipulation of CS through controlled excitation led to significant changes to the acoustic far field (Bechert & Pfizenmaier 1975, 1977; Moore 1977), and that the near- and far-field pressure fluctuations were composed of just several low-order azimuthal modes (Fuchs & Michel 1978). All these indicate that CS might be the major source of noise. Since CS are more amenable to theoretical modelling and experimental probing than random fluctuations, it might be possible to predict and control noise through CS (Hussain & Hasan 1985; Zaman 1985; Samimy *et al.* 2010). This attractive prospect has prompted considerable sustained interest and research activities, which resurged recently (Jordan & Colonius 2013).

In order to account for the weak non-parallelism of the mean flow, the approach of linear parabolised stability equations (PSE) has been adopted to describe the development of CS (Gudmundsson & Colonius 2011; Cavalieri *et al.* 2013). Alternatively, linear (bi-)global stability analyses, which include non-parallelism at leading order, have been performed by Nicholas & Lele (2011) and Schmidt *et al.* (2017) for supersonic and high-subsonic jets, respectively. This approach treats the streamwise and transverse variations of the mean flow on the same footing, and thus requires both the upstream and downstream boundary conditions of the computation domain. It is however quite difficult to specify the ones that fully respect the true flow conditions and ensure independency of the solution from the domain size. Only temporally damped global modes have been found. While how such modes represent (or reconcile with) the sustained nature of CS and noise radiation remains to be understood, it is interesting that their spatial structures closely mimic those of the usual Kelvin–Helmholtz (K–H) type of shear instability as well as upstream propagating acoustic modes, and in the supersonic case feature an acoustic field at large radial distances (Schmidt *et al.* 2017). The signatures of K–H and acoustic modes contained in the global modes are of primary physical relevance, but it is unclear presently how the nonlinear nature of K–H modes, which is important for their acoustic radiation, could be taken into account within the global stability approach.

The resolvent analysis approach, developed primarily for CS in exact parallel flows (McKeon & Sharma 2010; Sharma & McKeon 2013), has recently been extended to spatially developing shear flows. Including the non-parallelism at leading order, as in the global stability analysis, Garnaud *et al.* (2013) formulated a global resolvent analysis for an incompressible jet, and this framework was further extended to subsonic jets by Towne *et al.* (2015) and Jeun, Nichols & Jovanović (2016) among others; see the recent review by Cavalieri, Jordan & Lesshafft (2019). The nonlinear terms were treated as a time-harmonic external forcing, and so a linear inhomogeneous boundary-value problem arises. Under the assumption that CS correspond to an 'optimal' response, the problem is converted to one of finding the input, the forcing or initial condition, such that the gain (i.e. output–input ratio) is the largest. The optimal

https://doi.org/10.1017/jfm.2019.909 Published online by Cambridge University Press

response and maximum gain, referred to as the resolvent mode and singular value respectively, are determined by the property of the linear operators, one of which appears in the linearised N–S equations and the other describes the observable output. The resolvent mode contains significant signature of local instability modes. The connection between these two entities was discussed by Beneddine *et al.* (2016), who noted that if the dominant singular value is much greater than others while the forcing does not contain preferentially the subdominant one, then the local instability mode is proportional to the dominant resolvent mode of the same frequency. Tissot *et al.* (2016) presented a local data-driven resolvent formulation, in which the weak non-parallelism is accounted for by using the linear PSE idea, while the forcing is chosen such that the output 'best approximates' the observation.

The physical mechanisms of noise generation by CS continue to be the focus of current investigations. In supersonic shear layers, there exist CS propagating supersonically relative to the ambient flow, and they may radiate Mach waves (Tam 1991). The mechanism is now well understood, and the far-field acoustic wave can be found in terms of the amplitude of the wavepacket representing CS (Tam & Burton 1984; Wu 2005), or via extrapolating the near-field pressure to the far field using the Kirchhoff acoustic surface propagation technique (Sinha *et al.* 2014).

Generation of sound waves in the subsonic regime is however rather different and subtle. Insights into the relations between CS and noise emission were provided by recent studies. Cavalieri *et al.* (2012) found in their experiment that the acoustic field at low polar angles (with respect to the downstream axial direction) is predominantly axisymmetric, and exhibits the so-called superdirectivity. Employing a simplified form of acoustic analogy and modelling the source term by a wavepacket, they calculated the sound, and the prediction was found to be in agreement with the measurements. Instead of examining how CS might radiate sound waves, Kerhervé *et al.* (2012) proposed a statistical estimation methodology and used it to educe, from the measured acoustic field as well as the turbulent flow, the structures primarily responsible for the low-angle sound radiation. These structures turned out to agree rather well with the linear instability modes supported by the mean-flow profile. Fu *et al.* (2017) showed that if CS are removed from the source in Lighthill's acoustic analogy, the resulting noise is substantially reduced.

There has been much effort to characterise the statistical properties of the near-field fluctuations, in terms of which the far-field noise may be expressed. However, statistical analysis in the frequency–wavenumber domain tends to mask noise-emitting events local in time and space. Quite a few investigators therefore turned their attention to temporal-spatial behaviours of the near-field flow and far-field noise with a view of seeking causal relations between the two. Close examinations of experimental and DNS (direct numerical simulation) or LES (large eddy simulation) data reveal that the emission is associated with intermittent events (Juvé, Sunyach & Comte-Bellot 1980; Hileman *et al.* 2005; Cavalieri *et al.* 2010; Kearney-Fischer, Sinha & Samimy 2013). The intermittency may manifest itself as jittering, or spatial-temporal modulation, which is controlled by nonlinear effects. The role of jittering has been assessed mainly in the framework of the acoustic analogy. When jittering was introduced, on a phenomenological basis, to the phase speed or envelope of the wavepack modelling the source, the radiated sound increased (Ffowcs Williams & Kempton 1978; Cavalieri *et al.* 2011). The same effect occurs when coherence decay, which is a statistical measure of jittering, is introduced to the source model in the spectral domain (Goldstein 1984; Cavalieri & Agarwal 2014; Baqui *et al.* 2015). Among important flow events, vortex pairing had long been considered as one that

https://doi.org/10.1017/jfm.2019.909 Published online by Cambridge University Press

radiates substantial noise (e.g. Kibens 1980). However, subsequent studies found that this was the case only at low Reynolds numbers, and in practical situations breakdown of CS (axisymmetric ring vortices in circular jets, or Brown–Roshko rollers in mixing layers) appears to be the dominant source (Bridges & Hussain 1987, 1992; Samimy *et al.* 2010; Crawley *et al.* 2018). Despite the ever expanding literature, the causal relations between CS and the emitted sound remain elusive.

The aim of the present paper is, first of all, to investigate the nonlinear evolution of CS in a subsonic turbulent mixing layer. We shall pursue this goal in the simple framework of local stability, the reason being that even though global and resolvent modes can be computed (at higher costs), it is primarily the signatures of local convective unstable modes that are of direct relevance for physical understanding. These local modes are more amiable to theoretical and computational treatments, and equally importantly they possess the key attribute observed of CS being directly related to external disturbances (such as acoustic noise or turbulence in the oncoming flow), and the link between them could be understood in terms of receptivity mechanisms near the nozzle or the trailing edge of the splitter plate. The present theoretical development will be based on the previous work on nonlinear instability of a compressible laminar shear layer (Sparks & Wu 2008), and on CS in an incompressible turbulent mixing layer (Wu & Zhuang 2016). The ensuing analysis amounts to extending either the former to the CS in a turbulent shear flow, or the latter to the compressible regime. Moreover, the CS are taken to be a spatially and temporally modulated wavetrain, which is a more realistic representation of the actual disturbances, and more importantly would radiate low-frequency sound waves.

The second aim of the present paper is to investigate acoustic radiation of the CS. Several previous studies employed acoustic analogy with the corresponding sources being modelled in terms of wavepackets to calculate the sound field. Sandham, Morfey & Hu (2006) and Sandham & Salgado (2008) used the Lilley–Goldstein analogy, in which the sources are 'nonlinear', being the products of the fluctuations. With the fluctuations being represented by linearly evolving instability waves, the resulting source component with difference wavenumber or frequency was found to generate the dominant sound wave. Cheung & Lele (2009) showed that when the fluctuation is represented by nonlinearly developing instability modes, acoustic radiation becomes much stronger. Cavalieri *et al.* (2011) and Cavalieri & Agarwal (2014) opted for Lighthill's analogy, in which linear and nonlinear sources appear in general. They focussed on the linear source only while neglecting the nonlinear ones. The predictions based on acoustic analogy captured some key features of acoustic fields. However, this methodology does not probe the true physical process of sound emission, the precise mechanism of which remains unexplained. Our goal is to describe, on the basis of first principles, why and how the CS emit sound waves, using the asymptotic approach to aeroacoustics, which was first introduced by Crow (1970) for low-Mach-number flows. In this approach, sound radiation is treated as a singular perturbation problem with the acoustic field being determined by analysing the far-field asymptotic behaviour of the hydrodynamic fluctuations. Unlike the acoustic analogy, there is no need to pre-designate the 'sound field' and its 'source' since they identify themselves unequivocally in the course of the analysis. As further developments and applications, the mechanism and mathematical theory of the noise generated by linear unstable supersonic modes were proposed by Tam & Burton (1984), and the radiations by nonlinear unstable modes in supersonic and subsonic jets were presented by Wu (2005) and Wu & Huerre (2009) respectively. The approach has also been applied to acoustic radiation from instability waves in boundary layers by Wu & Hogg (2006) and Wu (2011).

https://doi.org/10.1017/jfm.2019.909 Published online by Cambridge University Press

The acoustic radiations mentioned above take place in laminar flows. In this paper, a theory for the acoustic radiation by subsonic CS in a turbulent mixing layer will be developed. A wave propagating subsonically relative to the ambient mean flow is completely quiescent if it undergoes no spatial modulation. When modulated in space, it does radiate sound waves of the same frequency directly through a linear mechanism, as has been shown by Crighton & Huerre (1990) for a model problem and by Tam & Morris (1980) for a mixing layer; see also Cavalieri *et al.* (2012). The sound waves emitted are rather weak, and concentrate in the small angles to the streamwise direction. A nonlinear and stronger radiation occurs if the wave undergoes simultaneous spatial and temporal modulation. The nonlinear interactions of the waves (or rather wavepackets) then generate components with difference wavenumbers/frequencies, which may radiate effectively (Sandham & Salgado 2008; Suponitsky, Sandham & Morfey 2010). More generally, these components can be considered as part of the nonlinearly induced mean-flow distortion, which varies slowly in both time and space, radiating low-frequency noise to the far field. Such a mechanism has been demonstrated for a pair of subsonic helical modes on a laminar circular jet (Wu & Huerre 2009). A broadly similar mechanism operates with the two-dimensional CS in a turbulent mixing layer, but significant differences arise in the characters of both the nonlinear dynamics and radiation.

The rest of the paper is organised as follows. In § 2, CS are separated from the instantaneous flow field through triple decomposition. Their governing equations are obtained with the aid of a closure model for the coherent Reynolds stresses of small-scale fluctuations. In § 3, on the assumption that a CS can be represented by a wavepacket, we consider its nonlinear dynamics in the streamwise region where the linear growth rate is vanishingly small. Suitable scales are introduced, and the asymptotic analysis is performed for the main shear layer and the critical layer to derive a strongly nonlinear evolution system. In § 4, this evolution system is summarised, and appropriate initial and boundary conditions are deduced for the cases where the wavepacket consists of discrete and continuous sidebands. By examining the far-field behaviour of CS, we show in § 5 how CS emit sound waves. The actual sound emitter is found to be the nonlinearly generated unsteady mean-flow distortion, which radiates low-frequency sound waves. Calculations are carried out for a typical mean-flow velocity profile in § 6, and numerical calculations are presented in three parts: (a) CS with a single frequency; (b) CS consisting of discrete sidebands; (c) the sound waves radiated by modulated CS with discrete and continuous sidebands. Finally, a summary and discussion are given in § 7.

2. Formulation

2.1. *Governing equations and flow decomposition*

To fix the idea, we consider a typical compressible mixing layer, which is formed due to two streams merging downstream of a splitter plate. The velocity and temperature in the fast stream are denoted by U_1^* and T_1^*, and those in the slow stream by U_2^* and T_2^*, respectively. We introduce the Cartesian coordinates (x^*, y^*), where x^* and y^* denote the distances in the streamwise and transverse directions respectively. The coordinates (x^*, y^*) and time t^* are non-dimensionalised by a reference length δ_0^* and time δ_0^*/U_0^*, where the superscript * signifies a dimensional quantity, δ_0^* denotes the thickness of the shear layer at a typical position and U_0^* is a reference velocity. The velocity U^*, density ρ^*, temperature T^* and viscosity μ^* are normalised respectively by

$$U_0^* = (U_1^* - U_2^*)/2, \quad \rho_0^* = \rho_1^*, \quad T_0^* = T_1^*, \quad \mu_0^* = \mu_1^*, \tag{2.1a–d}$$

while the non-dimensional pressure p is introduced by writing $p^* = p_0^* + \rho_0^* U_0^{*2} p$.

https://doi.org/10.1017/jfm.2019.909 Published online by Cambridge University Press

The resulting dimensionless parameters, including the Mach number Ma, the Reynolds number Re and the Prandtl number Pr, are defined as

$$Ma = U_0^*/\sqrt{\gamma R_g^* T_0^*}, \quad Re = \rho_0^* U_0^* \delta_0^*/\mu_0^*, \quad Pr = \mu_0^* C_p^*/k_0^*, \tag{2.2a–c}$$

where R_g^* is the universal gas constant, k_0^* its thermal conductivity and $\gamma = C_p/C_v$ is the ratio of the constant-pressure and constant-volume specific heat capacities, C_p and C_v. The non-dimensional compressible Navier–Stokes (N–S) equations for a perfect gas can be written as (in the tensor form),

$$\frac{\partial \rho}{\partial t} + \frac{\partial \rho u_i}{\partial x_i} = 0, \tag{2.3}$$

$$\rho \frac{\partial u_i}{\partial t} + \rho u_j \frac{\partial u_i}{\partial x_j} = -\frac{\partial p}{\partial x_i} + \frac{1}{Re}\frac{\partial}{\partial x_j}\left[\mu\left(\frac{\partial u_i}{\partial x_j} + \frac{\partial u_j}{\partial x_i}\right) - \frac{2}{3}\mu \frac{\partial u_k}{\partial x_k}\delta_{ij}\right], \tag{2.4}$$

$$\rho \frac{\partial T}{\partial t} + \rho u_i \frac{\partial T}{\partial x_i} = (\gamma - 1)Ma^2\left(\frac{\partial p}{\partial t} + u_i \frac{\partial p}{\partial x_i}\right) + \frac{1}{PrRe}\frac{\partial}{\partial x_i}\mu \frac{\partial T}{\partial x_i} + \frac{(\gamma - 1)Ma^2}{Re}\Phi, \tag{2.5}$$

$$\rho T = 1 + \gamma Ma^2 p, \tag{2.6}$$

where the dissipation function Φ is

$$\Phi = \frac{\mu}{2}\left(\frac{\partial u_i}{\partial x_j} + \frac{\partial u_j}{\partial x_i}\right)\left(\frac{\partial u_i}{\partial x_j} + \frac{\partial u_j}{\partial x_i}\right) - \frac{2\mu}{3}\left(\frac{\partial u_i}{\partial x_i}\right)^2. \tag{2.7}$$

As a first step towards a mathematical formulation for the nonlinear evolution of CS in a mixing layer, the instantaneous field $(\boldsymbol{u}, T, p, \rho, \mu)$ is decomposed into the mean flow $(\bar{\boldsymbol{U}}, \bar{T}, \bar{P}, \bar{\rho}, \bar{\mu})$, the quasi-periodic coherent motion $(\tilde{\boldsymbol{u}}, \tilde{T}, \tilde{p}, \tilde{\rho}, \tilde{\mu})$ and the remaining fluctuations $(\boldsymbol{u}', T', p', \rho', \mu')$, which are predominately small scale (so that energy cascade takes place among components in this part) (Hussain & Reynolds 1972; Wu & Zhuang 2016),

$$(\boldsymbol{u}, T, p, \rho, \mu) = (\bar{\boldsymbol{U}}, \bar{T}, \bar{P}, \bar{\rho}, \bar{\mu}) + (\tilde{\boldsymbol{u}}, \tilde{T}, \tilde{p}, \tilde{\rho}, \tilde{\mu}) + (\boldsymbol{u}', T', p', \rho', \mu'), \tag{2.8}$$

where an overbar over p, ρ and μ denotes a time-averaged quantity

$$\bar{f}(\boldsymbol{x}, t) \equiv \lim_{\tau \to \infty} \frac{1}{\tau}\int_t^{t+\tau} f(\boldsymbol{x}, t^\star)\,\mathrm{d}t^\star, \tag{2.9}$$

whereas the velocity $\bar{\boldsymbol{U}}$ and temperature $\bar{T}$ denote the Favre time average,

$$\bar{f}(\boldsymbol{x}, t) \equiv \frac{1}{\bar{\rho}} \lim_{\tau \to \infty} \frac{1}{\tau}\int_t^{t+\tau} \rho f(\boldsymbol{x}, t^\star)\,\mathrm{d}t^\star, \tag{2.10}$$

which is necessary for compressible turbulent flows; for statistically stationary flows, $\bar{f}$ is independent of t. Owing to their quasi-cyclic property, CS may be extracted by the phase average (Hussain & Reynolds 1970)

$$\langle f \rangle(\boldsymbol{x}, t) \equiv \lim_{N \to \infty} \frac{1}{N}\sum_{i=1}^{N} f(\boldsymbol{x}, t + \tau_i), \tag{2.11}$$

https://doi.org/10.1017/jfm.2019.909 Published online by Cambridge University Press

for $\tilde{p}$, $\tilde{\rho}$ and $\tilde{\mu}$, whereas for $\tilde{\boldsymbol{u}}$ and $\tilde{T}$ the Favre phase average is defined as

$$\langle f\rangle(\boldsymbol{x},t)\equiv\frac{1}{\langle\rho\rangle}\lim_{N\to\infty}\frac{1}{N}\sum_{i=1}^{N}\rho f(\boldsymbol{x},t+\tau_i),\tag{2.12}$$

where τ_i denotes the time lapse between the instants at which the structure is considered to have the same phase as at time t (Hussain & Reynolds 1970; Hussain 1983). The decomposition is primarily targeted at flows which exhibit a discernible period τ_0, or are excited by harmonic forcing, in which case $\tau_i=i\tau_0$. The signature of CS, $\tilde{f}$, is then obtained by $\tilde{f}\equiv\langle f\rangle-\bar{f}$. The large- and small-scale fluctuations are assumed to be uncorrelated, i.e. $\overline{\tilde{f}g'}=0$.

2.2. *Mean-flow equations*

The time-averaged mean flow is driven by the Reynolds stresses contributed by both the coherent and small-scale fluctuations. Unlike the conventional treatment, here we regard $\bar{U}$, $\bar{V}$, $\bar{T}$, $\bar{P}$, $\bar{\rho}$ and $\bar{\mu}$ as being driven only by the Reynolds stresses from small-scale eddies. This is realised by treating the mean-flow distortion caused by CS as a part of CS themselves (cf. Wu & Zhuang 2016).

It is generally accepted that direct effects of density fluctuations on turbulence are small at free-stream Mach numbers less than approximately 5 (Bradshaw 1977). For subsonic cases, we can omit the correlations about ρ'. After taking the time average, or Favre time average, of (2.3)–(2.6), the mean flow field in two dimensions is found to satisfy the Reynolds-averaged equations (Schlichting 1979),

$$\frac{\partial\bar{\rho}}{\partial t}+\frac{\partial\bar{\rho}\bar{U}}{\partial x}+\frac{\partial\bar{\rho}\bar{V}}{\partial y}=0,\tag{2.13}$$

$$\begin{aligned}&\bar{\rho}\frac{\partial\bar{U}}{\partial t}+\bar{\rho}\bar{U}\frac{\partial\bar{U}}{\partial x}+\bar{\rho}\bar{V}\frac{\partial\bar{U}}{\partial y}-\frac{2}{3Re}\frac{\partial}{\partial x}\bar{\mu}\left(2\frac{\partial\bar{U}}{\partial x}-\frac{\partial\bar{V}}{\partial y}\right)-\frac{1}{Re}\frac{\partial}{\partial y}\bar{\mu}\left(\frac{\partial\bar{U}}{\partial y}+\frac{\partial\bar{V}}{\partial x}\right)\\&\quad=-\frac{\partial\bar{P}}{\partial x}+\frac{\partial\bar{\tau}^{\dagger}_{11}}{\partial x}+\frac{\partial\bar{\tau}^{\dagger}_{12}}{\partial y}+\text{H.O.T.},\end{aligned}\tag{2.14}$$

$$\begin{aligned}&\bar{\rho}\frac{\partial\bar{V}}{\partial t}+\bar{\rho}\bar{U}\frac{\partial\bar{V}}{\partial x}+\bar{\rho}\bar{V}\frac{\partial\bar{V}}{\partial y}-\frac{2}{3Re}\frac{\partial}{\partial y}\bar{\mu}\left(2\frac{\partial\bar{V}}{\partial y}-\frac{\partial\bar{U}}{\partial x}\right)-\frac{1}{Re}\frac{\partial}{\partial x}\bar{\mu}\left(\frac{\partial\bar{U}}{\partial y}+\frac{\partial\bar{V}}{\partial x}\right)\\&\quad=-\frac{\partial\bar{P}}{\partial y}+\frac{\partial\bar{\tau}^{\dagger}_{21}}{\partial x}+\frac{\partial\bar{\tau}^{\dagger}_{22}}{\partial y}+\text{H.O.T.},\end{aligned}\tag{2.15}$$

$$\begin{aligned}&\bar{\rho}\frac{\partial\bar{T}}{\partial t}+\bar{\rho}\bar{U}\frac{\partial\bar{T}}{\partial x}+\bar{\rho}\bar{V}\frac{\partial\bar{T}}{\partial y}-\frac{1}{PrRe}\left(\frac{\partial}{\partial x}\bar{\mu}\frac{\partial\bar{T}}{\partial x}+\frac{\partial}{\partial y}\bar{\mu}\frac{\partial\bar{T}}{\partial y}\right)\\&\quad=(\gamma-1)Ma^2\left(\frac{\partial\bar{P}}{\partial t}+\bar{U}\frac{\partial\bar{P}}{\partial x}+\bar{V}\frac{\partial\bar{P}}{\partial y}\right)+(\gamma-1)Ma^2\left[\overline{u'\frac{\partial p'}{\partial x}}+\overline{v'\frac{\partial p'}{\partial y}}\right]\\&\qquad+\frac{\partial\bar{\tau}^{\dagger}_{T1}}{\partial x}+\frac{\partial\bar{\tau}^{\dagger}_{T2}}{\partial y}+\frac{(\gamma-1)Ma^2}{Re}(\bar{\Phi}+\bar{\Phi}')+\text{H.O.T.},\end{aligned}\tag{2.16}$$

$$\bar{\rho}\bar{T}=1+\gamma Ma^2\bar{P},\tag{2.17}$$

https://doi.org/10.1017/jfm.2019.909 Published online by Cambridge University Press

where $\bar{\tau}_{ij}^{\dagger}$ and $\bar{\tau}_{Ti}^{\dagger}$ denote the Reynolds stress and energy flux, respectively, and

$$\left.\begin{aligned}\bar{\Phi} &= \frac{4}{3}\bar{\mu}\left[\frac{\partial \bar{U}}{\partial x}\frac{\partial \bar{U}}{\partial x}+\frac{\partial \bar{V}}{\partial y}\frac{\partial \bar{V}}{\partial y}-\frac{\partial \bar{U}}{\partial x}\frac{\partial \bar{V}}{\partial y}\right]+\bar{\mu}\left[\frac{\partial \bar{U}}{\partial y}\frac{\partial \bar{U}}{\partial y}+\frac{\partial \bar{V}}{\partial x}\frac{\partial \bar{V}}{\partial x}-\frac{\partial \bar{U}}{\partial y}\frac{\partial \bar{V}}{\partial x}\right],\\ \bar{\Phi}' &= \frac{4}{3}\bar{\mu}\left[\overline{\frac{\partial u'}{\partial x}\frac{\partial u'}{\partial x}}+\overline{\frac{\partial v'}{\partial y}\frac{\partial v'}{\partial y}}-\overline{\frac{\partial u'}{\partial x}\frac{\partial v'}{\partial y}}\right]+\bar{\mu}\left[\overline{\frac{\partial u'}{\partial y}\frac{\partial u'}{\partial y}}+\overline{\frac{\partial v'}{\partial x}\frac{\partial v'}{\partial x}}-\overline{\frac{\partial u'}{\partial y}\frac{\partial v'}{\partial x}}\right].\end{aligned}\right\} \tag{2.18}$$

The fact that large-scale CS are influenced by the upstream and boundary conditions means that their Reynolds stresses cannot be well characterised by the local mean-flow strain rate with an eddy viscosity coefficient. Now with CS and their Reynolds stresses being treated separately and explicitly, a closure model needs to be introduced for the (Favre-) time-averaged Reynolds stresses of small-scale fluctuations, which depend primarily on local conditions and thus may be less troublesome to model. A simple gradient type of model may be adopted here, which is written (in the tensor form with the Kronecker delta δ_{ij}) as

$$\bar{\tau}_{Ti}^{\dagger} = -\overline{\rho u_i' T'} = \frac{\mu_t}{Pr_T R_T}\frac{\partial \bar{T}}{\partial x_i}, \tag{2.19}$$

$$\bar{\tau}_{ij}^{\dagger} = -\overline{\rho u_i' u_j'} = -\frac{1}{3}\overline{\rho u_k' u_k'}\delta_{ij}+\frac{\mu_t}{R_T}\left(\frac{\partial \bar{U}_i}{\partial x_j}+\frac{\partial \bar{U}_j}{\partial x_i}-\frac{2}{3}\frac{\partial \bar{U}_k}{\partial x_k}\delta_{ij}\right), \tag{2.20}$$

where μ_t is the mean eddy viscosity normalised by its reference value $\mu_{t,0}^*$. The turbulent Reynolds number R_T and Prandtl number Pr_T are defined as

$$R_T = \rho_0^* U_0^* \delta_0^*/\mu_{t,0}^*, \quad Pr_T = C_p^* \mu_{t,0}^*/k_{t,0}^*, \tag{2.21a,b}$$

with $k_{t,0}^*$ being the dimensional mean eddy conductivity. The term $\overline{u_i' \partial_{x_i} p'}$ in (2.16) is modelled by following Van Driest (1951). After using the momentum equations for u_i' to eliminate the pressure gradient, and making the same approximations as that in Van Driest (1951), we have the model

$$\overline{u_i'\frac{\partial p'}{\partial x_i}} = -\overline{\rho u_i' u_j'}\frac{\partial \bar{U}_i}{\partial x_j} = \bar{\tau}_{ij}^{\dagger}\frac{\partial \bar{U}_i}{\partial x_j}. \tag{2.22}$$

The molecular viscosity μ is usually a function of temperature, i.e. $\mu = \mu(T)$, and thus the temperature fluctuation causes a molecular viscosity fluctuation μ'. The time-averaged Reynolds stresses due to μ' are relegated into higher-order terms represented by H.O.T. in (2.14)–(2.16), since they are small (Bradshaw 1977), here of $O[(R_T Re)^{-1}]$ (which is $O(\epsilon^{5/2})$ with the scalings to be introduced in § 3.1), and likewise the resulting phase-averaged (coherent) Reynolds stresses are much smaller than those caused by velocity fluctuations, and so will be relegated into the higher-order terms represented by h.o.t. in (2.24)–(2.26).

2.3. *Equations for coherent structures*

Substituting (2.8) into (2.3)–(2.6), and performing the phase average or the Favre-phase average, followed by subtracting out (2.13)–(2.17) respectively, we obtain the equations governing CS,

$$\frac{\partial \tilde{\rho}}{\partial t}+\frac{\partial \tilde{\rho}\bar{U}}{\partial x}+\frac{\partial \tilde{\rho}\bar{V}}{\partial y}+\frac{\partial \rho u}{\partial x}+\frac{\partial \rho v}{\partial y} = 0, \tag{2.23}$$

https://doi.org/10.1017/jfm.2019.909 Published online by Cambridge University Press

$$\rho\frac{\partial u}{\partial t}+\rho\bar{U}\frac{\partial u}{\partial x}+\rho\bar{V}\frac{\partial u}{\partial y}+\rho u\frac{\partial \bar{U}}{\partial x}+\rho v\frac{\partial \bar{U}}{\partial y}+\rho u\frac{\partial u}{\partial x}+\rho v\frac{\partial u}{\partial y}+\tilde{\rho}\bar{U}\frac{\partial \bar{U}}{\partial x}+\tilde{\rho}\bar{V}\frac{\partial \bar{U}}{\partial y}$$
$$=-\frac{\partial p}{\partial x}+\frac{\partial \tilde{\tau}_{11}^{\dagger}}{\partial x}+\frac{\partial \tilde{\tau}_{12}^{\dagger}}{\partial y}+\frac{2}{3Re}\frac{\partial}{\partial x}\mu\left(2\frac{\partial u}{\partial x}-\frac{\partial v}{\partial y}\right)+\frac{1}{Re}\frac{\partial}{\partial y}\mu\left(\frac{\partial u}{\partial y}+\frac{\partial v}{\partial x}\right)$$
$$+\frac{2}{3Re}\frac{\partial}{\partial x}\tilde{\mu}\left(2\frac{\partial \bar{U}}{\partial x}-\frac{\partial \bar{V}}{\partial y}\right)+\frac{1}{Re}\frac{\partial}{\partial y}\tilde{\mu}\left(\frac{\partial \bar{U}}{\partial y}+\frac{\partial \bar{V}}{\partial x}\right)+\text{h.o.t.}, \tag{2.24}$$

$$\rho\frac{\partial v}{\partial t}+\rho\bar{U}\frac{\partial v}{\partial x}+\rho\bar{V}\frac{\partial v}{\partial y}+\rho u\frac{\partial \bar{V}}{\partial x}+\rho v\frac{\partial \bar{V}}{\partial y}+\rho u\frac{\partial v}{\partial x}+\rho v\frac{\partial v}{\partial y}+\tilde{\rho}\bar{U}\frac{\partial \bar{V}}{\partial x}+\tilde{\rho}\bar{V}\frac{\partial \bar{V}}{\partial y}$$
$$=-\frac{\partial p}{\partial y}+\frac{\partial \tilde{\tau}_{21}^{\dagger}}{\partial x}+\frac{\partial \tilde{\tau}_{22}^{\dagger}}{\partial y}+\frac{2}{3Re}\frac{\partial}{\partial y}\mu\left(2\frac{\partial v}{\partial y}-\frac{\partial u}{\partial x}\right)+\frac{1}{Re}\frac{\partial}{\partial x}\mu\left(\frac{\partial u}{\partial y}+\frac{\partial v}{\partial x}\right)$$
$$+\frac{2}{3Re}\frac{\partial}{\partial y}\tilde{\mu}\left(2\frac{\partial \bar{V}}{\partial y}-\frac{\partial \bar{U}}{\partial x}\right)+\frac{1}{Re}\frac{\partial}{\partial x}\tilde{\mu}\left(\frac{\partial \bar{U}}{\partial y}+\frac{\partial \bar{V}}{\partial x}\right)+\text{h.o.t.}, \tag{2.25}$$

$$\rho\frac{\partial T}{\partial t}+\rho\bar{U}\frac{\partial T}{\partial x}+\rho\bar{V}\frac{\partial T}{\partial y}+\rho u\frac{\partial \bar{T}}{\partial x}+\rho v\frac{\partial \bar{T}}{\partial y}+\rho u\frac{\partial T}{\partial x}+\rho v\frac{\partial T}{\partial y}+\tilde{\rho}\bar{U}\frac{\partial \bar{T}}{\partial x}+\tilde{\rho}\bar{V}\frac{\partial \bar{T}}{\partial y}$$
$$=(\gamma-1)Ma^2\left(\frac{\partial p}{\partial t}+\bar{U}\frac{\partial p}{\partial x}+\bar{V}\frac{\partial p}{\partial y}+u\frac{\partial \bar{P}}{\partial x}+v\frac{\partial \bar{P}}{\partial y}+u\frac{\partial p}{\partial x}+v\frac{\partial p}{\partial y}\right)$$
$$+\frac{1}{PrRe}\left(\frac{\partial}{\partial x}\mu\frac{\partial T}{\partial x}+\frac{\partial}{\partial y}\mu\frac{\partial T}{\partial y}\right)+\frac{1}{PrRe}\left(\frac{\partial}{\partial x}\tilde{\mu}\frac{\partial \bar{T}}{\partial x}+\frac{\partial}{\partial y}\tilde{\mu}\frac{\partial \bar{T}}{\partial y}\right)+\frac{\partial \tilde{\tau}_{T1}^{\dagger}}{\partial x}+\frac{\partial \tilde{\tau}_{T2}^{\dagger}}{\partial y}$$
$$+(\gamma-1)Ma^2\bowtie\left[u'\frac{\partial p'}{\partial x}+v'\frac{\partial p'}{\partial y}\right]+\frac{(\gamma-1)Ma^2}{Re}(\tilde{\Phi}+\tilde{\Phi}')+\text{h.o.t.}, \tag{2.26}$$

$$\rho T+\tilde{\rho}\bar{T}=\gamma Ma^2 p, \tag{2.27}$$

where $\tilde{\tau}_{ij}^{\dagger}=\bowtie[\rho u_i'u_j']$ and $\tilde{\tau}_{Ti}^{\dagger}=\bowtie[\rho u_i'T']$ represent the phase-averaged Reynolds stresses of small-scale velocity and temperature fluctuations with the operator '$\bowtie$' being defined as

$$\bowtie[f(t)]\equiv-[\langle f(t)\rangle-\overline{f(t)}]; \tag{2.28}$$

in (2.26), $\tilde{\Phi}$ and $\tilde{\Phi}'$ denote the dissipation functions associated with CS and small-scale motions respectively,

$$\left.\begin{aligned}\tilde{\Phi}=\mu\Bigg\{&\frac{4}{3}\left[\frac{\partial u}{\partial x}\frac{\partial u}{\partial x}+\frac{\partial v}{\partial y}\frac{\partial v}{\partial y}+2\frac{\partial \bar{U}}{\partial x}\frac{\partial u}{\partial x}+2\frac{\partial \bar{V}}{\partial y}\frac{\partial v}{\partial y}-\frac{\partial \bar{U}}{\partial x}\frac{\partial v}{\partial y}\right.\\&\left.-\frac{\partial \bar{V}}{\partial y}\frac{\partial u}{\partial x}-\frac{\partial u}{\partial x}\frac{\partial v}{\partial y}\right]\\&+\left[\frac{\partial v}{\partial x}\frac{\partial v}{\partial x}+\frac{\partial u}{\partial y}\frac{\partial u}{\partial y}+2\frac{\partial \bar{V}}{\partial x}\frac{\partial v}{\partial x}+2\frac{\partial \bar{V}}{\partial x}\frac{\partial u}{\partial y}+2\frac{\partial \bar{U}}{\partial y}\frac{\partial v}{\partial x}\right.\\&\left.+2\frac{\partial \bar{U}}{\partial y}\frac{\partial u}{\partial y}+2\frac{\partial v}{\partial x}\frac{\partial u}{\partial y}\right]\Bigg\},\\\tilde{\Phi}'=\mu\bowtie\Bigg[&\frac{4}{3}\frac{\partial u'}{\partial x}\frac{\partial u'}{\partial x}+\frac{4}{3}\frac{\partial v'}{\partial y}\frac{\partial v'}{\partial y}+\frac{\partial v'}{\partial x}\frac{\partial v'}{\partial x}+\frac{\partial u'}{\partial y}\frac{\partial u'}{\partial y}+\frac{4}{3}\frac{\partial u'}{\partial x}\frac{\partial v'}{\partial y}+\frac{8}{3}\frac{\partial v'}{\partial x}\frac{\partial u'}{\partial y}\Bigg].\end{aligned}\right\} \tag{2.29}$$

https://doi.org/10.1017/jfm.2019.909 Published online by Cambridge University Press

For brevity, we have omitted the $\tilde{}$ over u, v, T and p, the quantities representing CS. However, ρ and μ will denote the sums of the time-averaged density and molecular viscosity and the coherent density and viscosity fluctuations, i.e. $\rho = \bar{\rho} + \tilde{\rho}$ and $\mu = \bar{\mu} + \tilde{\mu}$.

The system (2.23)–(2.27) needs to be closed by introducing a suitable model for $\tilde{\tau}_{ij}^{\dagger}$ and $\tilde{\tau}_{Ti}^{\dagger}$, the coherent (phase-averaged) Reynolds stresses of small-scale turbulence. They are related to the strain rate of CS by a gradient type of model with a time delay, i.e.

$$\tilde{\tau}_{Ti}^{\dagger} = \frac{\tilde{\mu}_t}{\tilde{Pr}_T \tilde{R}_T} \frac{\partial T}{\partial x_i}(t - \hat{\tau}_1, \boldsymbol{x}), \quad \tilde{\tau}_{ij}^{\dagger} = \frac{\tilde{\mu}_t}{\tilde{R}_T} \left(\frac{\partial u_i}{\partial x_j} + \frac{\partial u_j}{\partial x_i} - \frac{2}{3} \frac{\partial u_k}{\partial x_k} \delta_{ij} \right) (t - \hat{\tau}_2, \boldsymbol{x}), \quad (2.30a,b)$$

where $\tilde{\mu}_t$, normalised by its reference value $\tilde{\mu}_{t,0}^*$, is the coherent eddy viscosity, accounting for the impact of fine-scale turbulence on CS, and the dimensionless parameters, $\tilde{R}_T$ and $\tilde{Pr}_T$, are defined as

$$\tilde{R}_T = \rho_0^* U_0^* \delta_0^* / \tilde{\mu}_{t,0}^*, \quad \tilde{Pr}_T = C_p^* \tilde{\mu}_{t,0}^* / \tilde{k}_{t,0}^*, \quad (2.31a,b)$$

with $\tilde{k}_{t,0}^*$ being the dimensional coherent eddy conductivity. A model of this type was introduced by Wu & Zhou (1989) for CS in incompressible boundary layers. Here, we generalise it to a compressible mixing layer, and allow for two time delays, $\hat{\tau}_1$ and $\hat{\tau}_2$. The concept of eddy viscosity was introduced by drawing analogy between 'random eddy motions' and molecular collisions, which give rise to molecular viscosity. However, small-scale fluctuations have a much longer time scale than that of molecular collisions, and so do not adjust instantaneously to the local conditions of the large-scale CS (Wu & Zhou 1989). It appears reasonable to expect that the momentum and energy fluxes carried by small-scale turbulence lag behind the strain rate and temperature gradient of the CS, respectively. As it will transpire in § 4.3, when the governing equations are transformed to spectral space, complex eddy conductivity and viscosity coefficients will appear. Following Van Driest (1951), we obtain the model for the phase-averaged quantity,

$$\left\langle u_i' \frac{\partial p'}{\partial x_i} \right\rangle = -\langle \rho u_i' u_j' \rangle \left(\frac{\partial \bar{U}_i}{\partial x_j} + \frac{\partial u_i}{\partial x_j} \right). \quad (2.32)$$

It follows from (2.22) and (2.32) that

$$\bowtie \left[u_i' \frac{\partial p'}{\partial x_i} \right] = \bar{\tau}_{ij}^{\dagger} \frac{\partial u_i}{\partial x_j} + \tilde{\tau}_{ij}^{\dagger} \frac{\partial \bar{U}_i}{\partial x_j} + \tilde{\tau}_{ij}^{\dagger} \frac{\partial u_i}{\partial x_j}. \quad (2.33)$$

The effect of the above term turns out to be negligible for the problem considered in the present paper.

3. Asymptotic theory for strongly nonlinear critical layers

3.1. *Asymptotic scalings*

The equations governing CS are now applied to a compressible free shear layer. As a first step, we specify the appropriate scalings both in the streamwise and normal directions (figure 1). A CS is represented by a modulated wavepacket of an instability mode. Our focus is on the region where the mode is nearly neutral and

https://doi.org/10.1017/jfm.2019.909 Published online by Cambridge University Press

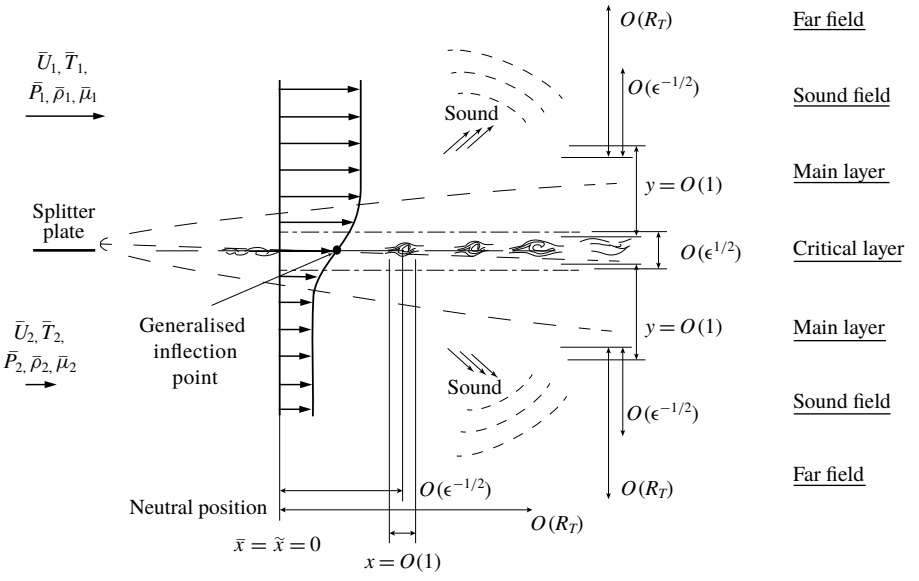

FIGURE 1. Asymptotic structures and scalings in both the streamwise and transverse directions.

thus prone to nonlinear effects. In the main part of the flow, the CS can be written as

$$\epsilon A^{\dagger}(\tau, \bar{x})\hat{q}(y)\mathrm{e}^{\mathrm{i}\alpha\zeta} + \text{c.c.} \quad \text{with } \zeta = x - ct, \tag{3.1}$$

where $\alpha, c = O(1)$ are the wavenumber and phase speed of the locally neutral mode respectively, $\epsilon \ll 1$ is a measure of its magnitude, $\hat{q}(y)$ characterises its transverse distribution and $A^{\dagger}$ is its amplitude with the slow spatial and time variables, $\bar{x}$ and τ, to be defined below.

The mode representing the CS has a critical layer located at a generalised inflection point. As in Sparks & Wu (2008) and Wu & Zhuang (2016), our interest is in its dynamics in the strongly nonlinear and non-equilibrium regime. Suppose that the critical-layer thickness is of $O(l_\mu)$ with $l_\mu \ll 1$ to be fixed. The nonlinear effect, mainly from $v\partial/(\partial y) = O(\epsilon/l_\mu)$, is required to balance the $O(l_\mu)$ non-equilibrium effect, leading to

$$l_\mu = \epsilon^{1/2}. \tag{3.2}$$

The disturbance undergoes temporal and spatially modulation, which is described by the slow time and streamwise variables (cf. Wu & Tian 2012),

$$\tau = l_\mu t, \quad \bar{x} = l_\mu x/c. \tag{3.3a,b}$$

The introduction of temporal modulation means that the CS consists of discrete, or a continuum of, sideband spectra adjacent to the main carrier-wave component. Such spectral content arises because naturally present disturbances exciting the CS are unlikely to be purely monochromatic. When nonlinear effects come into play, the resulting energy transfer among different spectral components causes significant intermittency or jittering (Wu & Tian 2012), which is known to be important in the radiation of sound waves.

https://doi.org/10.1017/jfm.2019.909 Published online by Cambridge University Press

For $\bar{x} = O(1)$, the nonlinear effect as well as the effects of conductivities and viscosities all appear at leading order in the critical layer, if we choose the scalings as,

$$Re^{-1} = \bar{\lambda} l_\mu^3 = \bar{\lambda}\epsilon^{3/2}, \quad \tilde{R}_T^{-1} = \tilde{\lambda} l_\mu^3 = \tilde{\lambda}\epsilon^{3/2}, \tag{3.4a,b}$$

where $\bar{\lambda}$, $\tilde{\lambda} = O(1)$ are the Haberman (1972) parameters. Furthermore, the non-parallelism is to appear at leading order, if we set $R_T \sim Re^{2/3}$ (cf. Wu & Zhuang 2016), which can be expressed as

$$\sigma R_T = Re^{2/3} \quad \text{with } \sigma = O(1). \tag{3.5}$$

Note that $Re \gg R_T \gg 1$, which is reasonable since the eddy viscosity is much greater than the molecular viscosity. We re-scale the vertical velocity as $R_T^{-1}\bar{V}$, so that the mean flow field can be written as $(\bar{U},\ R_T^{-1}\bar{V},\ \bar{T},\ \bar{P},\ \bar{\rho},\ \bar{\mu})$, and it develops in the streamwise direction on the slow streamwise variable

$$\tilde{x} = x/R_T. \tag{3.6}$$

Clearly, $\tilde{x}$ and $\bar{x}$ have the relationship $\tilde{x} = \epsilon^{1/2}\sigma\bar{\lambda}^{2/3}c\bar{x}$.

With the aid of the closure model (2.19)–(2.20) and (2.22), equations (2.13)–(2.14) and (2.16) reduce to (cf. Van Driest 1951)

$$\frac{\partial \bar{\rho}\bar{U}}{\partial \tilde{x}} + \frac{\partial \bar{\rho}\bar{V}}{\partial y} = 0, \tag{3.7}$$

$$\bar{\rho}\bar{U}\frac{\partial \bar{U}}{\partial \tilde{x}} + \bar{\rho}\bar{V}\frac{\partial \bar{U}}{\partial y} = \frac{\partial}{\partial y}\mu_t\frac{\partial \bar{U}}{\partial y}, \tag{3.8}$$

$$\bar{\rho}\bar{U}\frac{\partial \bar{T}}{\partial \tilde{x}} + \bar{\rho}\bar{V}\frac{\partial \bar{T}}{\partial y} = \frac{1}{Pr_T}\frac{\partial}{\partial y}\mu_t\frac{\partial \bar{T}}{\partial y} + (\gamma-1)Ma^2\mu_t\frac{\partial \bar{U}}{\partial y}\frac{\partial \bar{U}}{\partial y}. \tag{3.9}$$

The velocity and temperature profiles of the mean flow near $\tilde{x} = 0$ (the neutral point) can be Taylor expanded as,

$$\begin{bmatrix}\bar{U}(\tilde{x}, y)\\ \bar{T}(\tilde{x}, y)\end{bmatrix} = \begin{bmatrix}\bar{U}(0, y)\\ \bar{T}(0, y)\end{bmatrix} + \epsilon^{1/2}\begin{bmatrix}\bar{U}_1(y)\\ \bar{T}_1(y)\end{bmatrix}\bar{x} + \frac{1}{2}\epsilon\begin{bmatrix}\bar{U}_2(y)\\ \bar{T}_2(y)\end{bmatrix}\bar{x}^2 + \cdots, \tag{3.10a,b}$$

where

$$(\bar{U}_n, \bar{T}_n) = (\sigma\bar{\lambda}^{2/3}c)^n\left(\frac{\partial^n \bar{U}}{\partial \tilde{x}^n}, \frac{\partial^n \bar{T}}{\partial \tilde{x}^n}\right)\bigg|_{\tilde{x}=0}. \tag{3.11}$$

When analysing the critical layer, a thin layer at the generalised inflection point y_c, it is necessary to introduce a local transverse (inner) variable,

$$Y = (y - y_c)/l_\mu = (y - y_c)/\epsilon^{1/2}. \tag{3.12}$$

In the critical layer, the mean-flow profiles can be further expanded about y_c as,

$$\begin{aligned}\begin{bmatrix}\bar{U}(\bar{x}, Y)\\ \bar{T}(\bar{x}, Y)\end{bmatrix} &= \begin{pmatrix}\bar{U}_c\\ \bar{T}_c\end{pmatrix} + \epsilon^{1/2}\left[\begin{pmatrix}\bar{U}_{1,c}\\ \bar{T}_{1,c}\end{pmatrix}\bar{x} + \begin{pmatrix}\bar{U}'_c\\ \bar{T}'_c\end{pmatrix}Y\right]\\ &\quad + \frac{1}{2}\epsilon\left[\begin{pmatrix}\bar{U}_{2,c}\\ \bar{T}_{2,c}\end{pmatrix}\bar{x}^2 + 2\begin{pmatrix}\bar{U}'_{1,c}\\ \bar{T}'_{1,c}\end{pmatrix}\bar{x}Y + \begin{pmatrix}\bar{U}''_c\\ \bar{T}''_c\end{pmatrix}Y^2\right] + \cdots.\end{aligned} \tag{3.13}$$

https://doi.org/10.1017/jfm.2019.909 Published online by Cambridge University Press

Moreover, in order to describe acoustic radiation and non-parallelism, a sound-field variable $\bar{y}$ and a far-field variable $\tilde{y}$,

$$\bar{y} = l_\mu y/c = \epsilon^{1/2} y/c, \quad \tilde{y} = y/R_T \tag{3.14a,b}$$

have to be introduced, as will be explained in § 5.3 and § 6.1, respectively. The asymptotic structure of the flow is shown in figure 1. In the streamwise direction, the mean flow develops over the $O(R_T)$ distances, while the perturbation evolves nonlinearly over an $O(\epsilon^{-1/2})$ length. In the transverse direction, there exist four regions: the main layer with $y = O(1)$, the critical layer where $Y = O(1)$, the acoustic region where $\bar{y} = O(1)$ and the inviscid region of the mean flow where $\tilde{y} = O(1)$. An analysis will be performed for each of them, of which the most important is the critical layer, where nonlinearity, viscosity, non-equilibrium and non-parallelism all play leading roles. The asymptotic matching is between $Y \to \pm\infty$ and $y \to 0^{\pm}$, $y \to \pm\infty$ and $\bar{y} \to 0^{\pm}$ for the perturbation as well as between $y \to \pm\infty$ and $\tilde{y} \to 0^{\pm}$ for the mean flow.

3.2. *Outer expansions in the main shear layer*

In the main part of the shear layer, the perturbation is a travelling wave, modulated in both time and space. The carrier wave is described by the fast variable $\zeta = x - ct$, representing the coordinate moving at the phase speed of the wave. The temporal-spatial modulation is described by the amplitude function $A^{\dagger}(\tau, \bar{x})$. The molecular viscosity μ has no contribution in this region up to $O(\epsilon^{5/2})$, namely the main layer is inviscid in our analysis. Let $\tilde{q}$ represent any of u, v, T, p, $\tilde{\rho}$ or $\tilde{\mu}$. The solution can be expressed as an asymptotic series,

$$\begin{aligned}\tilde{q} \;=\; & \epsilon A^{\dagger}(\tau, \bar{x})\hat{q}_0(y)\mathrm{e}^{\mathrm{i}\alpha\zeta} + \epsilon^{3/2}\sum_{m=1}^{\infty}\hat{q}_1^{\langle m\rangle}(\tau, \bar{x}, y)\mathrm{e}^{\mathrm{i}m\alpha\zeta} \\ & + \epsilon^2\sum_{m=0}^{\infty}\hat{q}_2^{\langle m\rangle}(\tau, \bar{x}, y)\mathrm{e}^{\mathrm{i}m\alpha\zeta} + \text{c.c.} + \cdots .\end{aligned} \tag{3.15}$$

Inserting (3.15) into (2.23)–(2.27), at $O(\epsilon)$ we obtain,

$$\mathrm{i}\alpha\hat{u}_0 + \hat{v}_0' + \mathrm{i}\alpha Ma^2(\bar{U} - c)\hat{p}_0 = 0, \tag{3.16}$$

$$\mathrm{i}\alpha(\bar{U} - c)\hat{u}_0 + \bar{U}'\hat{v}_0 + \mathrm{i}\alpha\bar{T}\hat{p}_0 = 0, \tag{3.17}$$

$$\mathrm{i}\alpha(\bar{U} - c)\hat{v}_0 + \bar{T}\hat{p}_0' = 0, \tag{3.18}$$

$$\mathrm{i}\alpha(\bar{U} - c)\hat{T}_0 + \bar{T}'\hat{v}_0 - \mathrm{i}\alpha(\gamma - 1)Ma^2\bar{T}(\bar{U} - c)\hat{p}_0 = 0, \tag{3.19}$$

$$\hat{T}_0 + \bar{T}^2\hat{\rho}_0 - \gamma Ma^2\bar{T}\hat{p}_0 = 0, \tag{3.20}$$

where the prime represents the differentiation with respect to y. Elimination of $\hat{u}_0$ and $\hat{v}_0$ from (3.16)–(3.20) leads to the compressible Rayleigh equation with the boundary conditions,

$$\mathcal{L}\hat{p}_0 = 0; \quad \hat{p}_0 \to 0 \quad \text{as } y \to \pm\infty, \tag{3.21}$$

where $\mathcal{L}$ is the Rayleigh operator, defined as

$$\mathcal{L} \equiv \frac{\mathrm{d}^2}{\mathrm{d}y^2} + \left[\frac{\bar{T}'}{\bar{T}} - \frac{2\bar{U}'}{\bar{U} - c}\right]\frac{\mathrm{d}}{\mathrm{d}y} + \alpha^2\left[\frac{Ma^2(\bar{U} - c)^2}{\bar{T}} - 1\right]. \tag{3.22}$$

https://doi.org/10.1017/jfm.2019.909 Published online by Cambridge University Press

The eigenvalue problem (3.21) determines unstable modes with $O(1)$ growth rates, but the critical layer has to be considered for nearly neutral modes. The solution for the velocities $\hat{u}_0$ and $\hat{v}_0$, the density $\hat{\rho}_0$ and temperature $\hat{T}_0$ can be expressed in terms of $\hat{p}_0$; see appendix A.

The Rayleigh equation is singular at the critical level $y = y_c$, where $\bar{U}(y_c) = c$. Near y_c, an asymptotic solution can be found for $\hat{p}_0$ (cf. Goldstein & Leib 1989; Leib 1991),

$$\hat{p}_0 = \frac{\bar{U}_c'}{\bar{T}_c}\left[\pi_1(\alpha;\hat{y}) + \frac{1}{3}\alpha^2\left(b_1 + \frac{\bar{U}_c''}{2\bar{U}_c'}\right)\pi_2(\alpha;\hat{y})\right], \tag{3.23}$$

where $\hat{y} \equiv y - y_c \to 0$,

$$\left.\begin{gathered}\pi_1(\alpha;\hat{y}) = 1 - \tfrac{1}{2}\alpha^2\hat{y}^2 + a_4\hat{y}^4 + O(\hat{y}^6), \quad \pi_2(\alpha;\hat{y}) = \hat{y}^3 + O(\hat{y}^5), \\ a_4 = \frac{1}{4}\alpha^2\left[\frac{\bar{T}_c''}{\bar{T}_c} - \frac{2\bar{U}_c'''}{3\bar{U}_c'} - \frac{\bar{T}_c'^2}{2\bar{T}_c^2} - \frac{1}{2}\alpha^2 - \frac{Ma^2\bar{U}_c'^2}{\bar{T}_c}\right],\end{gathered}\right\} \tag{3.24}$$

and b_1 is a constant to be determined by solving (3.21) globally. Inserting (3.23) into (3.17)–(3.19), we obtain,

$$\hat{u}_0 = -b_1 - e_1\hat{y} + O(\hat{y}^2), \tag{3.25}$$

$$\hat{v}_0 = -\mathrm{i}\alpha[1 - b_1\hat{y} - \tfrac{1}{2}(e_1 - Ma^2\bar{U}_c'^2/\bar{T}_c)\hat{y}^2] + O(\hat{y}^3), \tag{3.26}$$

$$\hat{T}_0 = \frac{\bar{T}_c'}{\bar{U}_c'}\frac{1}{\hat{y}} + \frac{1}{\bar{U}_c'}\left[\bar{T}_c'' - \bar{T}_c'b_1 - \frac{\bar{T}_c'^2}{2\bar{T}_c} + (\gamma-1)Ma^2\bar{U}_c'^2\right] + O(\hat{y}), \tag{3.27}$$

with

$$e_1 = \frac{\bar{T}_c''}{\bar{T}_c} + b_1\frac{\bar{T}_c'}{\bar{T}_c} - \frac{\bar{U}_c'''}{\bar{U}_c'} - \alpha^2 - \frac{Ma^2\bar{U}_c'^2}{\bar{T}_c}. \tag{3.28}$$

At $O(\epsilon^{3/2})$, we obtain,

$$\mathrm{i}\alpha\hat{u}_1^{\langle1\rangle} + \hat{v}_1^{\langle1\rangle\prime} + Ma^2\mathrm{i}\alpha(\bar{U}-c)\hat{p}_1^{\langle1\rangle} = -Ma^2\hat{p}_0(\mathcal{D}_1A^\dagger + \mathrm{i}\alpha\bar{U}_1\bar{x}A^\dagger) - c^{-1}\hat{u}_0\frac{\partial A^\dagger}{\partial\bar{x}}, \tag{3.29}$$

$$\begin{aligned}&\mathrm{i}\alpha(\bar{U}-c)\hat{u}_1^{\langle1\rangle} + \bar{U}'\hat{v}_1^{\langle1\rangle} + \mathrm{i}\alpha\bar{T}\hat{p}_1^{\langle1\rangle} \\ &\quad= -\hat{u}_0(\mathcal{D}_1A^\dagger + \mathrm{i}\alpha\bar{U}_1\bar{x}A^\dagger) - \bar{U}_1'\hat{v}_0\bar{x}A^\dagger - c^{-1}\bar{T}\hat{p}_0\frac{\partial A^\dagger}{\partial\bar{x}} - \mathrm{i}\alpha\bar{T}_1\hat{p}_0\bar{x}A^\dagger,\end{aligned} \tag{3.30}$$

$$\mathrm{i}\alpha(\bar{U}-c)\hat{v}_1^{\langle1\rangle} + \bar{T}\hat{p}_1^{\langle1\rangle\prime} = -\hat{v}_0(\mathcal{D}_1A^\dagger + \mathrm{i}\alpha\bar{U}_1\bar{x}A^\dagger) - \bar{T}_1\hat{p}_0'\bar{x}A^\dagger, \tag{3.31}$$

$$\begin{aligned}&\mathrm{i}\alpha(\bar{U}-c)\hat{T}_1^{\langle1\rangle} + \bar{T}'\hat{v}_1^{\langle1\rangle} - \mathrm{i}\alpha(\gamma-1)Ma^2\bar{T}(\bar{U}-c)\hat{p}_1^{\langle1\rangle} \\ &\quad= -\hat{T}_0(\mathcal{D}_1A^\dagger + \mathrm{i}\alpha\bar{U}_1\bar{x}A^\dagger) - \bar{T}_1'\hat{v}_0\bar{x}A^\dagger \\ &\qquad+ (\gamma-1)Ma^2(\bar{T}\hat{p}_0\mathcal{D}_1A^\dagger + \mathrm{i}\alpha\bar{T}_1\hat{p}_0'\bar{x}A^\dagger),\end{aligned} \tag{3.32}$$

$$\hat{T}_1^{\langle1\rangle} + \bar{T}^2\hat{\rho}_1^{\langle1\rangle} - \gamma Ma^2\bar{T}\hat{p}_1^{\langle1\rangle} = (\hat{T}_0 - \bar{T}^2\hat{\rho}_0)\bar{T}^{-1}\bar{T}_1\bar{x}A^\dagger, \tag{3.33}$$

where the operator $\mathcal{D}_1$ is defined as

https://doi.org/10.1017/jfm.2019.909 Published online by Cambridge University Press

$$\mathcal{D}_1(y) \equiv \frac{\partial}{\partial \tau} + \frac{\bar{U}(y)}{c}\frac{\partial}{\partial \bar{x}}. \tag{3.34}$$

Eliminating $\hat{u}_1^{\langle 1\rangle}$, $\hat{v}_1^{\langle 1\rangle}$ and $\hat{T}_1^{\langle 1\rangle}$ from (3.29)–(3.33), we obtain the inhomogeneous Rayleigh equation for $\hat{p}_1^{\langle 1\rangle}$ (cf. Wu 2005),

$$\mathcal{L}\hat{p}_1^{\langle 1\rangle} = -\frac{2\mathrm{i}}{\alpha c}(\mathcal{G}_{11}\hat{p}_0' + \alpha^2\mathcal{G}_{12}\hat{p}_0)\frac{\partial A^\dagger}{\partial \bar{x}} + \frac{2\mathrm{i}}{\alpha}(\mathcal{G}_{21}\hat{p}_0' + \alpha^2\mathcal{G}_{22}\hat{p}_0)\mathcal{D}_0 A^\dagger - (\mathcal{G}_{01}\hat{p}_0' + \alpha^2\mathcal{G}_{02}\hat{p}_0)\bar{x}A^\dagger, \tag{3.35}$$

with its boundary conditions that $\hat{p}_1^{\langle 1\rangle} \to 0$ as $y \to \pm\infty$, where

$$\left.\begin{gathered}
\mathcal{D}_0 \equiv \mathcal{D}_1(y_c) = \frac{\partial}{\partial \tau} + \frac{\partial}{\partial \bar{x}}; \\
\mathcal{G}_{11} = 0, \quad \mathcal{G}_{12} = 1 - \frac{Ma^2(\bar{U}-c)^2}{\bar{T}}; \quad \mathcal{G}_{21} = \frac{\bar{U}'}{(\bar{U}-c)^2}, \quad \mathcal{G}_{22} = \frac{Ma^2(\bar{U}-c)}{\bar{T}}; \\
\mathcal{G}_{01} = \frac{2[\bar{U}_1\bar{U}' - (\bar{U}-c)\bar{U}_1']}{(\bar{U}-c)^2} - \frac{\bar{T}'\bar{T}_1 - \bar{T}\bar{T}_1'}{\bar{T}^2}, \\
\mathcal{G}_{02} = \frac{Ma^2(\bar{U}-c)}{\bar{T}^2}[2\bar{U}_1\bar{T} - (\bar{U}-c)\bar{T}_1].
\end{gathered}\right\} \tag{3.36}$$

By the method of variation of parameter, the solution for $\hat{p}_1^{\langle 1\rangle}$ can be found, in terms of $\hat{p}_0$, as

$$\hat{p}_1^{\langle 1\rangle} = C_1^{\langle 1\rangle}(\tau, \bar{x})\hat{p}_0 + C_2^{\langle 1\rangle\pm}(\tau, \bar{x})\hat{p}_{00} - \frac{2\mathrm{i}}{\alpha c}\frac{\partial A^\dagger}{\partial \bar{x}}K_1 + \frac{2\mathrm{i}}{\alpha}\mathcal{D}_0 A^\dagger K_2 - \bar{x}A^\dagger K_0, \tag{3.37}$$

where the '$\pm$' signs refer to $y > y_c$ and $y < y_c$ respectively, and

$$\hat{p}_{00}(\hat{y}) = \hat{p}_0\int_0^{\hat{y}} \frac{(\bar{U}-c)^2}{\bar{T}\hat{p}_0^2}\,\mathrm{d}\hat{y}^\star, \quad K_j(\hat{y}) = \hat{p}_0\int_0^{\hat{y}} \frac{(\bar{U}-c)^2}{\bar{T}\hat{p}_0^2}\tilde{J}_j(\hat{y}^\star)\,\mathrm{d}\hat{y}^\star, \tag{3.38a,b}$$

with

$$\tilde{J}_j(\hat{y}) = \fint_{-\infty}^{\hat{y}} \frac{\bar{T}}{(\bar{U}-c)^2}(\mathcal{G}_{j1}\hat{p}_0'\hat{p}_0 + \alpha^2\mathcal{G}_{j2}\hat{p}_0^2)\,\mathrm{d}\hat{y}^\star \quad (j = 0, 1, 2), \tag{3.39}$$

whereas $C_1^{\langle 1\rangle}$ and $C_2^{\langle 1\rangle\pm}$ are arbitrary. Obviously, $\tilde{J}_j$ may be hyper-singular integrals when the integral interval contains $y = y_c$, and must be defined in the sense of Hadamard finite part; see § 6.2 for the details of their calculation.

In order for $\hat{p}_1^{\langle 1\rangle}$ to satisfy the boundary conditions, it is necessary to set

$$C_2^{\langle 1\rangle -} = 0, \quad C_2^{\langle 1\rangle +} = \frac{2\mathrm{i}}{\alpha c}J_1\frac{\partial A^\dagger}{\partial \bar{x}} - \frac{2\mathrm{i}}{\alpha}J_2\mathcal{D}_0 A^\dagger + J_0\bar{x}A^\dagger, \tag{3.40a,b}$$

where we have put

$$J_j = \tilde{J}_j(\infty) = \fint_{-\infty}^{\infty} \frac{\bar{T}}{(\bar{U}-c)^2}(\mathcal{G}_{j1}\hat{p}_0'\hat{p}_0 + \alpha^2\mathcal{G}_{j2}\hat{p}_0^2)\,\mathrm{d}\hat{y} \quad (j = 0, 1, 2). \tag{3.41}$$

https://doi.org/10.1017/jfm.2019.909 Published online by Cambridge University Press

On the other hand, near y_c (i.e. $\hat{y}\to 0$), we have the asymptotic solution to (3.35),

$$\begin{aligned}\hat{p}_1^{\langle 1\rangle} \;\to\; & d_1^{\langle 1\rangle}(\tau,\bar{x})\pi_1(\alpha;\hat{y}) + d_2^{\langle 1\rangle\pm}(\tau,\bar{x})\pi_2(\alpha;\hat{y}) \\ & + \left(\frac{\mathrm{i}\alpha}{\bar{T}_c}\mathcal{D}_0 A^\dagger - \frac{\alpha^2\bar{U}_{1,c}}{\bar{T}_c}\bar{x}A^\dagger\right)\left[\hat{y} - \left(b_1 + \frac{\bar{U}_c''}{2\bar{U}_c'}\right)\hat{y}^2 + \frac{1}{3}j\hat{y}^3\ln|\hat{y}|\right] \\ & + \frac{\mathrm{i}\alpha\bar{U}_c'}{c\bar{T}_c}\frac{\partial A^\dagger}{\partial\bar{x}}\hat{y}^2 + \frac{\alpha^2\bar{U}_c'}{3\bar{T}_c}j_1\bar{x}A^\dagger\hat{y}^3\ln|\hat{y}| + O(\hat{y}^4\ln|\hat{y}|) \quad \text{as } \hat{y}\to 0, \end{aligned} \tag{3.42}$$

in which

$$j = \left(\frac{\bar{T}_c''}{\bar{T}_c} - \frac{\bar{T}_c'^2}{\bar{T}_c^2}\right) - \left(\frac{\bar{U}_c'''}{\bar{U}_c'} - \frac{\bar{U}_c''^2}{\bar{U}_c'^2}\right), \quad j_1 = \frac{\bar{T}_c'}{\bar{T}_c}\left(\frac{\bar{T}_{1,c}'}{\bar{T}_c'} - \frac{\bar{T}_{1,c}}{\bar{T}_c}\right) - \frac{\bar{U}_c''}{\bar{U}_c'}\left(\frac{\bar{U}_{1,c}''}{\bar{U}_c''} - \frac{\bar{U}_{1,c}'}{\bar{U}_c'}\right). \tag{3.43a,b}$$

In the limit $\hat{y}\to 0$, the general solution (3.37) must have the same behaviour as (3.42). Taking the limit $\hat{y}\to 0$ of (3.37) and using the asymptotic behaviour of $\hat{p}_0$, we have,

$$d_1^{\langle 1\rangle} = (\bar{U}_c'/\bar{T}_c)C_1^{\langle 1\rangle}, \tag{3.44}$$

$$\begin{aligned} d_2^{\langle 1\rangle\pm} \;=\; & \frac{\bar{U}_c'}{3}\left[\frac{\alpha^2}{\bar{T}_c}\left(b_1 + \frac{\bar{U}_c''}{2\bar{U}_c'}\right)C_1^{\langle 1\rangle} + C_2^{\langle 1\rangle\pm}\right. \\ & \left. - \tilde{J}_1(0)\frac{2\mathrm{i}}{\alpha c}\frac{\partial A^\dagger}{\partial\bar{x}} + \tilde{J}_2(0)\frac{2\mathrm{i}}{\alpha}\mathcal{D}_0 A^\dagger - \tilde{J}_0(0)\bar{x}A^\dagger\right]. \end{aligned} \tag{3.45}$$

Obviously, $C_1^{\langle 1\rangle}(\tau,\bar{x})$ remains undetermined, but we could treat $(A^\dagger + \epsilon^{1/2}C_1^{\langle 1\rangle})$ as one entity, which is equivalent to re-defining the amplitude function $A^\dagger$.

For the boundary-value problem (3.35) to have a solution, a solvable condition must be satisfied, which follows from multiplying (3.35) by $\bar{T}\hat{p}_0/(\bar{U}-c)^2$ and performing integration by parts on the left-hand side. After these steps, we obtain

$$-\frac{3}{\bar{U}_c'}(d_2^{\langle 1\rangle+} - d_2^{\langle 1\rangle-}) = \frac{2\mathrm{i}}{\alpha}J_2\frac{\partial A^\dagger}{\partial\tau} - \frac{2\mathrm{i}}{\alpha}\left(\frac{J_1}{c} - J_2\right)\frac{\partial A^\dagger}{\partial\bar{x}} - J_0\bar{x}A^\dagger. \tag{3.46}$$

The solution for the velocities $\hat{u}_1$ and $\hat{v}_1$, the density $\hat{\rho}_1$ and temperature $\hat{T}_1$ can be expressed in terms of $\hat{p}_0$ and $\hat{p}_1$ as shown in appendix A. In order to find the relation between the jump $(d_2^{\langle 1\rangle+} - d_2^{\langle 1\rangle-})$ and the jump in the relevant flow quantity, the asymptotic solutions for $\hat{u}_1^{\langle 1\rangle}$, $\hat{v}_1^{\langle 1\rangle}$ and $\hat{T}_1^{\langle 1\rangle}$ near $\hat{y}=0$ are worked out as follows,

$$\begin{aligned}\hat{u}_1^{\langle 1\rangle} \;\to\; & \left[-\frac{\mathrm{i}}{\alpha\bar{U}_c'}j\mathcal{D}_0 - \left(j_1 - \frac{\bar{U}_{1,c}}{\bar{U}_c'}j\right)\bar{x}\right]A^\dagger\ln|\hat{y}| \\ & + \left(e_2\mathcal{D}_0 A^\dagger + e_3\bar{x}A^\dagger - \frac{3\bar{T}_c}{\alpha^2\bar{U}_c'}d_2^{\langle 1\rangle\pm}\right) + O(\hat{y}\ln|\hat{y}|), \end{aligned} \tag{3.47}$$

$$\hat{v}_1^{\langle 1\rangle} \;\to\; \left[\left(\frac{b_1}{\bar{U}_c'} + \frac{\bar{U}_c''}{2\bar{U}_c'^2}\right)(\mathcal{D}_0 + \mathrm{i}\alpha\bar{U}_{1,c}\bar{x})A^\dagger - \frac{\partial A^\dagger}{c\partial\bar{x}} + \frac{\mathrm{i}\alpha\bar{U}_{1,c}'}{\bar{U}_c'}\bar{x}A^\dagger - \frac{\mathrm{i}\alpha\bar{T}_c}{\bar{U}_c'}d_1^{\langle 1\rangle}\right]$$

https://doi.org/10.1017/jfm.2019.909 Published online by Cambridge University Press

$$+\left[-\frac{1}{\bar{U}_c'}j(\mathcal{D}_0+\mathrm{i}\alpha\bar{U}_{1,c}\bar{x})+\mathrm{i}\alpha j_1\bar{x}\right]A^\dagger\hat{y}\ln|\hat{y}|+O(\hat{y}), \tag{3.48}$$

$$\begin{aligned}\hat{T}_1^{\langle1\rangle}\ \rightarrow\ &\frac{\mathrm{i}\bar{T}_c'}{\alpha\bar{U}_c'^2\hat{y}^2}(\mathcal{D}_0+\mathrm{i}\alpha\bar{U}_{1,c}\bar{x})A^\dagger-\frac{1}{\mathrm{i}\alpha\bar{U}_c'^2\hat{y}}[\bar{T}_c''\mathcal{D}_0+\mathrm{i}\alpha(\bar{U}_{1,c}\bar{T}_c''-\bar{U}_c'\bar{T}_{1,c}')\bar{x}]A^\dagger\\&+\frac{\bar{T}_c'}{\bar{U}_c'^2\bar{T}_c\hat{y}}\left[\alpha^2\bar{T}_c^2d_1^{\langle1\rangle}-\frac{\mathrm{i}\bar{T}_c'}{\alpha}\mathcal{D}_0A^\dagger+(\bar{U}_c'\bar{T}_{1,c}-\bar{T}_c'\bar{U}_{1,c}-2\bar{T}_c\bar{U}_{1,c}')\bar{x}A^\dagger\right]\\&+O(\ln|\hat{y}|),\end{aligned} \tag{3.49}$$

where e_2 and e_3 are coefficients, each having the same value above and below the critical layer. It follows from (3.47) that the difference $(d_2^{\langle1\rangle+}-d_2^{\langle1\rangle-})$ is related to the jump of the streamwise velocity $\hat{u}_1^{\langle1\rangle}$ across the critical layer,

$$-\frac{3\bar{T}_c}{\alpha^2\bar{U}_c'}(d_2^{\langle1\rangle+}-d_2^{\langle1\rangle-})=\hat{u}_1^{\langle1\rangle}(\hat{y}=0^+)-\hat{u}_1^{\langle1\rangle}(\hat{y}=0^-). \tag{3.50}$$

The right-hand side of the above equation is to be found by considering the inner solution in the critical layer. The issuing analysis in § 3.3 is rather complex, but the principal outcome consists of (a) the jump, which is used in (3.46) to give the amplitude equation (3.67), and (b) the evolution equations (3.61) and (3.66), which govern the temperature and vorticity of the CS in the critical layer. The reader who is primarily interested in the results may skip much of the algebra in § 3.3 and go to § 4, where the outcome is summarised.

3.3. *Inner expansions in the critical layer*

Due to the algebraic singularity of $\hat{T}$ (see (3.27) and (3.49)) and the logarithmic singularity of $\hat{u}$ (see (3.47)) in the outer expansions, we need to find the corresponding inner solution in the critical layer. As indicated by (3.27) and (3.49), the strength of the pole singularity in the temperature is controlled by $\bar{T}_c'$. When $\bar{T}_c'=O(1)$, the critical layer is weakly nonlinear (Goldstein & Leib 1989; Leib 1991), but is strongly nonlinear when $\bar{T}_c'=O(\epsilon^{1/2})$, which is the case if $Ma=O(\epsilon^{1/4})$ as was noted by Sparks & Wu (2008). It turns out that $\bar{T}_c'$ is rather small even for $Ma=O(1)$, implying that a strongly nonlinear critical layer is more appropriate. Following Sparks & Wu (2008), we treat $\bar{T}_c'$ as an independent parameter with $\bar{T}_c'=O(\epsilon^{1/2})$. Given that the critical layer is located at the generalised inflection point, where $\bar{T}_c'/\bar{T}_c=\bar{U}_c''/\bar{U}_c'$, we scale the parameters as

$$\bar{T}_c'=\bar{T}_{cM}'\epsilon^{1/2},\quad \bar{U}_c''=\bar{U}_{cM}''\epsilon^{1/2}, \tag{3.51a,b}$$

where $\bar{T}_{cM}'$, $\bar{U}_{cM}''=O(1)$ and

$$\bar{T}_{cM}'/\bar{T}_c=\bar{U}_{cM}''/\bar{U}_c'. \tag{3.52}$$

The solution in the critical layer is described by the inner variable Y defined by (3.12) and can be expanded as (Sparks & Wu 2008; Wu & Zhuang 2016)

$$\tilde{q}=\epsilon\tilde{q}_0(\tau,\bar{x},Y,\zeta)+\epsilon^{3/2}\ln\epsilon\tilde{q}_{1L}(\tau,\bar{x},Y,\zeta)+\epsilon^{3/2}\tilde{q}_1(\tau,\bar{x},Y,\zeta)+\cdots, \tag{3.53}$$

https://doi.org/10.1017/jfm.2019.909 Published online by Cambridge University Press

where $\tilde{q}$ stands for the quantities u, v, T, p, $\tilde{\rho}$ and $\tilde{\mu}$. Here, the molecular viscosity fluctuation $\tilde{\mu}$ arises due to its dependence on $\tilde{T}$, and the leading-order term in the critical layer can be expressed as

$$\tilde{\mu}_0 = \frac{\mathrm{d}\mu}{\mathrm{d}T}\tilde{T}_0 \overset{\text{def.}}{=\!=} \mu_c'\tilde{T}_0. \tag{3.54}$$

Substituting expansions (3.53) and (3.13) together with the scaling (3.51) into (2.23)–(2.27), we obtain the equations at leading order. The inner solutions for $\tilde{v}_0$ and $\tilde{p}_0$, which match with the corresponding outer expansions, are found as,

$$\tilde{v}_0 = -\mathrm{i}\alpha A^\dagger \mathrm{e}^{\mathrm{i}\alpha\zeta} + \text{c.c.}, \quad \tilde{p}_0 = \frac{\bar{U}_c'}{\bar{T}_c}A^\dagger \mathrm{e}^{\mathrm{i}\alpha\zeta} + \text{c.c.}, \tag{3.55a,b}$$

which are simply trivial continuations of the outer solutions. The expansion of the continuity and momentum equations to the second order shows that the solution for $\tilde{u}_0$ matching with the outer solution (3.25) is

$$\tilde{u}_0 = -b_1 A^\dagger \mathrm{e}^{\mathrm{i}\alpha\zeta} + \text{c.c.}, \tag{3.56}$$

and that the solution for $\tilde{v}_1$ that matches with (3.26) and (3.48) is

$$\tilde{v}_1 = \left[\mathrm{i}\alpha b_1 Y + \frac{b_1}{\bar{U}_c'}(\mathcal{D}_0 + \mathrm{i}\alpha\bar{U}_{1,c}\bar{x}) - \frac{\partial}{c\partial\bar{x}} + \frac{\mathrm{i}\alpha\bar{U}_{1,c}'}{\bar{U}_c'}\bar{x}\right]A^\dagger \mathrm{e}^{\mathrm{i}\alpha\zeta} + \text{c.c.} \tag{3.57}$$

The leading-order temperature satisfies the equation,

$$\begin{aligned}&\mathcal{L}_N^\dagger\tilde{T}_0 - \frac{\bar{\lambda}\bar{T}_c\mu_c}{Pr}\frac{\partial^2}{\partial Y^2}\tilde{T}_0 - \frac{\tilde{\lambda}\bar{T}_c\tilde{\mu}_{t,c}}{\tilde{P}r_T}\frac{\partial^2}{\partial Y^2}\tilde{T}_0(t-\hat{\tau}_1)\\ &\quad = (\gamma-1)Ma^2\bar{T}_c\left[\mathcal{D}_0\tilde{p}_0 + (\bar{U}_c'Y + \bar{U}_{1,c}\bar{x})\frac{\partial\tilde{p}_0}{\partial\zeta}\right] - (\bar{T}_c''Y + \bar{T}_{1,c}'\bar{x} + \bar{T}_{cM}')\tilde{v}_0,\end{aligned} \tag{3.58}$$

where $\mathcal{L}_N^\dagger$ denotes the nonlinear operator

$$\mathcal{L}_N^\dagger \equiv \frac{\partial}{\partial\tau} + \frac{\partial}{\partial\bar{x}} + (\bar{U}_c'Y + \bar{U}_{1,c}\bar{x})\frac{\partial}{\partial\zeta} - (\mathrm{i}\alpha A^\dagger\mathrm{e}^{\mathrm{i}\alpha\zeta} + \text{c.c.} - \sigma\bar{\lambda}^{2/3}\bar{V}_c)\frac{\partial}{\partial Y}, \tag{3.59}$$

in which $\bar{V}_c$ is the re-scaled mean-flow vertical velocity at the critical level.

In order to aid the matching with the outer solution, we make the substitution

$$T^\dagger = \tilde{T}_0 - \left[\frac{\bar{T}_c''}{\bar{U}_c'} + (\gamma-1)Ma^2\bar{U}_c'\right](A^\dagger\mathrm{e}^{\mathrm{i}\alpha\zeta} + \text{c.c.}). \tag{3.60}$$

Substitution of (3.55) and (3.60) into (3.58) reduces the latter to

$$\begin{aligned}&\mathcal{L}_N^\dagger T^\dagger - \frac{\bar{\lambda}\bar{T}_c\mu_c}{Pr}\frac{\partial^2}{\partial Y^2}T^\dagger - \frac{\tilde{\lambda}\bar{T}_c\tilde{\mu}_{t,c}}{\tilde{P}r_T}\frac{\partial^2}{\partial Y^2}T^\dagger(t-\hat{\tau}_1)\\ &\quad = \left(\mathrm{i}\alpha\bar{T}_{cM}' - \frac{\bar{T}_c''}{\bar{U}_c'}\mathcal{D}_0 + \mathrm{i}\alpha\frac{\bar{U}_c'\bar{T}_{1,c}' - \bar{U}_{1,c}\bar{T}_c''}{\bar{U}_c'}\bar{x}\right)A^\dagger\mathrm{e}^{\mathrm{i}\alpha\zeta} + \text{c.c.}\end{aligned} \tag{3.61}$$

As $Y\to\pm\infty$, $\tilde{T}_0$ matches with the $O(\epsilon)$ terms in the outer expansion (3.27) and (3.49) when the latter is written in terms of $Y = \hat{y}/\epsilon^{1/2}$ and $\bar{T}_c'$ is relegated to a higher order.

Substitution of the expansions (3.53) and (3.13) into the equations (2.23)–(2.25) gives, at the next (third) order, the equations

https://doi.org/10.1017/jfm.2019.909 Published online by Cambridge University Press

$$\mathcal{L}_N^{\dagger}\tilde{T}_0+(\bar{T}_c''Y+\bar{T}_{1,c}'\bar{x}+\bar{T}_{cM}')\tilde{v}_0-\gamma Ma^2\bar{T}_c\left[\mathcal{D}_0\tilde{p}_0+(\bar{U}_c'Y+\bar{U}_{1,c}\bar{x})\frac{\partial\tilde{p}_0}{\partial\zeta}\right]$$
$$=\bar{T}_c\left(\frac{\partial\tilde{u}_1}{\partial\zeta}+\frac{\partial\tilde{v}_2}{\partial Y}+\frac{\partial\tilde{u}_0}{c\partial\bar{x}}\right)+\bar{T}_{1,c}\bar{x}\left(\frac{\partial\tilde{u}_0}{\partial\zeta}+\frac{\partial\tilde{v}_1}{\partial Y}\right), \tag{3.62}$$

$$\mathcal{L}_N^{\dagger}\tilde{u}_1-\bar{\lambda}\bar{T}_c\mu_c\frac{\partial^2}{\partial Y^2}\tilde{u}_1-\tilde{\lambda}\bar{T}_c\tilde{\mu}_{t,c}\frac{\partial^2}{\partial Y^2}\tilde{u}_1(t-\hat{\tau}_2)$$
$$=\bar{\lambda}\bar{T}_c\bar{U}_c'\mu_c'\frac{\partial\tilde{T}_0}{\partial Y}-\left(\frac{1}{2}\bar{T}_c''Y^2+\bar{T}_{1,c}'\bar{x}Y+\bar{T}_{cM}'Y\right)\frac{\partial\tilde{p}_0}{\partial\zeta}-\tilde{T}_0\frac{\partial\tilde{p}_0}{\partial\zeta}-\bar{T}_{1,c}\bar{x}\left(\frac{\partial\tilde{p}_1}{\partial\zeta}+\frac{\partial\tilde{p}_0}{c\partial\bar{x}}\right)$$
$$-\bar{T}_c\left(\frac{\partial\tilde{p}_2}{\partial\zeta}+\frac{\partial\tilde{p}_1}{c\partial\bar{x}}\right)-\tilde{u}_0\frac{\partial\tilde{u}_0}{\partial\zeta}-\left(\bar{U}_{1,c}'\bar{x}Y+\frac{1}{2}\bar{U}_{2,c}\bar{x}^2\right)\frac{\partial\tilde{u}_0}{\partial\zeta}-(\bar{U}_c'Y+\bar{U}_{1,c}\bar{x})\frac{\partial\tilde{u}_0}{c\partial\bar{x}}$$
$$-\bar{U}_{1,c}\tilde{u}_0-\bar{U}_c'\tilde{v}_2-\bar{U}_{1,c}'\bar{x}\tilde{v}_1-\left(\frac{1}{2}\bar{U}_c'''Y^2+\bar{U}_{1,c}''\bar{x}Y+\frac{1}{2}\bar{U}_2'\bar{x}^2+\bar{U}_{cM}''Y\right)\tilde{v}_0$$
$$-(\gamma Ma^2\tilde{p}_0-\tilde{T}_0/\bar{T}_c)(\bar{U}_{1,c}+\sigma\bar{\lambda}^{2/3}\bar{U}_c'\bar{V}_c), \tag{3.63}$$

$$\frac{\partial\tilde{v}_0}{\partial\tau}+\frac{\partial\tilde{v}_0}{\partial\bar{x}}+(\bar{U}_c'Y+\bar{U}_{1,c}\bar{x})\frac{\partial\tilde{v}_0}{\partial\zeta}=-\bar{T}_c\frac{\partial\tilde{p}_2}{\partial Y}. \tag{3.64}$$

The first term on the right-hand side of (3.63) is associated with $\tilde{\mu}_0$, given by (3.54).

Differentiating (3.63) with respect to Y, and making use of the results (3.56), (3.57) and (3.64) as well as (3.62) and (3.58), followed by the introduction of the new dependent variable,

$$Q^{\dagger}=\tilde{u}_{1Y}-\left[\left(\alpha^2+\frac{\bar{U}_c'''}{\bar{U}_c'}-\frac{\bar{T}_c''}{\bar{T}_c}+\frac{Ma^2\bar{U}_c'^2}{\bar{T}_c}\right)A^{\dagger}\mathrm{e}^{\mathrm{i}\alpha\zeta}+\mathrm{c.c.}\right], \tag{3.65}$$

we obtain the equation for $Q^{\dagger}$,

$$\mathcal{L}_N^{\dagger}Q^{\dagger}-\bar{\lambda}\bar{T}_c\mu_c\frac{\partial^2}{\partial Y^2}Q^{\dagger}-\tilde{\lambda}\bar{T}_c\tilde{\mu}_{t,c}\frac{\partial^2}{\partial Y^2}Q^{\dagger}(t-\hat{\tau}_2)$$
$$=-\bar{\lambda}\bar{U}_c'\left(\frac{\mu_c}{Pr}-\bar{T}_c\mu_c'\right)\frac{\partial^2T^{\dagger}}{\partial Y^2}-\frac{\tilde{\lambda}\bar{U}_c'\tilde{\mu}_{t,c}}{\tilde{Pr}_T}\frac{\partial^2T^{\dagger}(t-\hat{\tau}_1)}{\partial Y^2}$$
$$-\frac{\bar{U}_c'}{\bar{T}_c}\left(\mathrm{i}\alpha A^{\dagger}\mathrm{e}^{\mathrm{i}\alpha\zeta}+\mathrm{c.c.}-\frac{\bar{U}_{1,c}}{\bar{U}_c'}-\sigma\bar{\lambda}^{2/3}\bar{V}_c\right)\frac{\partial T^{\dagger}}{\partial Y}-\left(\frac{\bar{U}_c'''}{\bar{U}_c'}-\frac{\bar{T}_c''}{\bar{T}_c}\right)\mathcal{D}_0(A^{\dagger}\mathrm{e}^{\mathrm{i}\alpha\zeta}+\mathrm{c.c.})$$
$$+\left[\bar{U}_c'\left(\frac{\bar{U}_{1,c}''}{\bar{U}_c'}-\frac{\bar{T}_{1,c}'}{\bar{T}_c}\right)-\left(\frac{\bar{U}_c'''}{\bar{U}_c'}-\frac{\bar{T}_c''}{\bar{T}_c}\right)\bar{U}_{1,c}\right]\bar{x}(\mathrm{i}\alpha A^{\dagger}\mathrm{e}^{\mathrm{i}\alpha\zeta}+\mathrm{c.c.}). \tag{3.66}$$

As $Y\to\pm\infty$, $Q^{\dagger}$ matches with $(\hat{u}_1^{\langle1\rangle}\mathrm{e}^{\mathrm{i}\alpha\zeta}+\mathrm{c.c.})$ in (3.47) differentiated with respect to $\hat{y}$ with $\bar{T}_c'$ and $\bar{U}_c''$ being relegated to higher orders.

Equation (3.66) allows us to determine the jump $(d_2^{\langle1\rangle+}-d_2^{\langle1\rangle-})$ as follows. Selecting the $n=1$ component of $Q^{\dagger}$ and integrating it with respect to Y gives $\tilde{u}_1^{\langle1\rangle}(\infty)-\tilde{u}_1^{\langle1\rangle}(-\infty)$. Matching between the outer solution $\epsilon^{3/2}\hat{u}_1^{\langle1\rangle}$ and the inner solution $\epsilon^{3/2}\tilde{u}_1$ means that $\hat{u}_1(y=y_c^+)-\hat{u}_1(y=y_c^-)=\tilde{u}_1^{\langle1\rangle}(\infty)-\tilde{u}_1^{\langle1\rangle}(-\infty)$. Combining this with (3.46) and (3.50), we obtain the amplitude equation for $A^{\dagger}$,

$$\frac{\alpha}{2\pi}\int_{-\infty}^{\infty}\int_0^{2\pi/\alpha}Q^{\dagger}\mathrm{e}^{-\mathrm{i}\alpha\zeta}\,\mathrm{d}\zeta\,\mathrm{d}Y=\frac{\bar{T}_c}{\alpha^2}\left[\frac{2\mathrm{i}}{\alpha}J_2\frac{\partial A^{\dagger}}{\partial\tau}-\frac{2\mathrm{i}}{\alpha}\left(\frac{J_1}{c}-J_2\right)\frac{\partial A^{\dagger}}{\partial\bar{x}}-J_0\bar{x}A^{\dagger}\right]. \tag{3.67}$$

https://doi.org/10.1017/jfm.2019.909 Published online by Cambridge University Press

The evolution system governing the nonlinear dynamics of CS consists of the amplitude equation (3.67), the temperature equation and vorticity equations, (3.61) and (3.66), subject to appropriate upstream and boundary conditions, which will be derived in § 4.2 and § 4.3 respectively. Several features of this system are worth noting. In the incompressible limit, $Ma = 0$, $\bar{T}_c' = \bar{T}_c'' = 0$ and the temperature fluctuation is absent, i.e. $T^\dagger \equiv 0$, and hence the system reduces to (3.37) and (3.44) in Wu & Zhuang (2016) as expected. For the laminar case with a parallel-flow assumption, we have $\tilde{\lambda} = 0$, $\bar{V} \equiv 0$ and $\bar{U}_1 = \bar{U}_1' = \bar{U}_1'' = \bar{T}_1 = \bar{T}_1' = 0$, and the system with $Pr = 1$ reduces to (4.12)–(4.14) in Sparks & Wu (2008), which further reduce to the incompressible limit (Goldstein & Hultgren 1988). On the other hand, in the limit $\bar{T}_{cM}' \gg 1$, the system can be simplified to a sole amplitude equation for $A^\dagger$ as derived in Sparks & Wu (2008).

4. Evolution system of coherent structures

4.1. *Coupled equations*

A main remaining task of this paper is to solve the evolution system ((3.67) coupled with (3.61) and (3.66)) subject to appropriate initial and boundary conditions. In order to reduce the number of parameters, it is convenient to introduce the renormalised variables,

$$\widetilde{A} = \alpha^2 \bar{U}_c' A^\dagger, \quad \widetilde{T} = T^\dagger, \quad \widetilde{Q} = \alpha^2 \bar{U}_c' \left(\frac{\bar{U}_c'''}{\bar{U}_c'} - \frac{\bar{T}_c''}{\bar{T}_c} \right)^{-1} Q^\dagger \overset{\text{def.}}{=\!=} \frac{Q^\dagger}{p_Q}, \tag{4.1a–c}$$

as well as the renormalised streamwise and local transverse coordinates,

$$\bar{\xi} = \alpha \xi, \quad \bar{\eta} = \alpha (\bar{U}_c' Y + \bar{U}_{1,c} \bar{x}). \tag{4.2a,b}$$

The coupled equations (3.61), (3.66) and (3.67) then become,

$$\begin{cases} \dfrac{1}{2\pi} \displaystyle\int_{-\infty}^{\infty} \int_0^{2\pi} \widetilde{Q} \mathrm{e}^{-\mathrm{i}\bar{\zeta}} \, \mathrm{d}\bar{\zeta} \, \mathrm{d}\bar{\eta} = \Lambda_1 \frac{\partial \widetilde{A}}{\partial \tau} + \Lambda_2 \frac{\partial \widetilde{A}}{\partial \bar{x}} + \Lambda_0 \bar{x} \widetilde{A}, & (4.3a) \\ \mathcal{L}_N \widetilde{T} - \bar{\lambda}_1 \dfrac{\partial^2}{\partial \bar{\eta}^2} \widetilde{T} - \tilde{\lambda}_1 \dfrac{\partial^2}{\partial \bar{\eta}^2} \widetilde{T}(t - \hat{\tau}_1) \\ \quad = - \left[\left(p_1 \dfrac{\partial}{\partial \tau} + p_1 \dfrac{\partial}{\partial \bar{x}} - \mathrm{i} p_2 - \mathrm{i} \chi_1 \bar{x} \right) \widetilde{A} \mathrm{e}^{\mathrm{i}\bar{\zeta}} + \mathrm{c.c.} \right], & (4.3b) \\ \mathcal{L}_N \widetilde{Q} - \bar{\lambda}_2 \dfrac{\partial^2}{\partial \bar{\eta}^2} \widetilde{Q} - \tilde{\lambda}_2 \dfrac{\partial^2}{\partial \bar{\eta}^2} \widetilde{Q}(t - \hat{\tau}_2) \\ \quad = -\bar{\lambda}_3 \dfrac{\partial^2 \widetilde{T}}{\partial \bar{\eta}^2} - \tilde{\lambda}_3 \dfrac{\partial^2 \widetilde{T}(t - \hat{\tau}_1)}{\partial \bar{\eta}^2} + p_3 (\mathrm{i} \widetilde{A} \mathrm{e}^{\mathrm{i}\bar{\zeta}} + \mathrm{c.c.} - \chi) \dfrac{\partial \widetilde{T}}{\partial \bar{\eta}} \\ \qquad - \left[\left(\dfrac{\partial}{\partial \tau} + \dfrac{\partial}{\partial \bar{x}} - \mathrm{i} \chi_2 \bar{x} \right) \widetilde{A} \mathrm{e}^{\mathrm{i}\bar{\zeta}} + \mathrm{c.c.} \right], & (4.3c) \end{cases}$$

where we have put

$$\mathcal{L}_N \equiv \frac{\partial}{\partial \tau} + \frac{\partial}{\partial \bar{x}} + \bar{\eta} \frac{\partial}{\partial \bar{\zeta}} - (\mathrm{i} \widetilde{A} \mathrm{e}^{\mathrm{i}\bar{\zeta}} + \mathrm{c.c.} - \chi) \frac{\partial}{\partial \bar{\eta}}, \tag{4.4}$$

https://doi.org/10.1017/jfm.2019.909 Published online by Cambridge University Press

and the parameters in the system are,

$$\left.\begin{gathered}
\chi=\alpha(\bar{U}_{1,c}+\sigma\bar{\lambda}^{2/3}\bar{U}_c'\bar{V}_c),\quad \chi_1=(\bar{U}_c'\bar{T}_{1,c}'-\bar{U}_{1,c}\bar{T}_c'')/(\alpha\bar{U}_c'^2),\\
\chi_2=[\bar{U}_c'(\bar{U}_{1,c}''/\bar{U}_c'-\bar{T}_{1,c}'/\bar{T}_c)-(\bar{U}_c'''/\bar{U}_c'-\bar{T}_c''/\bar{T}_c)\bar{U}_{1,c}]/(\alpha\bar{U}_c'p_Q);\\
p_1=\bar{T}_c''/(\alpha\bar{U}_c'^2),\quad p_2=\bar{T}_{cM}'/(\alpha\bar{U}_c'),\quad p_3=\bar{U}_c'/(\bar{T}_cp_Q);\\
\Lambda_1=2\mathrm{i}\bar{T}_cJ_2/(\alpha^4p_Q),\quad \Lambda_2=-2\mathrm{i}\bar{T}_c(J_1/c-J_2)/(\alpha^4p_Q),\quad \Lambda_0=-\bar{T}_cJ_0/(\alpha^3p_Q);\\
\bar{\lambda}_1=\bar{\lambda}\bar{T}_c\mu_c(\alpha\bar{U}_c')^2/Pr,\quad \bar{\lambda}_2=\bar{\lambda}\bar{T}_c\mu_c(\alpha\bar{U}_c')^2,\quad \bar{\lambda}_3=\bar{\lambda}(\mu_c/Pr-\mu_c'\bar{T}_c)\alpha^2\bar{U}_c'^3/p_Q;\\
\tilde{\lambda}_1=\tilde{\lambda}\bar{T}_c\tilde{\mu}_{t,c}(\alpha\bar{U}_c')^2/\tilde{P}r_T,\quad \tilde{\lambda}_2=\tilde{\lambda}\bar{T}_c\tilde{\mu}_{t,c}(\alpha\bar{U}_c')^2,\quad \tilde{\lambda}_3=\tilde{\lambda}\tilde{\mu}_{t,c}\alpha^2\bar{U}_c'^3/(p_Q\tilde{P}r_T).
\end{gathered}\right\}\tag{4.5}$$

Since the unknown amplitude function $\widetilde{A}$ appears in the coefficients in both the temperature and vorticity equations, the evolution system (4.3) for CS is strongly nonlinear.

A turbulent flow differs from its laminar counterpart owing to the influences of small-scale fluctuations and the strong non-parallelism. The former is characterised by the eddy conductivity and viscosity, $\tilde{\lambda}_1$ and $\tilde{\lambda}_2$, as well as the time delays, $\hat{\tau}_1$ and $\hat{\tau}_2$. The non-parallelism is characterised by parameters χ, χ_1, χ_2 and Λ_0, of which χ indicates a translating critical-layer effect associated with motion of the critical level, similar to that in certain time-dependent flows (cf. Cowley 1985; Haynes & Cowley 1986).

4.2. *Upstream conditions*

The upstream condition can be derived by observing that as $\bar{x}\to-\infty$, the disturbance is of small amplitude so that the nonlinear terms in both the temperature and vorticity equations can be neglected. The system linearises, and only the fundamental component is present in the flow field. Solving the linear equations gives the upstream conditions for $\widetilde{T}(\tau,\bar{x},\bar{\eta},\bar{\zeta})$ and $\widetilde{Q}(\tau,\bar{x},\bar{\eta},\bar{\zeta})$ as

$$\widetilde{T}\to\left[-\int_0^\infty\mathscr{T}_A(\xi;\tau,\bar{x})\mathrm{e}^{-\lambda_{11}\xi^3/3+\mathrm{i}\chi\xi^2/2-\mathrm{i}\bar{\eta}\xi}\,\mathrm{d}\xi\right]\mathrm{e}^{\mathrm{i}\bar{\zeta}}+\mathrm{c.c.},\tag{4.6}$$

$$\widetilde{Q}\to\left[-\int_0^\infty\mathscr{Q}_A(\xi;\tau,\bar{x})\mathrm{e}^{-\lambda_{21}\xi^3/3+\mathrm{i}\chi\xi^2/2-\mathrm{i}\bar{\eta}\xi}\,\mathrm{d}\xi\right]\mathrm{e}^{\mathrm{i}\bar{\zeta}}+\mathrm{c.c.},\tag{4.7}$$

with

$$\left.\begin{aligned}
\mathscr{T}_A(\xi;\tau,\bar{x})&=\left[p_1\left(\frac{\partial}{\partial\tau}+\frac{\partial}{\partial\bar{x}}\right)-\mathrm{i}p_2-\mathrm{i}\chi_1(\bar{x}-\xi)\right]\widetilde{A}(\tau-\xi,\bar{x}-\xi),\\
\mathscr{Q}_A(\xi;\tau,\bar{x})&=\int_0^\xi(\lambda_{31}\xi^{\dagger2}+\mathrm{i}p_3\chi\xi^\dagger)\mathscr{T}_A(\xi^\dagger;\tau,\bar{x})\mathrm{e}^{-(\lambda_{11}-\lambda_{21})\xi^{\dagger3}/3}\,\mathrm{d}\xi^\dagger\\
&\quad+\left[\frac{\partial}{\partial\tau}+\frac{\partial}{\partial\bar{x}}-\mathrm{i}\chi_2(\bar{x}-\xi)\right]\widetilde{A}(\tau-\xi,\bar{x}-\xi),
\end{aligned}\right\}\tag{4.8}$$

and λ_{i1} $(i=1,2,3)$ being the normalised complex eddy conductivities and viscosities, which will be defined in (4.17).

Integrating (4.7) with respect to $\bar{\eta}$, we have

$$\int_{-\infty}^\infty\widetilde{Q}\,\mathrm{d}\bar{\eta}=-\pi(\mathcal{D}_0-\mathrm{i}\chi_2\bar{x})\widetilde{A}\mathrm{e}^{\mathrm{i}\bar{\zeta}}+\mathrm{c.c.}\tag{4.9}$$

https://doi.org/10.1017/jfm.2019.909 Published online by Cambridge University Press

This result is inserted into (4.3*a*) to give

$$\frac{\partial \widetilde{A}}{\partial \bar{x}} + \frac{1}{c_g}\frac{\partial \widetilde{A}}{\partial \tau} = \sigma_s \bar{x}\widetilde{A}, \tag{4.10}$$

where c_g is the group velocity,

$$c_g = (\Lambda_2 + \pi)/(\Lambda_1 + \pi), \tag{4.11}$$

and

$$\sigma_s = (\mathrm{i}\pi\chi_2 - \Lambda_0)/(\pi + \Lambda_2) \tag{4.12}$$

is a quantity characterising non-parallelism. It can be deduced from (4.10) that

$$\widetilde{A} \to \mathrm{e}^{\sigma_s \bar{x}^2/2 + \kappa_l \bar{x} - \mathrm{i}S_0\tau} \quad \text{as } \bar{x} \to -\infty, \tag{4.13}$$

where $\kappa_l = \mathrm{i}S_0/c_g$ with S_0 measuring the deviation of the disturbance frequency from that of the neutral mode ($\omega = \alpha c + \epsilon^{1/2}S_0$), and the real part of κ_l represents the scaled linear growth rate of $\widetilde{A}$. Since the group velocity c_g is a complex number, it is impossible to introduce the coordinate moving at the group velocity. This modulation equation is a first-order partial differential equation unlike the case of a real group velocity, where a modulation equation containing a second-order derivative with respect to the moving coordinate can be derived.

4.3. *Fourier decompositions and boundary conditions*

The solutions for $\widetilde{A}$, $\widetilde{T}$ and $\widetilde{Q}$ can be written as Fourier series (cf. Goldstein & Leib 1988; Wu & Tian 2012),

$$\widetilde{A} = A(\tau, \bar{x})\mathrm{e}^{-\mathrm{i}S_0\tau}, \tag{4.14}$$

$$[\widetilde{T}, \widetilde{Q}] = \sum_{n=-\infty}^{\infty} [T_n(\tau, \bar{x}, \eta), Q_n(\tau, \bar{x}, \eta)]\mathrm{e}^{\mathrm{i}n(\bar{\zeta} - S_0\tau)}, \tag{4.15}$$

where $\eta = \bar{\eta} - S_0$, $T_{-n} = T_n^*$ and $Q_{-n} = Q_n^*$ ($n \in \mathbb{N}^+$) with the superscript * denoting the complex conjugate. It is worth mentioning that T_0 and Q_0 represent the mean-flow distortion generated by the nonlinear self-interaction of CS. Inserting (4.14)–(4.15) into (4.3), we have

$$\int_{-\infty}^{\infty} Q_1 \,\mathrm{d}\eta = -\mathrm{i}S_0\Lambda_1 A + \Lambda_1\frac{\partial A}{\partial \tau} + \Lambda_2\frac{\partial A}{\partial \bar{x}} + \Lambda_0\bar{x}A, \tag{4.16a}$$

$$\left(\mathcal{D}_0 + \mathrm{i}n\eta + \chi\frac{\partial}{\partial \eta} - \lambda_{1n}\frac{\partial^2}{\partial \eta^2}\right) T_n + \mathrm{i}\frac{\partial}{\partial \eta}(A^*T_{n+1} - AT_{n-1})$$
$$= -\delta_{n1}(p_1\mathcal{D}_0 - \mathrm{i}p_1S_0 - \mathrm{i}p_2 - \mathrm{i}\chi_1\bar{x})A, \tag{4.16b}$$

$$\left(\mathcal{D}_0 + \mathrm{i}n\eta + \chi\frac{\partial}{\partial \eta} - \lambda_{2n}\frac{\partial^2}{\partial \eta^2}\right) Q_n + \mathrm{i}\frac{\partial}{\partial \eta}(A^*Q_{n+1} - AQ_{n-1})$$
$$= -\delta_{n1}(\mathcal{D}_0 - \mathrm{i}S_0 - \mathrm{i}\chi_2\bar{x})A + \mathrm{i}p_3\frac{\partial}{\partial \eta}(AT_{n-1} - A^*T_{n+1})$$
$$- p_3\chi\frac{\partial T_n}{\partial \eta} - \lambda_{3n}\frac{\partial^2 T_n}{\partial \eta^2}, \tag{4.16c}$$

where δ_{n1} denotes the Kronecker delta, and λ_{1n}, λ_{2n} and λ_{3n} are complex quantities to

https://doi.org/10.1017/jfm.2019.909 Published online by Cambridge University Press

characterise the molecular and coherent eddy conductivities and viscosities,

$$\lambda_{1n} = \bar{\lambda}_1 + \tilde{\lambda}_1 \mathrm{e}^{\mathrm{i}n\omega\hat{\tau}_1}, \quad \lambda_{2n} = \bar{\lambda}_2 + \tilde{\lambda}_2 \mathrm{e}^{\mathrm{i}n\omega\hat{\tau}_2}, \quad \lambda_{3n} = \bar{\lambda}_3 + \tilde{\lambda}_3 \mathrm{e}^{\mathrm{i}n\omega\hat{\tau}_1}. \tag{4.17a–c}$$

For the mathematical problem (4.16) to be well posed, the effective conductivity and diffusivity must be positive for $\hat{\tau}_i \neq 0$ $(i = 1, 2)$, and it is thus necessary to restrict $\tilde{\lambda}_i \leqslant \bar{\lambda}_i$ $(i = 1, 2)$.

The boundary conditions of T_n and Q_n follow from the dominant balances in (4.16*b*)–(4.16*c*) as $\eta \to \pm\infty$. After ignoring the $O(\eta^{-4})$ terms, they are written as,

$$T_1 \to \left(\frac{\mathrm{i}}{\eta} - \frac{\mathcal{D}_0}{\eta^2} - \frac{\mathrm{i}\mathcal{D}_0^2}{\eta^3} + \frac{\chi}{\eta^3}\right)(p_1\mathcal{D}_0 - \mathrm{i}p_1S_0 - \mathrm{i}p_2 - \mathrm{i}\chi_1\bar{x})A + O(\eta^{-4}), \tag{4.18a}$$

$$\begin{aligned} T_0 \to\ & -\frac{p_1|A|^2}{\eta^2} + \frac{2}{\eta^3}\left[\mathrm{i}p_1(A\mathcal{D}_0A^* - A^*\mathcal{D}_0A + \mathrm{i}S_0|A|^2)\right. \\ & \left. - (p_2 + \chi_1\bar{x})|A|^2 - (\chi_1 + p_1\chi)\mathcal{B}_1\right] + O(\eta^{-4}), \end{aligned} \tag{4.18b}$$

$$T_2 \to -\frac{\mathrm{i}}{2\eta^3}A(p_1\mathcal{D}_0 - \mathrm{i}p_1S_0 - \mathrm{i}p_2 - \mathrm{i}\chi_1\bar{x})A + O(\eta^{-4}), \tag{4.18c}$$

$$\begin{aligned} Q_1 \to\ & \left(\frac{\mathrm{i}}{\eta} - \frac{\mathcal{D}_0}{\eta^2} - \frac{\mathrm{i}\mathcal{D}_0^2}{\eta^3} + \frac{\chi}{\eta^3}\right)(\mathcal{D}_0 - \mathrm{i}S_0 - \mathrm{i}\chi_2\bar{x})A \\ & + p_3\chi\left(\frac{\mathrm{i}}{\eta^2} - \frac{2\mathcal{D}_0}{\eta^3}\right)(p_1\mathcal{D}_0 - \mathrm{i}p_1S_0 - \mathrm{i}p_2 - \mathrm{i}\chi_1\bar{x})A + O(\eta^{-4}), \end{aligned} \tag{4.19a}$$

$$\begin{aligned} Q_0 \to\ & -\frac{(p_1p_3+1)|A|^2}{\eta^2} + \frac{2}{\eta^3}\{\mathrm{i}(p_1p_3+1)(A\mathcal{D}_0A^* - A^*\mathcal{D}_0A) \\ & - [S_0 + p_3(p_1S_0 + p_2 + p_1\chi) + (\chi_2 + p_3\chi_1)\bar{x}]|A|^2 \\ & - [\chi_2 + p_3\chi_1 + \chi(p_1p_3+1)]\mathcal{B}_1\} + O(\eta^{-4}), \end{aligned} \tag{4.19b}$$

$$Q_2 \to -\frac{\mathrm{i}A}{2\eta^3}\{p_3(p_1\mathcal{D}_0 - \mathrm{i}p_1S_0 - \mathrm{i}p_2 - \mathrm{i}\chi_1\bar{x}) + \mathcal{D}_0 - \mathrm{i}S_0 - \mathrm{i}\chi_2\bar{x}\}A + O(\eta^{-4}), \tag{4.19c}$$

where we have put

$$\mathcal{B}_1(\tau, \bar{x}) = \int_0^\infty |A(\tau - \xi, \bar{x} - \xi)|^2 \,\mathrm{d}\xi. \tag{4.20}$$

In order to solve the evolution system, the infinite domain in the η-direction is truncated to a large but finite interval $-\tilde{H} \leqslant \eta \leqslant \tilde{H}$. Then equation (4.16*a*) becomes a second-order partial differential equation,

$$\begin{aligned} & \Lambda_1\frac{\partial A}{\partial\tau} + \Lambda_2\frac{\partial A}{\partial\bar{x}} + \left[\left(\Lambda_0 - \frac{2}{\tilde{H}}p_3\chi\chi_1\right)\bar{x} - \mathrm{i}S_0\Lambda_1 - \frac{2}{\tilde{H}}p_3\chi(S_0p_1 + p_2)\right]A \\ & = I_{10} - \frac{2}{\tilde{H}}\mathcal{D}_0[\mathcal{D}_0 - \mathrm{i}(S_0 + p_1p_3\chi) - \mathrm{i}\chi_2\bar{x}]A + O(\tilde{H}^{-3}), \end{aligned} \tag{4.21}$$

where we have defined

https://doi.org/10.1017/jfm.2019.909 Published online by Cambridge University Press

$$I_{nk} = \int_{-\tilde{H}}^{\tilde{H}} \eta^k Q_n \,\mathrm{d}\eta. \tag{4.22}$$

Equation (4.21) is similar to that in Wu & Zhuang (2016), and it can, according to (3.43) and (3.44) in that paper, be written into a first-order form with respect to $\bar{x}$,

$$\begin{aligned}&\tilde{\Lambda}_1\frac{\partial A}{\partial \tau} + \tilde{\Lambda}_2\frac{\partial A}{\partial \bar{x}} - \tilde{\Lambda}_{d,1}\frac{\partial^2 A}{\partial \tau^2} - \tilde{\Lambda}_{d,2}\frac{\partial^2 A}{\partial \tau \partial \bar{x}} + \tilde{\Lambda}_0 A \\ &\quad = \left(q_1 - q_2\bar{x} - \frac{2\Lambda_d}{\tilde{H}\Lambda_2}\frac{\partial}{\partial \tau}\right) I_{10} + \frac{2\mathrm{i}}{\tilde{H}} I_{11} - \frac{4}{\tilde{H}^2\Lambda_2}(I_{12} + \mathrm{i}\chi I_{10} - A^* I_{20}),\end{aligned} \tag{4.23}$$

the coefficients of which are given in appendix B.

4.4. *Strongly nonlinear sideband instability*

Now we show that a modulated wavepacket of the form (3.1) may represent a disturbance consisting of two or more instability waves with different frequencies, e.g. ω_0 and ω_1, which differ by $O(\epsilon^{1/2})$, i.e. $|\omega_0 - \omega_1| = O(\epsilon^{1/2})$; the two waves are in the 'sideband' of each other. The corresponding wavenumbers differ by $O(\epsilon^{1/2})$ also, i.e. $|\alpha_0 - \alpha_1| = O(\epsilon^{1/2})$. Supposing that the wave with ω_0 is stronger than the one with ω_1, we regard ω_0 as the 'central frequency', while ω_1 is its sideband frequency. The disturbance in the main layer is represented by $\epsilon\hat{q}_0(y)[A_0^\dagger \mathrm{e}^{\mathrm{i}(\alpha_0 x - \omega_0 t)} + A_1^\dagger \mathrm{e}^{\mathrm{i}(\alpha_1 x - \omega_1 t)}] + \text{c.c.}$, or

$$\epsilon\hat{q}_0(y)[A_0^\dagger + A_1^\dagger \mathrm{e}^{\mathrm{i}(\alpha_1 - \alpha_0)x - \mathrm{i}(\omega_1 - \omega_0)t}]\mathrm{e}^{\mathrm{i}\alpha_0\zeta} + \text{c.c.}, \tag{4.24}$$

which is of the form (3.1) since $|\alpha_0 - \alpha_1| \sim |\omega_0 - \omega_1| = O(\epsilon^{1/2})$. More generally, a modulated wavetrain may consist of discrete or a continuum of sideband modes. The focus of this section is on how this form of disturbance evolves, how the spectral components are excited and what role they would play in the nonlinear dynamics.

4.4.1. *Discrete-sideband disturbance*

For the case of a discrete sideband, the amplitude $\widetilde{A}$ is expressed as a Fourier series,

$$\widetilde{A} = A(\tau, \bar{x})\mathrm{e}^{-\mathrm{i}S_0\tau} = \sum_{m=-\infty}^{\infty} A^{(m)}(\bar{x})\mathrm{e}^{-\mathrm{i}m\Delta\tau}\mathrm{e}^{-\mathrm{i}S_0\tau}, \tag{4.25}$$

while a double Fourier decomposition is necessary for temperature $\widetilde{T}$ and vorticity $\widetilde{Q}$,

$$\begin{aligned}[\widetilde{T}, \widetilde{Q}] &= \sum_{n=-\infty}^{\infty} [T_n(\tau, \bar{x}, \eta), Q_n(\tau, \bar{x}, \eta)]\mathrm{e}^{\mathrm{i}n(\bar{\zeta} - S_0\tau)} \\ &= \sum_{n=-\infty}^{\infty}\sum_{m=-\infty}^{\infty} [T_n^{(m)}(\bar{x}, \eta), Q_n^{(m)}(\bar{x}, \eta)]\mathrm{e}^{-\mathrm{i}m\Delta\tau}\mathrm{e}^{\mathrm{i}n(\bar{\zeta} - S_0\tau)},\end{aligned} \tag{4.26}$$

with the reality condition demanding that $T_{-n} = T_n^*$, $T_{-n}^{(m)} = T_n^{(-m)*}$ and similarly for Q_n and $Q_n^{(m)}$. Substituting (4.25)–(4.26) into (4.23) and (4.16*b*)–(4.16*c*), we obtain the equations for $A^{(m)}$, $T_n^{(m)}$ and $Q_n^{(m)}$ as,

https://doi.org/10.1017/jfm.2019.909 Published online by Cambridge University Press

$$(\mathrm{i}m\Delta\tilde{\Lambda}_2+\tilde{\Lambda}_{d,2})\frac{\partial A^{(m)}}{\partial\bar{x}}+(\tilde{\Lambda}_0-\mathrm{i}m\Delta\tilde{\Lambda}_1+m^2\Delta^2\tilde{\Lambda}_{d,1})A^{(m)}$$
$$=\left(q_1-q_2\bar{x}+\frac{2\mathrm{i}m\Delta\Lambda_d}{\tilde{H}\Lambda_2}\right)I_{10}^{(m)}+\frac{2\mathrm{i}}{\tilde{H}}I_{11}^{(m)}$$
$$-\frac{4}{\tilde{H}^2\Lambda_2}\left[I_{12}^{(m)}+\mathrm{i}\chi I_{10}^{(m)}-\sum_{k=-\infty}^{\infty}A^{(k)*}I_{20}^{(m+k)}\right], \tag{4.27a}$$

$$\left(\frac{\partial}{\partial\bar{x}}+\mathrm{i}n\eta-\mathrm{i}m\Delta+\chi\frac{\partial}{\partial\eta}-\lambda_{1n}\frac{\partial^2}{\partial\eta^2}\right)T_n^{(m)}+\mathrm{i}\frac{\partial}{\partial\eta}\sum_{k=-\infty}^{\infty}[A^{(k)*}T_{n+1}^{(m+k)}-A^{(k)}T_{n-1}^{(m-k)}]$$
$$=-\delta_{n1}\left(p_1\frac{\partial}{\partial\bar{x}}-\mathrm{i}p_1m\Delta-\mathrm{i}p_1S_0-\mathrm{i}p_2-\mathrm{i}\chi_1\bar{x}\right)A^{(m)}, \tag{4.27b}$$

$$\left(\frac{\partial}{\partial\bar{x}}+\mathrm{i}n\eta-\mathrm{i}m\Delta+\chi\frac{\partial}{\partial\eta}-\lambda_{2n}\frac{\partial^2}{\partial\eta^2}\right)Q_n^{(m)}+\mathrm{i}\frac{\partial}{\partial\eta}\sum_{k=-\infty}^{\infty}[A^{(k)*}Q_{n+1}^{(m+k)}-A^{(k)}Q_{n-1}^{(m-k)}]$$
$$=-\mathrm{i}p_3\frac{\partial}{\partial\eta}\sum_{k=-\infty}^{\infty}[A^{(k)*}T_{n+1}^{(m+k)}-A^{(k)}T_{n-1}^{(m-k)}]-p_3\chi\frac{\partial T_n^{(m)}}{\partial\eta}$$
$$-\lambda_{3n}\frac{\partial^2T_n^{(m)}}{\partial\eta^2}-\delta_{n1}\left(\frac{\partial}{\partial\bar{x}}-\mathrm{i}m\Delta-\mathrm{i}S_0-\mathrm{i}\chi_2\bar{x}\right)A^{(m)}, \tag{4.27c}$$

where

$$I_{nk}^{(m)}(\bar{x})=\int_{-\tilde{H}}^{\tilde{H}}Q_n^{(m)}(\bar{x},\eta)\eta^k\,\mathrm{d}\eta. \tag{4.28}$$

We consider a particular form of disturbance that consists of three modes upstream. The upstream condition for the amplitude (4.14) is then given by

$$\widetilde{A}\to(a_0^-\mathrm{e}^{\mathrm{i}\varphi_0^-}\mathrm{e}^{\kappa_l^-\bar{x}+\mathrm{i}\Delta\tau}+\mathrm{e}^{\kappa_l\bar{x}}+a_0^+\mathrm{e}^{\mathrm{i}\varphi_0^+}\mathrm{e}^{\kappa_l^+\bar{x}-\mathrm{i}\Delta\tau})\mathrm{e}^{\sigma_s\bar{x}^2/2-\mathrm{i}S_0\tau}\quad\text{as }\bar{x}\to-\infty, \tag{4.29}$$

where $\epsilon^{1/2}\Delta=\omega_v$ is the scaled frequency difference, $a_0^{\pm}$, $\varphi_0^{\pm}$ and $\kappa_l^{\pm}$ represent the initial amplitudes, phases and the linear growth rates of the two sidebands respectively, whose frequencies are $\omega^{\pm}=\omega_0\pm\omega_v=\omega_0\pm\epsilon^{1/2}\Delta=\alpha_0c+\epsilon^{1/2}(S_0\pm\Delta)$. Inserting (4.29) into (4.10), we have $\kappa_l=\mathrm{i}S_0/c_g$ and $\kappa_l^{\pm}=\mathrm{i}(S_0\pm\Delta)/c_g$. Then the upstream conditions for $\widetilde{T}$ and $\widetilde{Q}$ can be found by inserting (4.29) into (4.6) and (4.7) respectively.

The boundary conditions for $T_n^{(m)}$ and $Q_n^{(m)}$ follow from (4.18*a*)–(4.19*c*) provided that the nonlinear terms involving A are replaced by the Cauchy products, i.e.

$$\left.\begin{gathered}|A|^2\Rightarrow\sum_{k=-\infty}^{\infty}[A^{(k)}A^{(k-m)*}],\quad A\mathcal{D}_0A\Rightarrow\sum_{k=-\infty}^{\infty}\left\{A^{(k)}\left[\frac{\partial}{\partial\bar{x}}-\mathrm{i}(m-k)\Delta\right]A^{(m-k)}\right\},\\ A^*\mathcal{D}_0A\Rightarrow\sum_{k=-\infty}^{\infty}\left\{A^{(k)*}\left[\frac{\partial}{\partial\bar{x}}-\mathrm{i}(m+k)\Delta\right]A^{(m+k)}\right\},\quad A\mathcal{D}_0A^*\Rightarrow(A^*\mathcal{D}_0A)^*,\\ \mathcal{B}_1\Rightarrow\mathcal{B}_1^{(m)}(\tau,\bar{x})=\sum_{k=-\infty}^{\infty}\int_0^{\infty}[A^{(k)}(\bar{x}-\xi)A^{(k-m)*}(\bar{x}-\xi)]\mathrm{e}^{\mathrm{i}m\Delta\xi}\,\mathrm{d}\xi.\end{gathered}\right\} \tag{4.30}$$

https://doi.org/10.1017/jfm.2019.909 Published online by Cambridge University Press

4.4.2. *Continuous-sideband disturbance*

In the case of a continuous sideband, we perform a Fourier transform of the coupled equations (4.3) with respect to τ. The transformed quantities of $\widetilde{A}$, $\widetilde{T}$ and $\widetilde{Q}$ in spectral space are expressed as,

$$\mathscr{F}_{\tau\to\omega}[\widetilde{A}(\tau,\bar{x})]=\widehat{A}(\omega-S_0,\bar{x}), \tag{4.31}$$

$$\mathscr{F}_{\tau\to\omega}[\widetilde{T}(\tau,\bar{x},\eta),\widetilde{Q}(\tau,\bar{x},\eta)]=\sum_{n=-\infty}^{\infty}[\widehat{T}_n(\omega-S_0,\bar{x},\eta),\widehat{Q}_n(\omega-S_0,\bar{x},\eta)]\mathrm{e}^{\mathrm{i}n\bar{\zeta}}. \tag{4.32}$$

The equations governing the spectral components are similar to (4.27) for the discrete case, provided that the terms $A^{(m)}$, $T_n^{(m)}$, $Q_n^{(m)}$ and $I_{nk}^{(m)}$ are replaced by their respective Fourier transforms $\widehat{A}(\omega,\bar{x})$, $\widehat{T}_n(\omega,\bar{x},\eta)$, $\widehat{Q}_n(\omega,\bar{x},\eta)$ and $\widehat{I}_{nk}(\omega,\bar{x})$ respectively with

$$\widehat{I}_{nk}(\omega,\bar{x})=\int_{-\tilde{H}}^{\tilde{H}}\widehat{Q}_n(\omega,\bar{x},\eta)\eta^k\,\mathrm{d}\eta. \tag{4.33}$$

Meanwhile the term $(-\mathrm{i}m\Delta)$, which is produced by the differential operator $\partial/\partial\tau$, is written as $(-\mathrm{i}\omega)$, and the terms with the Cauchy products in (4.27) and the boundary conditions (4.18*a*)–(4.19*c*) are substituted by the corresponding convolutions such as

$$\widehat{|A|^2}(\omega,\bar{x})=\widehat{A}(\omega,\bar{x})*\widehat{A}^*(\omega,\bar{x})=\int_{-\infty}^{\infty}\widehat{A}(\omega-s,\bar{x})\widehat{A}^*(s,\bar{x})\,\mathrm{d}s. \tag{4.34}$$

The upstream condition for $\widehat{A}$ is found by Fourier transforming (4.10) as

$$\widehat{A}(\omega,\bar{x})\to\widehat{A}_0(\omega)\exp(\sigma_s\bar{x}^2/2+\mathrm{i}\omega\bar{x}/c_g)\quad\text{as }\bar{x}\to-\infty, \tag{4.35}$$

where $\widehat{A}_0(\omega)$ is the initial spectrum. In in our calculations, a Gaussian distribution,

$$\widehat{A}_0(\omega)=(d\sqrt{\pi})^{-1}\exp(-\omega^2/d^2), \tag{4.36}$$

will be used (cf. Wu & Huerre 2009), where d is the scaled spectral bandwidth of the oncoming wavepacket, and $\widehat{A}$ is normalised by d such that the overall intensity of $\widehat{A}$ is (scaled to) 1. The upstream wavepacket envelope in physical space is given by

$$\widetilde{A}(\tau,\bar{x})\to(2\pi)^{-1}\exp[\sigma_s\bar{x}^2/2-(\bar{x}/c_g-\tau)^2d^2/4]\mathrm{e}^{-\mathrm{i}S_0\tau}\quad\text{as }\bar{x}\to-\infty. \tag{4.37}$$

A modulated wavepacket of this form can be measured more concisely by its mean square,

$$\overline{|\widetilde{A}|^2}\to[d\sqrt{(2\pi)^3}]^{-1}\exp(-\bar{x}^2/\sigma_e^2)\quad\text{as }\bar{x}\to-\infty, \tag{4.38}$$

which is Gaussian since

$$\sigma_e^{-2}=-(\sigma_s+\sigma_s^*)/2-(1/c_g-1/c_g^*)^2d^2/8\in\mathbb{R}^+. \tag{4.39}$$

Obviously, $\sigma_e>0$ is the scale of the wavepacket analogous to Δ^{-1} in the discrete-sideband case.

https://doi.org/10.1017/jfm.2019.909 Published online by Cambridge University Press

The upstream conditions ($\bar{x} \to -\infty$) for $\widehat{T}$ and $\widehat{Q}$ are derived by Fourier transforming (4.6) and (4.7),

$$\widehat{T} \to \left[-\int_0^\infty \widehat{\mathscr{T}_A}(\xi;\omega,\bar{x}) \mathrm{e}^{-\lambda_{11}\xi^3/3+\mathrm{i}\chi\xi^2/2-\mathrm{i}\bar{\eta}\xi}\,\mathrm{d}\xi \right] \mathrm{e}^{\mathrm{i}\bar{\zeta}} + \mathrm{c.c.}, \tag{4.40}$$

$$\widehat{Q} \to \left[-\int_0^\infty \widehat{\mathscr{Q}_A}(\xi;\omega,\bar{x}) \mathrm{e}^{-\lambda_{21}\xi^3/3+\mathrm{i}\chi\xi^2/2-\mathrm{i}\bar{\eta}\xi}\,\mathrm{d}\xi \right] \mathrm{e}^{\mathrm{i}\bar{\zeta}} + \mathrm{c.c.}, \tag{4.41}$$

with

$$\left.\begin{aligned} \widehat{\mathscr{T}_A}(\xi;\omega,\bar{x}) &= \left[p_1 \frac{\partial}{\partial \bar{x}} - \mathrm{i}p_1\omega - \mathrm{i}p_2 - \mathrm{i}\chi_1(\bar{x}-\xi) \right] \widehat{A}(\omega,\bar{x}-\xi)\mathrm{e}^{\mathrm{i}\omega\xi}, \\ \widehat{\mathscr{Q}_A}(\xi;\omega,\bar{x}) &= \int_0^\xi \left(\lambda_{31}\xi^{\dagger 2} + \mathrm{i}p_3\xi^\dagger \right) \widehat{\mathscr{T}_A}(\xi^\dagger;\omega,\bar{x}) \mathrm{e}^{-(\lambda_{11}-\lambda_{21})\xi^{\dagger 3}/3}\,\mathrm{d}\xi^\dagger \\ &\quad + \left[\frac{\partial}{\partial \bar{x}} - \mathrm{i}\omega - \mathrm{i}\chi_2(\bar{x}-\xi) \right] \widehat{A}(\omega,\bar{x}-\xi)\mathrm{e}^{\mathrm{i}\omega\xi}. \end{aligned}\right\} \tag{4.42}$$

The numerical calculations for sideband modes (either discrete or continuous case) consist of solving the coupled equations (4.27) or their modified forms, subject to the corresponding initial and boundary conditions as described above.

The results on the nonlinear dynamics of the CS are presented in §§ 6.1–6.4, which may be read independently of § 5.

5. Acoustic radiation and its physical source

In this section, we consider how CS can radiate sound waves. Wu & Huerre (2009) showed that a pair of subsonic oblique (helical) modes interact to generate a spatially and temporally modulated mean-flow distortion; the latter then emits low-frequency sound waves. There will be a similar radiation mechanism with the two-dimensional CS under consideration. We will analyse the mean-flow distortion caused by modulated CS to find the actual sound source as well as the mechanism of radiation.

5.1. *Mean-flow distortion in the main layer*

The mean-flow distortion caused by the nonlinear interactions is a part of the CS, corresponding to the modulated components without the fast-varying carrier-wave factor, i.e. the components with $n = 0$ in (3.15) and (4.26). In the main layer, the expansion up to the first two orders takes the form,

$$\epsilon^2[(u_M, \epsilon^{1/2}v_M, T_M, p_M, \rho_M) + \epsilon^{1/2}(u_{M_2}, \epsilon^{1/2}v_{M_2}, T_{M_2}, p_{M_2}, \rho_{M_2}) + \cdots]. \tag{5.1}$$

The leading-order terms are governed by equations,

$$\left\{\begin{aligned} &\frac{1}{c}\frac{\partial u_M}{\partial \bar{x}} + \frac{\partial v_M}{\partial y} + \bar{T}\mathcal{D}_1\rho_M - \frac{\bar{T}'}{\bar{T}}v_M = \bar{T}f_c, && (5.2a)\\ &\mathcal{D}_1 u_M + \bar{U}'v_M + \frac{\bar{T}}{c}\frac{\partial p_M}{\partial \bar{x}} = f_x, && (5.2b)\\ &\frac{\partial p_M}{\partial y} = f_y, && (5.2c)\\ &\mathcal{D}_1 T_M + \bar{T}'v_M - (\gamma-1)Ma^2\bar{T}\ \mathcal{D}_1 p_M = f_T, && (5.2d)\\ &\gamma Ma^2\bar{T}p_M = T_M + \bar{T}^2\rho_M + \bar{T}f_s, && (5.2e) \end{aligned}\right.$$

https://doi.org/10.1017/jfm.2019.909 Published online by Cambridge University Press

where f_c, f_x, f_y, f_T and f_s are the nonlinear forcing terms in the main layer,

$$\left.\begin{aligned} f_c &= -\hat{\rho}_0\hat{u}_0\frac{\partial|A^\dagger|^2}{c\partial\bar{x}} - \left[A^{\dagger *}\frac{\partial}{\partial y}(\hat{v}_1^{\langle 1\rangle}\hat{\rho}_0 - \hat{v}_0\hat{\rho}_1^{\langle 1\rangle}) + \text{c.c.}\right], \\ f_x &= -\left\{[\hat{u}_0\hat{u}_0 + (\hat{T}_0 - \gamma Ma^2\bar{T}\hat{p}_0)\hat{p}_0]\frac{\partial|A^\dagger|^2}{c\partial\bar{x}} + [A^{\dagger *}(\hat{v}_1^{\langle 1\rangle}\hat{u}_0' - \hat{v}_0\hat{u}_1^{\langle 1\rangle\prime}) + \text{c.c.}]\right\}, \\ f_y &= 2|A^\dagger|^2(\hat{v}_0^2/\bar{T})', \\ f_T &= (\gamma-1)Ma^2(\hat{T}_0 - \gamma Ma^2\bar{T}\hat{p}_0)\hat{p}_0\mathcal{D}_1|A^\dagger|^2 \\ &\quad - [\hat{T}_0 - (\gamma-1)Ma^2\bar{T}\hat{p}_0]\hat{u}_0\frac{\partial|A^\dagger|^2}{c\partial\bar{x}} + [A^{\dagger *}(\mathrm{i}\alpha\mathscr{Z}_{T,1} + \mathscr{Z}_{T,2}) + \text{c.c.}], \\ f_s &= 2\hat{\rho}_0\hat{T}_0|A^\dagger|^2, \end{aligned}\right\} \tag{5.3}$$

with the complex quantities, $\mathscr{Z}_{T,1}$ and $\mathscr{Z}_{T,2}$, being given by

$$\left.\begin{aligned} \mathscr{Z}_{T,1} &= (\gamma-1)Ma^2[(\bar{U}-c)(\hat{T}_0\hat{p}_1^{\langle 1\rangle} - \hat{T}_1^{\langle 1\rangle}\hat{p}_0) + \bar{T}(\hat{u}_0\hat{p}_1^{\langle 1\rangle} - \hat{u}_1^{\langle 1\rangle}\hat{p}_0)] \\ &\quad + \hat{T}_0\hat{u}_1^{\langle 1\rangle} - \hat{T}_1^{\langle 1\rangle}\hat{u}_0, \\ \mathscr{Z}_{T,2} &= \hat{v}_0\hat{T}_1^{\langle 1\rangle\prime} - \hat{v}_1^{\langle 1\rangle}\hat{T}_0' + (\gamma-1)Ma^2\bar{T}(\hat{v}_1^{\langle 1\rangle}\hat{p}_0' - \hat{v}_0\hat{p}_1^{\langle 1\rangle\prime}). \end{aligned}\right\} \tag{5.4}$$

It is noted that these volumetric forcing terms in the main layer all vanish as $y\to\pm\infty$. Integrating (5.2*c*), we find $p_M = 2|A^\dagger|^2\hat{v}_0^2/\bar{T} + p_{M,\infty}(\tau,\bar{x})$, where we take $p_{M,\infty}\equiv 0$ so that $p_M\to 0$ as $y\to\pm\infty$, because otherwise in the far field, $O(\epsilon^2)$ streamwise velocity and temperature would be present according to (5.2*b*) and (5.2*d*). That would in turn imply an $O(\epsilon^2)$ transverse velocity, which is too large to be matched with v_M at $O(\epsilon^{5/2})$ in the main layer.

Now eliminating ρ_M, u_M and T_M among (5.2), we obtain,

$$\left(\frac{\partial}{\partial\tau} + \frac{\bar{U}}{c}\frac{\partial}{\partial\bar{x}}\right)\frac{\partial v_M}{\partial y} - \frac{\bar{U}'}{c}\frac{\partial v_M}{\partial\bar{x}} = -\mathcal{S}(\tau,\bar{x},y), \tag{5.5}$$

where the forcing $\mathcal{S}$ on the right-hand side is given by

$$\mathcal{S} = -\frac{\bar{T}}{c^2}\frac{\partial^2 p_M}{\partial\bar{x}^2} + \frac{1}{c}\frac{\partial f_x}{\partial\bar{x}} - \mathcal{D}_1\left(\bar{T}f_c + \frac{f_T}{\bar{T}}\right) + \mathcal{D}_1^2(Ma^2 p_M - f_s). \tag{5.6}$$

Note that $\mathcal{S}\to 0$ as $y\to\pm\infty$, and that the $O(\epsilon^2)$ quantities of the mean-flow distortion, (p_M, u_M, ρ_M, T_M), are completely trapped within the shear layer. Furthermore, equation (5.5) reduces to the correct incompressible limit (4.9) in Wu & Zhuang (2016). Each of f_x, f_c, f_T and f_s can be expressed in terms of the eigenfunction $\hat{p}_0(y)$ and the mean-flow profiles, as detailed in § C.1. We can evaluate $\mathcal{S}(\tau,\bar{x},y)$, and after using the relation $\mathcal{D}_1(y)\equiv\mathcal{D}_0 + [\bar{U}(y)/c - 1]\partial/\partial\bar{x}$, the final result is

$$\begin{aligned} \mathcal{S}(\tau,\bar{x},y) \;=\; & [2\bar{T}'J_{y1}^{\pm}(y)/\alpha^2 + \tilde{\mathcal{S}}_1(y)]\frac{\partial^2 B_0^\dagger}{c^2\partial\bar{x}^2} + [-2Ma^2\bar{U}'J_{y2}^{\pm}(y)/\alpha^2 + \tilde{\mathcal{S}}_2(y)]\mathcal{D}_0^2 B_0^\dagger \\ & + [2Ma^2\bar{U}'J_{y1}^{\pm}(y)/\alpha^2 - 2\bar{T}'J_{y2}^{\pm}(y)/\alpha^2 + \tilde{\mathcal{S}}_3(y)]\mathcal{D}_0\frac{\partial B_0^\dagger}{c\partial\bar{x}}, \end{aligned} \tag{5.7}$$

where

$$B_0^\dagger(\tau,\bar{x}) = |A^\dagger(\tau,\bar{x})|^2, \quad \tilde{\mathcal{S}}_i(y) = S_{i1}^\dagger\hat{p}_0^2 + S_{i2}^\dagger\hat{p}_0'^2 + S_{i3}^\dagger\hat{p}_0'\hat{p}_0, \tag{5.8a,b}$$

https://doi.org/10.1017/jfm.2019.909 Published online by Cambridge University Press

$$J_{yj}^{\pm}(y)=\int_{\pm\infty}^{y}\frac{\bar{T}}{(\bar{U}-c)^2}(\mathcal{G}_{j1}\hat{p}_0'\hat{p}_0+\alpha^2\mathcal{G}_{j2}\hat{p}_0^2)\,\mathrm{d}y^{\star}\quad(j=0,\,1,\,2),\tag{5.9}$$

with '$\pm$' referring to $y>y_c$ and $y<y_c$ respectively.

For the purpose of determining the radiated sound wave, it is necessary to write the complementary solution to (5.5) in physical space,

$$v_{M,c}=\left(\frac{\partial}{\partial\tau}+\frac{\bar{U}}{c}\frac{\partial}{\partial\bar{x}}\right)a_M^{\pm}(\tau,\bar{x}),\tag{5.10}$$

where $a_M^{\pm}(\tau,\bar{x})$ are arbitrary functions and may take different values for $y>y_c$ and $y<y_c$. The general solution to (5.5) can be found in Fourier spectral space with respect to both τ and $\bar{x}$, marked by a wide hat over the quantity, as

$$\widehat{v_M}(\omega,\kappa,y)=\mathrm{i}(\bar{U}\kappa/c-\omega)\left[\widehat{a_M^{\pm}}(\omega,\kappa)+\int_{\pm\infty}^{y}\frac{\widehat{\mathcal{S}}(\omega,\kappa,y)}{(\bar{U}\kappa/c-\omega)^2}\,\mathrm{d}y\right].\tag{5.11}$$

Obviously, $\widehat{v_M}$ has non-zero values when $y\to\pm\infty$ as (5.11) shows, leading to a pressure perturbation in the far field. On the other hand, as $y\to y_c^{\pm}$,

$$\widehat{v_M}(y_c^{+})-\widehat{v_M}(y_c^{-})=\mathrm{i}(\kappa-\omega)\left[(\widehat{a_M^{+}}-\widehat{a_M^{-}})-\fint_{-\infty}^{\infty}\frac{\widehat{\mathcal{S}}}{(\bar{U}\kappa/c-\omega)^2}\,\mathrm{d}y\right].\tag{5.12}$$

The jump across the critical layer, $[\widehat{v_M}(y_c^{+})-\widehat{v_M}(y_c^{-})]$, will be determined in § 5.2. Our aim is to find $a_M^{\pm}(\tau,\bar{x})$ or $\widehat{a_M^{\pm}}(\tau,\bar{x})$ and analyse their role in the radiation of sound waves.

It is also necessary to find the $O(\epsilon^{5/2})$ pressure $p_{M_2}(y)$ in (5.1), whose governing equation is $\partial p_{M_2}/\partial y=f_{y_2}(\tau,\bar{x},y)$, with

$$\begin{aligned}f_{y_2}\;=\;&(2\gamma Ma^2\hat{p}_0'\hat{p}_0|A^{\dagger}|^2-p_M')\frac{\bar{T}_1\bar{x}}{\bar{T}}-\left\{\frac{A^{\dagger *}}{\bar{T}}\left[\mathrm{i}\alpha(\hat{u}_0\hat{v}_1^{\langle1\rangle}+\hat{u}_1^{\langle1\rangle}\hat{v}_0)-\hat{v}_0\hat{v}_1^{\langle1\rangle\prime}-\hat{v}_1^{\langle1\rangle}\hat{v}_0'\right.\right.\\&\left.\left.+\;(\hat{T}_0-\gamma Ma^2\bar{T}\hat{p}_0)\hat{p}_1^{\langle1\rangle\prime}+(\hat{T}_1^{\langle1\rangle}-\gamma Ma^2\bar{T}\hat{p}_1^{\langle1\rangle})\hat{p}_0'+\hat{u}_0\hat{v}_0\frac{\partial A^{\dagger}}{c\partial\bar{x}}\right]+\mathrm{c.c.}\right\}.\end{aligned}\tag{5.13}$$

Integrating it with respect to y, we have

$$p_{M_2}(y\to\infty)-p_{M_2}(y\to-\infty)=\fint_{-\infty}^{\infty}f_{y_2}\,\mathrm{d}y\overset{\text{def.}}{=\!=}\mathcal{Y}(\tau,\bar{x}).\tag{5.14}$$

After integration by parts, $\mathcal{Y}$ can be written as,

$$\mathcal{Y}(\tau,\bar{x})=\mathrm{i}(B_1^{\dagger}-B_1^{\dagger *})\tilde{\mathcal{Y}}_1+\mathrm{i}(B_2^{\dagger}-B_2^{\dagger *})\tilde{\mathcal{Y}}_2+\bar{x}B_0^{\dagger}\tilde{\mathcal{Y}}_0,\tag{5.15}$$

where

$$\tilde{\mathcal{Y}}_j=\fint_{-\infty}^{\infty}(G_{j1}^{\dagger}+G_{j2}^{\dagger}J_{yj}^{\pm}+G_{j3}^{\dagger}K_{yj}^{\pm})\,\mathrm{d}y\quad(j=0,\,1,\,2);\tag{5.16}$$

$$B_1^{\dagger}(\tau,\bar{x})\equiv c^{-1}A^{\dagger *}\frac{\partial A^{\dagger}}{\partial\bar{x}},\quad B_2^{\dagger}(\tau,\bar{x})\equiv A^{\dagger *}\mathcal{D}_0A^{\dagger};\tag{5.17a,b}$$

$$J_{yj}^{\pm}(y)=\int_{\pm\infty}^{y}(\mathcal{G}_{j1}\hat{p}_0'\hat{p}_0+\alpha^2\mathcal{G}_{j2}\hat{p}_0^2)\,\mathrm{d}y^{\star},\quad K_{yj}^{\pm}(y)=\begin{cases}K_j(y), & y<y_c,\\ K_j(y)-J_jp_{00}(y), & y>y_c,\end{cases}\tag{5.18a,b}$$

and the expressions for G_{ji} in (5.16) are given in § C.2.

https://doi.org/10.1017/jfm.2019.909 Published online by Cambridge University Press

5.2. *Asymptotic matching with the critical layer*

To verify the jump (5.12) of the $O(\epsilon^{5/2})$ normal velocity across the critical layer in the mean-flow distortion, we examine the $O(\epsilon^2)$ expansion of the continuity equation in the critical layer, which, after use is made of the temperature equation, reads

$$\left[\frac{\partial \tilde{u}_1}{c\partial\bar{x}}+\frac{\partial \tilde{v}_3}{\partial Y}\right]_0 = \left[\frac{\bar{\lambda}\mu_c}{Pr}\frac{\partial^2\tilde{T}_1}{\partial Y^2}+\frac{\bar{\lambda}\mu_c}{\tilde{P}r_T}\frac{\partial^2\tilde{T}_1(t-\hat{\tau}_1)}{\partial Y^2}-\frac{\bar{T}_{1,c}\bar{x}}{\bar{T}_c^2}\mathcal{L}_N^{\dagger}\tilde{T}_0 - \frac{\bar{\lambda}}{Pr}\left(\mu_c'+\mu_c\frac{\bar{T}_{1,c}\bar{x}}{\bar{T}_c}\right)\frac{\partial^2\tilde{T}_0}{\partial Y^2}-\frac{\tilde{\lambda}\bar{T}_{1,c}\bar{x}}{\tilde{P}r_T\bar{T}_c}\mu_c\frac{\partial^2\tilde{T}_0(t-\hat{\tau}_1)}{\partial Y^2}\right]_0, \tag{5.19}$$

where the subscript 0 indicates that the focus is on the mean-flow distortion. Due to the fact that $\partial\tilde{T}_1/\partial Y\to 0$ as $Y\to\pm\infty$, there is no need to derive the equation for $\tilde{T}_1$. Integrating (5.19) with respect to Y and noting that $(\mathcal{L}_N^{\dagger}\tilde{T}_0)|_0=0$, we obtain,

$$\tilde{v}_3|_0(Y\to\infty)-\tilde{v}_3|_0(Y\to-\infty)=-\frac{\partial}{c\partial\bar{x}}\left[\int_{-\infty}^{\infty}\tilde{u}_1\Big|_0(\tau,\bar{x},Y)\,\mathrm{d}Y\right]. \tag{5.20}$$

Taking (3.65) into account, we have,

$$\tilde{u}_1|_0=\int_{-\infty}^{Y}Q^{\dagger}|_0\,\mathrm{d}Y=\frac{p_Q}{\alpha\bar{U}_c'}\int_{-\infty}^{\eta}Q_0\,\mathrm{d}\eta. \tag{5.21}$$

The equation governing Q_0 follows from setting $n=0$ in (4.16*b*) and (4.16*c*),

$$\left(\frac{\partial}{\partial\tau}+\frac{\partial}{\partial\bar{x}}+\chi\frac{\partial}{\partial\eta}-\lambda_{10}\frac{\partial^2}{\partial\eta^2}\right)T_0+\mathrm{i}\frac{\partial}{\partial\eta}(A^*T_1-AT_1^*)=0, \tag{5.22a}$$

$$\left(\frac{\partial}{\partial\tau}+\frac{\partial}{\partial\bar{x}}+\chi\frac{\partial}{\partial\eta}-\lambda_{20}\frac{\partial^2}{\partial\eta^2}\right)Q_0+\mathrm{i}\frac{\partial}{\partial\eta}(A^*Q_1-AQ_1^*) =-\mathrm{i}p_3\frac{\partial}{\partial\eta}(A^*T_1-AT_1^*)-p_3\chi\frac{\partial T_0}{\partial\eta}-\lambda_{30}\frac{\partial^2T_0}{\partial\eta^2}. \tag{5.22b}$$

First integrating these two equations with respect to η from $-\infty$ to $(\eta-\bar{U}_{1,c}\bar{x}/\bar{U}_c')/(\alpha\bar{U}_c')$, then integrating with respect to η from $-\infty$ to ∞ again and noting that $\int_{-\infty}^{\infty}T_0\,\mathrm{d}\eta=\int_{-\infty}^{\infty}Q_0\,\mathrm{d}\eta=0$ as well as (4.16*a*), we obtain,

$$\mathcal{U}(\tau,\bar{x})\equiv\left(\frac{\partial}{\partial\tau}+\frac{\partial}{\partial\bar{x}}\right)\int_{-\infty}^{\infty}\tilde{u}_1\Big|_0\,\mathrm{d}Y =\frac{p_Q}{\alpha^2\bar{U}_c'^2}\left[-\mathrm{i}\Lambda_1\frac{\partial|A|^2}{\partial\tau}-\mathrm{i}\Lambda_2\frac{\partial|A|^2}{\partial\bar{x}}-p_3\left(\frac{\partial}{\partial\tau}+\frac{\partial}{\partial\bar{x}}\right)\int_{-\infty}^{\infty}\eta^*T_0(\eta^*)\,\mathrm{d}\eta^*\right]. \tag{5.23}$$

Noting that v_M and $\tilde{v}_3$ are both of $O(\epsilon^{5/2})$, we have, by the principle of asymptotic matching, the relation

$$v_M(y=y_c^+)-v_M(y=y_c^-)=\tilde{v}_3|_0(Y\to\infty)-\tilde{v}_3|_0(Y\to-\infty), \tag{5.24}$$

which is the first condition needed to determine $a_M^{\pm}$. It follows from (5.12) and Fourier transforms of (5.20) and (5.23)–(5.24) that

$$\mathrm{i}(\kappa-\omega)\left[\widehat{a_M^+}(\omega,\kappa)-\widehat{a_M^-}(\omega,\kappa)-\int_{-\infty}^{\infty}\frac{\widehat{\mathcal{S}}(\omega,\kappa,y)}{(\bar{U}\kappa/c-\omega)^2}\,\mathrm{d}y\right]=-\frac{\kappa\widehat{\mathcal{U}}(\omega,\kappa)}{c(\kappa-\omega)}, \tag{5.25}$$

where $\widehat{\mathcal{U}}$ denotes the Fourier transform of the right-hand side of (5.23).

https://doi.org/10.1017/jfm.2019.909 Published online by Cambridge University Press

5.3. *Asymptotic matching with the acoustic field*

Since v_M does not vanish as $y \to \pm\infty$, it induces a perturbation in the far field, which acquires the acoustic character when $y = O(\epsilon^{-1/2})$ (see figure 1). The transverse variable $\bar{y}$ defined by (3.14*a*) describes the acoustic field. The perturbation can be written as $\epsilon^{5/2}(\tilde{U}^{\pm}, \tilde{V}^{\pm}, \tilde{T}^{\pm}, \tilde{P}^{\pm})$, which are all functions of $(\tau, \bar{x}, \bar{y})$, and their governing equations follow from expansions of (2.23)–(2.26),

$$\frac{\bar{T}_{\pm}}{c}\left(\frac{\partial \tilde{U}^{\pm}}{\partial \bar{x}} + \frac{\partial \tilde{V}^{\pm}}{\partial \bar{y}}\right) = \left(\frac{\partial}{\partial \tau} + \frac{\bar{U}_{\pm}}{c}\frac{\partial}{\partial \bar{x}}\right)(\tilde{T}^{\pm} - \gamma Ma^2 \bar{T}_{\pm}\tilde{P}^{\pm}), \tag{5.26a}$$

$$\left(\frac{\partial}{\partial \tau} + \frac{\bar{U}_{\pm}}{c}\frac{\partial}{\partial \bar{x}}\right)(\tilde{U}^{\pm}, \tilde{V}^{\pm}) = -\frac{\bar{T}_{\pm}}{c}\left(\frac{\partial}{\partial \bar{x}}, \frac{\partial}{\partial \bar{y}}\right)\tilde{P}^{\pm}, \tag{5.26b}$$

$$\left(\frac{\partial}{\partial \tau} + \frac{\bar{U}_{\pm}}{c}\frac{\partial}{\partial \bar{x}}\right)\tilde{T}^{\pm} = (\gamma - 1)Ma^2 \bar{T}_{\pm}\left(\frac{\partial}{\partial \tau} + \frac{\bar{U}_{\pm}}{c}\frac{\partial}{\partial \bar{x}}\right)\tilde{P}^{\pm}, \tag{5.26c}$$

where $\bar{U}_{\pm} = (U_1^* + U_2^*)/(U_1^* - U_2^*) \pm 1$, $\bar{T}_{+} = 1$ and $\bar{T}_{-} = \beta_T$. Eliminating $\tilde{U}^{\pm}$, $\tilde{V}^{\pm}$ and $\tilde{T}^{\pm}$, we obtain a two-dimensional convected wave equation for $\tilde{P}^{\pm}$,

$$Ma^2\left(\frac{\partial}{\partial \tau} + \frac{\bar{U}_{\pm}}{c}\frac{\partial}{\partial \bar{x}}\right)^2 \tilde{P}^{\pm} - \frac{\bar{T}_{\pm}}{c^2}\left(\frac{\partial^2}{\partial \bar{x}^2} + \frac{\partial^2}{\partial \bar{y}^2}\right)\tilde{P}^{\pm} = 0, \tag{5.27}$$

subject to the Neumann boundary condition,

$$\left.\frac{\partial \tilde{P}^{\pm}}{\partial \bar{y}}\right|_{\bar{y}=0^{\pm}} = -\frac{c}{\bar{T}_{\pm}}\left(\frac{\partial}{\partial \tau} + \frac{\bar{U}_{\pm}}{c}\frac{\partial}{\partial \bar{x}}\right)^2 a_M^{\pm}(\tau, \bar{x}), \tag{5.28}$$

which follows from the vertical momentum equation in (5.26*b*) and matching with the main-layer solution (5.11). The acoustic radiation of CS is thus shown to be analogous to a classical acoustic problem represented by (5.27)–(5.28) with $a_M^{\pm}(\tau, \bar{x})$ playing the role of the equivalent acoustic sources in the acoustic analogy of Lighthill type. However, their values cannot be pre-determined, and rather have to be found along with solving the wave equation. In other words, although the sound may be viewed as being emitted by the equivalent sources, it also produces a back action on the latter. This is a significant difference from what the Lighthill type acoustical analogy envisages.

We can also solve (5.27)–(5.28) by taking double Fourier transform with respect to both τ and $\bar{x}$, which converts the system to

$$\left[\frac{\partial^2}{\partial \bar{y}^2} + \mathscr{K}_{\pm}^2(\omega, \kappa)\right]\widehat{P^{\pm}}(\omega, \kappa, \bar{y}) = 0, \tag{5.29a}$$

$$\left.\frac{\partial \widehat{P^{\pm}}}{\partial \bar{y}}\right|_{\bar{y}=0^{\pm}} = \frac{1}{c\bar{T}_{\pm}}(\bar{U}_{\pm}\kappa - c\omega)^2 \widehat{a_M^{\pm}}(\omega, \kappa), \tag{5.29b}$$

where

$$\mathscr{K}_{\pm}(\omega, \kappa) = \sqrt{Ma^2(\bar{U}_{\pm}\kappa - c\omega)^2/\bar{T}_{\pm} - \kappa^2}. \tag{5.30}$$

The solution can be written as

$$\widehat{P^{\pm}}(\omega, \kappa, \bar{y}) = \mp\widehat{\mathscr{E}}_{\pm}(\omega, \kappa)\widehat{a_M^{\pm}}(\omega, \kappa)\exp[\pm \mathrm{i}\mathscr{K}_{\pm}(\omega, \kappa)\bar{y}], \tag{5.31}$$

https://doi.org/10.1017/jfm.2019.909 Published online by Cambridge University Press

where $\widehat{\mathcal{E}}_{\pm}(\omega,\kappa)$ are determined by the boundary conditions (5.29*b*) as

$$\widehat{\mathcal{E}}_{\pm}(\omega,\kappa)=\mathrm{i}(\bar{U}_{\pm}\kappa-c\omega)^2/[c\bar{T}_{\pm}\mathscr{K}_{\pm}(\omega,\kappa)]. \tag{5.32}$$

The solution (5.31) indicates that there is a pressure jump across the main layer at $O(\epsilon^{5/2})$,

$$\widehat{P^{+}}(\bar{y}=0^{+})-\widehat{P^{-}}(\bar{y}=0^{-})=-[\widehat{\mathcal{E}}_{+}(\omega,\kappa)\widehat{a_M^{+}}(\omega,\kappa)+\widehat{\mathcal{E}}_{-}(\omega,\kappa)\widehat{a_M^{-}}(\omega,\kappa)]. \tag{5.33}$$

On the other hand, by matching with the main-layer pressure ($\epsilon^{5/2}p_{M_2}$), we have

$$\tilde{P}^{+}(\bar{y}=0^{+})-\tilde{P}^{-}(\bar{y}=0^{-})=p_{M_2}(y\to\infty)-p_{M_2}(y\to-\infty), \tag{5.34}$$

which is the second condition to determine $a_M^{\pm}$. Taking the Fourier transform of (5.34) and (5.14) and making use of (5.33), we obtain

$$-[\widehat{\mathcal{E}}_{+}(\omega,\kappa)\widehat{a_M^{+}}(\omega,\kappa)+\widehat{\mathcal{E}}_{-}(\omega,\kappa)\widehat{a_M^{-}}(\omega,\kappa)]=\widehat{\mathcal{Y}}(\omega,\kappa). \tag{5.35}$$

5.4. *Acoustic radiation of modulated coherent structures*

From (5.25) and (5.35), the Fourier transforms of the equivalent sound sources $a_M^{\pm}(\tau,\bar{x})$ are found as,

$$\widehat{a_M^{\pm}}(\omega,\kappa)=\frac{\pm\widehat{\mathcal{E}}_{\mp}(\omega,\kappa)}{\widehat{\mathcal{E}}_{+}+\widehat{\mathcal{E}}_{-}}\left[\frac{\mathrm{i}\kappa\widehat{\mathcal{U}}(\omega,\kappa)}{c(\kappa-\omega)^2}+\int_{-\infty}^{\infty}\frac{\widehat{\mathcal{S}}(\omega,\kappa,y)}{(\bar{U}\kappa/c-\omega)^2}\,\mathrm{d}y\right]-\frac{\widehat{\mathcal{Y}}(\omega,\kappa)}{\widehat{\mathcal{E}}_{+}+\widehat{\mathcal{E}}_{-}}. \tag{5.36}$$

The true physical sources correspond to $\mathcal{U}$, $\mathcal{S}$ and $\mathcal{Y}$, the first of which is contributed by the interactions in the critical layer, and the others by the interactions in the main layer. Note that the forcing terms generating these sources do not simply act on a (set of) wave-like equation(s) as in acoustic analogy. On the other hand, not all forcing terms lead to emission of sound waves. The equivalent sources are linear combinations of the three physical sources. It should be stressed again that the equivalent sources are determined in the course of calculating the radiated sound, indicating that a back action is present.

The acoustic pressure $\epsilon^{5/2}\tilde{P}^{\pm}(\tau,\bar{x},\bar{y})$ in physical space can be found by inverting Fourier transform as,

$$\tilde{P}^{\pm}(\tau,\bar{x},\bar{y})=\mp\frac{1}{4\pi^2}\int_{-\infty}^{\infty}\mathrm{e}^{-\mathrm{i}\omega\tau}\,\mathrm{d}\omega\int_{-\infty}^{\infty}\widehat{\mathcal{E}}_{\pm}(\omega,\kappa)\widehat{a_M^{\pm}}(\omega,\kappa)\mathrm{e}^{\pm\mathrm{i}\mathscr{K}_{\pm}(\omega,\kappa)\bar{y}+\mathrm{i}\kappa\bar{x}}\,\mathrm{d}\kappa. \tag{5.37}$$

Of primary interest is the acoustics in the far field, which can be approximated asymptotically using the stationary-phase method. For that purpose, the polar coordinates $(\bar{R},\bar{\theta})$, $\bar{\theta}\in[-\pi,\pi]$, are introduced, where

$$\bar{R}=\sqrt{\bar{x}^2+\bar{y}^2}\gg 1,\quad \tan\bar{\theta}=\bar{y}/\bar{x}. \tag{5.38a,b}$$

In the inner integral of (5.37), the phase functions

$$\phi_{\pm}(\omega,\kappa,\bar{\theta})=\pm\mathscr{K}_{\pm}(\omega,\kappa)\sin\bar{\theta}+\kappa\cos\bar{\theta} \tag{5.39}$$

https://doi.org/10.1017/jfm.2019.909 Published online by Cambridge University Press

have the stationary points, where $\partial\phi_{\pm}(\omega,\kappa,\bar{\theta})/\partial\kappa=0$, at

$$\kappa=\kappa_s^{\pm}(\omega,\bar{\theta})=\left[\frac{\mathrm{sgn}(\omega)\bar{T}_{\pm}\cos\bar{\theta}}{\sqrt{\bar{T}_{\pm}-Ma^2\bar{U}_{\pm}^2\sin^2\bar{\theta}}}-Ma\bar{U}_{\pm}\right]\frac{Mac\omega}{\bar{T}_{\pm}-Ma^2\bar{U}_{\pm}^2}. \tag{5.40}$$

It can be readily verified that $\kappa_s^{\pm}$ is in the region that leads to a wave form, i.e.

$$Ma^2(\bar{U}_{\pm}\kappa_s^{\pm}-c\omega)^2/\bar{T}_{\pm}-\kappa_s^{\pm 2}>0. \tag{5.41}$$

The far-field pressure in the region $\bar{R}\gg 1$ is given by

$$\begin{aligned}\tilde{P}^{\pm}(\tau,\bar{R},\bar{\theta})\ \rightarrow\ &\mp\frac{\sqrt{2\pi}}{4\pi^2\sqrt{\bar{R}}}\int_{-\infty}^{\infty}\frac{\mathrm{e}^{\mathrm{sgn}[\phi''_{\pm}(\omega,\kappa_s^{\pm},\bar{\theta})]\mathrm{i}\pi/4}}{\sqrt{|\phi''_{\pm}(\omega,\kappa_s^{\pm},\bar{\theta})|}}\\&\times\widehat{\mathcal{E}}_{\pm}(\omega,\kappa_s^{\pm})\widehat{a_M^{\pm}}(\omega,\kappa_s^{\pm})\mathrm{e}^{\mathrm{i}\phi_{\pm}(\omega,\kappa_s^{\pm},\bar{\theta})\bar{R}-\mathrm{i}\omega\tau}\,\mathrm{d}\omega,\end{aligned} \tag{5.42}$$

where

$$\phi''_{\pm}(\omega,\kappa_s^{\pm},\bar{\theta})=\frac{\pm(Ma^2\bar{U}_{\pm}^2-\bar{T}_{\pm})\sin\bar{\theta}}{\sqrt{T_{\pm}Ma^2(\bar{U}_{\pm}\kappa_s^{\pm}-c\omega)^2-\bar{T}_{\pm}^2\kappa_s^{\pm 2}}}+\frac{Ma^2\bar{U}_{\pm}(\bar{U}_{\pm}\kappa_s^{\pm}-c\omega)-\bar{T}_{\pm}\kappa_s^{\pm}}{Ma^2(\bar{U}_{\pm}\kappa_s^{\pm}-c\omega)^2-\bar{T}_{\pm}\kappa_s^{\pm 2}}\cos\bar{\theta}. \tag{5.43}$$

Obviously, $(\mathrm{i}\kappa_s^{\pm})^{-1}\widehat{\mathcal{E}}_{\pm}(\omega,\kappa_s^{\pm})$ and $\kappa_s^{\pm}\phi''_{\pm}(\omega,\kappa_s^{\pm},\bar{\theta})$ are functions only of the radiation angle $\bar{\theta}$, and so we could introduce two 'auxiliary functions' $\Theta_{\pm}(\bar{\theta})$ and $\mathscr{S}_{\pm}(\omega,\bar{\theta})$ as

$$\Theta_{\pm}(\bar{\theta})=\frac{(\mathrm{i}\kappa_s^{\pm})^{-1}\widehat{\mathcal{E}}_{+}(\omega,\kappa_s^{\pm})\widehat{\mathcal{E}}_{-}(\omega,\kappa_s^{\pm})}{\widehat{\mathcal{E}}_{+}(\omega,\kappa_s^{\pm})+\widehat{\mathcal{E}}_{-}(\omega,\kappa_s^{\pm})}|\kappa_s^{\pm}\phi''_{\pm}(\omega,\kappa_s^{\pm},\bar{\theta})|^{-1/2}, \tag{5.44}$$

$$\mathscr{S}_{\pm}(\omega,\bar{\theta})=\mathrm{i}\kappa_s^{\pm}\sqrt{|\kappa_s^{\pm}|}\left[\frac{\mathrm{i}\kappa\widehat{\mathcal{U}}(\omega,\kappa)}{c(\kappa_s^{\pm}-\omega)^2}+\int_{-\infty}^{\infty}\frac{\widehat{\mathcal{S}}(\omega,\kappa_s^{\pm},y)}{(\bar{U}\kappa_s^{\pm}/c-\omega)^2}\,\mathrm{d}y\mp\frac{\widehat{\mathcal{Y}}(\omega,\kappa_s^{\pm})}{\widehat{\mathcal{E}}_{\mp}(\omega,\kappa_s^{\pm})}\right]. \tag{5.45}$$

In terms of $\Theta_{\pm}$ and $\mathscr{S}_{\pm}$, the acoustic pressure (5.42) in the far field is expressed as

$$\tilde{P}^{\pm}\rightarrow-\frac{\Theta_{\pm}(\bar{\theta})}{(2\pi)^{3/2}\sqrt{\bar{R}}}\int_{-\infty}^{\infty}\mathrm{e}^{\mathrm{sgn}[\phi''_{\pm}(\omega,\kappa_s^{\pm},\bar{\theta})]\mathrm{i}\pi/4}\mathscr{S}_{\pm}(\omega,\bar{\theta})\mathrm{e}^{\mathrm{i}\phi_{\pm}(\omega,\kappa_s^{\pm},\bar{\theta})\bar{R}-\mathrm{i}\omega\tau}\,\mathrm{d}\omega. \tag{5.46}$$

The overall intensity of the acoustic pressure is measured by the root-mean-square value of $\tilde{P}^{\pm}$, which is, according to Parseval's theorem, given by

$$\tilde{P}^{\pm}_{rms}(\bar{R},\bar{\theta})\rightarrow\sqrt{\overline{|\tilde{P}^{\pm}|^2}}=\frac{1}{(2\pi)^{5/2}}\frac{\mathscr{D}_{\pm}(\bar{\theta})}{\sqrt{\bar{R}}}; \tag{5.47}$$

here $\mathscr{D}_{\pm}(\bar{\theta})$ is the directivity function,

$$\mathscr{D}_{\pm}(\bar{\theta})=|\Theta_{\pm}(\bar{\theta})|\sqrt{\int_{-\infty}^{\infty}|\mathscr{S}_{\pm}(\omega,\bar{\theta})|^2\,\mathrm{d}\omega}, \tag{5.48}$$

which indicates that $\mathscr{D}_{\pm}(\bar{\theta})$ is a superimposition of the corresponding spectrum function $|\mathscr{S}_{\pm}(\omega,\bar{\theta})|$ at a radiation direction $\bar{\theta}$.

https://doi.org/10.1017/jfm.2019.909 Published online by Cambridge University Press

6. Numerical solutions

6.1. *Non-parallel mean-flow profiles*

The theory is applied to a compressible mixing layer, which is formed by two streams with velocities U_1^* and $U_2^* < U_1^*$. The mean streamwise-velocity profile is chosen to be

$$\bar{U}[\eta^\dagger(y,\tilde{x})] = \bar{U}_R + f(\eta^\dagger), \tag{6.1}$$

with

$$\bar{U}_R = \frac{U_1^* + U_2^*}{U_1^* - U_2^*}, \quad \eta^\dagger = \eta_{c,0}^\dagger + \frac{y - y_0(\tilde{x})}{\delta(\tilde{x})}, \tag{6.2a,b}$$

where $f(\eta^\dagger)$ is a function satisfying $f(\pm\infty) = \pm 1$, y_0 and δ represent the centre and thickness of the mixing layer respectively, and they are both functions of $\tilde{x}$ defined by (3.6). The parameter $\eta_{c,0}^\dagger$ is assigned to ensure that the critical level (the generalised inflection point) is located at $y = y_0(0) = 0$ at the neutral position $\tilde{x} = 0$. Equation (6.1) indicates that the mean-flow profile remains self-similar in the streamwise direction, and the phase speed of the neutral mode c is given by

$$c = \bar{U}_c = \bar{U}[\eta^\dagger(y_0(\tilde{x}),\tilde{x})] = \bar{U}_R + f(\eta_{c,0}^\dagger). \tag{6.3}$$

The dimensional momentum thickness θ^*, which is often measured in experiments, is given by

$$\theta^* = \mathscr{C}_1 \delta \delta_0^*, \tag{6.4}$$

where the constant $\mathscr{C}_1$ is found as

$$\mathscr{C}_1 = \left(\frac{\bar{U}_+^2}{\bar{T}_+} - \frac{\bar{U}_+\bar{U}_-}{\bar{T}_+} - \frac{\bar{U}_+\bar{U}_-}{\bar{T}_-} + \frac{\bar{U}_-^2}{\bar{T}_-} \right)^{-1} \int_{-\infty}^{\infty} \frac{[\bar{U}_+ - \bar{U}(\eta^\dagger)][\bar{U}(\eta^\dagger) - \bar{U}_-]}{\bar{T}(\eta^\dagger)} \,\mathrm{d}\eta^\dagger. \tag{6.5}$$

Differentiation (6.4) with respect to the dimensional streamwise length x^* gives

$$\frac{\mathrm{d}\theta^*/\mathrm{d}x^*}{\epsilon \mathscr{C}_1} = \sigma \bar{\lambda}^{2/3} \dot{\delta}, \tag{6.6}$$

where the dot over a quantity represents the differentiation with respect to $\tilde{x}$. The quantities characterising non-parallelism are all proportional to $\hat{\delta} \equiv \sigma \bar{\lambda}^{2/3} \dot{\delta}$.

As previously stated, the normal velocity of the mean flow appears at leading order in the evolution system (4.3), which can be determined by the profiles of $\bar{U}$ and $\bar{T}$ as follows. The mean-flow quantities, $\bar{U}$, $\bar{V}$, $\bar{T}$, etc., depend on $\tilde{x}$ (defined in (3.6)) and y. The streamwise momentum equation of the mean flow (3.8) can be rewritten by subtracting out $\bar{U}_\pm$ for $y > 0$ and $y < 0$ respectively as

$$\bar{\rho}\bar{U}\frac{\partial(\bar{U} - \bar{U}_\pm)}{\partial \tilde{x}} + \bar{\rho}\bar{V}\frac{\partial(\bar{U} - \bar{U}_\pm)}{\partial y} = \frac{\partial}{\partial y}\mu_t \frac{\partial \bar{U}}{\partial y}, \tag{6.7}$$

which can, by using (3.7), be converted to

$$\frac{\partial \bar{\rho}\bar{U}(\bar{U} - \bar{U}_\pm)}{\partial \tilde{x}} + \frac{\partial \bar{\rho}\bar{V}(\bar{U} - \bar{U}_\pm)}{\partial y} = \frac{\partial}{\partial y}\mu_t \frac{\partial \bar{U}}{\partial y}. \tag{6.8}$$

https://doi.org/10.1017/jfm.2019.909 Published online by Cambridge University Press

Integrating (6.8) first with respect to y from $-\infty$ to ∞ and then with respect to $\tilde{x}$, we obtain

$$\int_{-\infty}^{0} \bar{\rho}\bar{U}(\bar{U}-\bar{U}_-)\,\mathrm{d}y + \int_{0}^{\infty} \bar{\rho}\bar{U}(\bar{U}-\bar{U}_+)\,\mathrm{d}y = \mathscr{C}_0 + \int_0^{\tilde{x}} \mathscr{C}_V(\xi)\,\mathrm{d}\xi, \tag{6.9}$$

where $\mathscr{C}_0$ is a constant and

$$\mathscr{C}_V(\tilde{x}) = -(\bar{U}_+ - \bar{U}_-)\bar{V}_{c,0}(\tilde{x})/\bar{T}_{c,0}(\tilde{x}). \tag{6.10}$$

After changing to the variable (6.2*b*), equation (6.9) becomes,

$$\int_{-\infty}^{\eta^\dagger_{c,0}-y_0/\delta} \bar{\rho}\bar{U}(\bar{U}-\bar{U}_-)\,\mathrm{d}\eta^\dagger + \int_{\eta^\dagger_{c,0}-y_0/\delta}^{\infty} \bar{\rho}\bar{U}(\bar{U}-\bar{U}_+)\,\mathrm{d}\eta^\dagger = \frac{\mathscr{C}_0}{\delta} + \frac{1}{\delta}\int_0^{\tilde{x}} \mathscr{C}_V(\xi)\,\mathrm{d}\xi. \tag{6.11}$$

On differentiating this equation with respect to $\tilde{x}$, we have,

$$\bar{\rho}_{c,0}\bar{U}_{c,0}(\bar{U}_+ - \bar{U}_-)(-\dot{y}_0\delta + y_0\dot{\delta}) = -\dot{\delta}\mathscr{C}_0 + \delta\mathscr{C}_V - \dot{\delta}\int_0^{\tilde{x}} \mathscr{C}_V(\xi)\,\mathrm{d}\xi, \tag{6.12}$$

where the subscript $(c,0)$ denotes the quantities evaluated $\eta^\dagger = \eta^\dagger_{c,0} - y_0(\tilde{x})/\delta(\tilde{x})$.

The normal velocity $\bar{V}$ can be derived from the continuity equation (3.7) by defining the streamfunction $\Psi_B(\tilde{x}, y)$ or $\Psi[\tilde{x}, \eta^\dagger(\tilde{x}, y)]$, which satisfies the relations,

$$\bar{\rho}\bar{U} = \frac{\partial \Psi_B}{\partial y} = \frac{1}{\delta}\frac{\partial \Psi}{\partial \eta^\dagger}, \quad \bar{\rho}\bar{V} = -\frac{\partial \Psi_B}{\partial \tilde{x}} = \frac{\dot{y}_0 + (\eta^\dagger - \eta^\dagger_{c,0})\dot{\delta}}{\delta}\frac{\partial \Psi}{\partial \eta^\dagger} - \frac{\partial \Psi}{\partial \tilde{x}}. \tag{6.13a,b}$$

Noting that $\bar{\rho} = 1/\bar{T}$ and integrating (6.13*a*), we have

$$\Psi = \delta\int_{-\infty}^{\eta^\dagger}\left[\frac{\bar{U}(\eta^\star)}{\bar{T}(\eta^\star)} - \frac{\bar{U}_-}{\bar{T}_-}\right]\mathrm{d}\eta^\star + \frac{\bar{U}_-}{\bar{T}_-}(\eta^\dagger - \eta^\dagger_{c,0})\delta + d_0(\tilde{x}), \tag{6.14}$$

where $d_0(\tilde{x})$ is an arbitrary function of $\tilde{x}$. The vertical velocity $\bar{V}$ follows from differentiating (6.14) with respect to $\tilde{x}$,

$$\begin{aligned}\bar{V}(\eta^\dagger, \tilde{x}) \;=\; & \bar{U}[\dot{y}_0 + (\eta^\dagger - \eta^\dagger_{c,0})\dot{\delta}] - \bar{T}\dot{\delta}\int_{-\infty}^{\eta^\dagger}[\bar{U}(\eta^\star)/\bar{T}(\eta^\star) - \bar{U}_-/\bar{T}_-]\,\mathrm{d}\eta^\star \\ & - (\bar{U}_-/\bar{T}_-)\bar{T}(\eta^\dagger - \eta^\dagger_{c,0})\dot{\delta} - \bar{T}\dot{d}_0.\end{aligned} \tag{6.15}$$

In order to determine $d_0(\tilde{x})$, it is necessary to analyse the impact of the shear layer on the inviscid mean flow in the far field. First, we take the limit $\eta^\dagger \to \pm\infty$ to show that

$$\bar{V} \to \bar{V}_\pm = \bar{U}_\pm\dot{y}_0(\tilde{x}) - \bar{T}_\pm[\dot{d}_0(\tilde{x}) + \mathscr{C}_T^\pm\dot{\delta}] \quad \text{as } \eta^\dagger \to \pm\infty, \tag{6.16}$$

where $\mathscr{C}_T^\pm$ are constants,

$$\mathscr{C}_T^- = 0, \quad \mathscr{C}_T^+ = \int_{-\infty}^{\eta^\dagger_{c,0}}(\bar{U}/\bar{T} - \bar{U}_-/\bar{T}_-)\,\mathrm{d}\eta + \int_{\eta^\dagger_{c,0}}^{\infty}(\bar{U}/\bar{T} - \bar{U}_+/\bar{T}_+)\,\mathrm{d}\eta, \tag{6.17a,b}$$

https://doi.org/10.1017/jfm.2019.909 Published online by Cambridge University Press

and $\bar{V}_\pm$ are the so-called transpiration velocities induced by the viscous motion in the shear layer. Through $\bar{V}_\pm$, an $O(R_T^{-1})$ perturbation $R_T^{-1}(\hat{u}^\pm, \hat{v}^\pm, \hat{T}^\pm, \hat{p}^\pm)$ is induced in the far field, where $\tilde{x}, \tilde{y} = O(1)$ (see (3.14*b*) and figure 1). The perturbation satisfies the equations,

$$\begin{cases} \bar{T}_\pm \left(\dfrac{\partial \hat{u}^\pm}{\partial \tilde{x}} + \dfrac{\partial \hat{v}^\pm}{\partial \tilde{y}} \right) = \bar{U}_\pm \dfrac{\partial \hat{T}^\pm}{\partial \tilde{x}} - \gamma Ma^2 \bar{T}_\pm \bar{U}_\pm \dfrac{\partial \hat{p}^\pm}{\partial \tilde{x}}, & (6.18a) \\ \bar{U}_\pm \dfrac{\partial}{\partial \tilde{x}} (\hat{u}^\pm, \hat{v}^\pm) = -\bar{T}_\pm \left(\dfrac{\partial}{\partial \tilde{x}}, \dfrac{\partial}{\partial \tilde{y}} \right) \hat{p}^\pm, & (6.18b) \\ \dfrac{\partial \hat{T}^\pm}{\partial \tilde{x}} = (\gamma - 1) Ma^2 \bar{T}_\pm \dfrac{\partial \hat{p}^\pm}{\partial \tilde{x}}, & (6.18c) \end{cases}$$

from which we can obtain the equation for $\hat{p}^\pm$ and its boundary condition,

$$\left(1 - \frac{\bar{U}_\pm^2 Ma^2}{\bar{T}_\pm} \right) \frac{\partial^2 \hat{p}^\pm}{\partial \tilde{x}^2} + \frac{\partial^2 \hat{p}^\pm}{\partial \tilde{y}^2} = 0, \quad \left. \frac{\partial \hat{p}^\pm}{\partial \tilde{y}} \right|_{\tilde{y}=0^\pm} = -\frac{\bar{U}_\pm}{\bar{T}_\pm} \frac{\partial \bar{V}_\pm}{\partial \tilde{x}}, \tag{6.19a,b}$$

where $\bar{U}_\pm Ma / \sqrt{\bar{T}_\pm} < 1$ holds for the subsonic regime, and the boundary condition follows from the vertical momentum equation in (6.18*b*) and matching $\hat{v}_\pm$ with the transpiration velocities $\bar{V}_\pm$.

Introducing the re-scaled variable $\mathscr{Y} = \mathscr{P}_\pm \tilde{y} = \sqrt{1 - \bar{U}_\pm^2 Ma^2 / \bar{T}_\pm}\, \tilde{y}$, we rewrite (6.19) into the standard Laplace equation and the corresponding boundary condition as,

$$\nabla^2 \hat{p}^\pm = 0, \quad \left. \frac{\partial \hat{p}^\pm}{\partial \mathscr{Y}} \right|_{\mathscr{Y}=0^\pm} = -\frac{\bar{U}_\pm}{\mathscr{P}_\pm \bar{T}_\pm} \frac{\partial \bar{V}_\pm}{\partial \tilde{x}}. \tag{6.20a,b}$$

Additionally, the mixing layer is too thin to withstand any difference of the pressure, that is, $\hat{p}^+ = \hat{p}^-$ at $\tilde{y} = 0$, which requires that $\bar{U}_+ \bar{V}_+ / (\mathscr{P}_+ \bar{T}_+) = -\bar{U}_- \bar{V}_- / (\mathscr{P}_- \bar{T}_-)$. Combining this with (6.16), we find that

$$\dot{d}_0 = \frac{\bar{U}_+^2 \bar{T}_- \mathscr{P}_- + \bar{U}_-^2 \bar{T}_+ \mathscr{P}_+}{\bar{T}_+ \bar{T}_- (\bar{U}_+ \mathscr{P}_- + \bar{U}_- \mathscr{P}_+)} \dot{y}_0 - \frac{\bar{U}_+ \mathscr{C}_T^+ \mathscr{P}_- + \bar{U}_- \mathscr{C}_T^- \mathscr{P}_+}{\bar{U}_+ \mathscr{P}_- + \bar{U}_- \mathscr{P}_+} \dot{\delta}. \tag{6.21}$$

Specifically, at the neutral position $\tilde{x} = 0$, we have $\delta(0) = 1$ and $y_0(0) = 0$, use of which in (6.11) and (6.12) gives

$$\int_{-\infty}^{\eta_{c,0}^\dagger} \bar{U}(\bar{U} - \bar{U}_-)/\bar{T}\, \mathrm{d}\eta^\dagger + \int_{\eta_{c,0}^\dagger}^{\infty} \bar{U}(\bar{U} - \bar{U}_+)/\bar{T}\, \mathrm{d}\eta^\dagger = \mathscr{C}_0, \tag{6.22}$$

$$-\bar{U}_c(\bar{U}_+ - \bar{U}_-)\dot{y}_0 = -\bar{T}_c \mathscr{C}_0 \dot{\delta} - (\bar{U}_+ - \bar{U}_-)\bar{V}_c(0). \tag{6.23}$$

The required value $\bar{V}_c(0)$ is found from (6.15) by setting $\eta^\dagger = \eta_{c,0}^\dagger$ and $\tilde{x} = 0$ as,

$$\bar{V}_c(0) = \bar{U}_c \dot{y}_0 - \bar{T}_c(\dot{d}_0 + \mathscr{C}_h \dot{\delta}) \quad \text{with } \mathscr{C}_h = \int_{-\infty}^{\eta_{c,0}^\dagger} (\bar{U}/\bar{T} - \bar{U}_-/\bar{T}_-)\, \mathrm{d}\eta^\dagger. \tag{6.24}$$

From (6.21) and (6.23)–(6.24), we find that $\dot{d}_0$, $\dot{y}_0$ and hence $\bar{V}_c$ are all proportional to $\dot{\delta}$,

$$\dot{d}_0 = \left(\frac{\mathscr{C}_0}{\bar{U}_+ - \bar{U}_-} - \mathscr{C}_h \right) \dot{\delta}, \tag{6.25}$$

https://doi.org/10.1017/jfm.2019.909 Published online by Cambridge University Press

$$\dot{y}_0 = \frac{\bar{T}_+\bar{T}_-(\bar{U}_+\mathscr{P}_- + \bar{U}_-\mathscr{P}_+)}{\bar{U}_+^2\bar{T}_-\mathscr{P}_- + \bar{U}_-^2\bar{T}_+\mathscr{P}_+}\left(\frac{\mathscr{C}_0}{\bar{U}_+ - \bar{U}_-} - \mathscr{C}_h + \frac{\bar{U}_+\mathscr{C}_T^+\mathscr{P}_-}{\bar{U}_+\mathscr{P}_- + \bar{U}_-\mathscr{P}_+}\right)\dot{\delta}, \quad (6.26)$$

$$\begin{aligned}\bar{V}_c(0) \;=\; & \frac{\bar{U}_c\bar{T}_+\bar{T}_-(\bar{U}_+\mathscr{P}_- + \bar{U}_-\mathscr{P}_+)}{\bar{U}_+^2\bar{T}_-\mathscr{P}_- + \bar{U}_-^2\bar{T}_+\mathscr{P}_+}\left(\frac{\mathscr{C}_0}{\bar{U}_+ - \bar{U}_-} - \mathscr{C}_h + \frac{\bar{U}_+\mathscr{C}_T^+\mathscr{P}_-}{\bar{U}_+\mathscr{P}_- + \bar{U}_-\mathscr{P}_+}\right)\dot{\delta} \\ & - \frac{\bar{T}_c\mathscr{C}_0}{\bar{U}_+ - \bar{U}_-}\dot{\delta}. \end{aligned} \quad (6.27)$$

The choice of the mean-temperature profile is now discussed. When a unit turbulent Prandtl number Pr_T is assumed, $\bar{T}$ is related to $\bar{U}$ via usual Crocco–Busemann relation similar to the laminar case. If $Pr_T \neq 1$ but still a constant, there is an empirical formula,

$$\bar{T}(\eta^\dagger) = -r\frac{(\gamma-1)Ma^2}{2}(\bar{U}-\bar{U}_-)(\bar{U}-\bar{U}_+) + \frac{1-\beta_T}{2}(\bar{U}-\bar{U}_-) + \beta_T, \quad (6.28)$$

where r is referred to as the recovery factor, and in the turbulent case $r = Pr_T{}^{1/3}$ was proposed (Persh & Lee 1956), but $r = Pr^{1/2}$ was taken for the laminar case (Schlichting 1979, pp. 334–335, pp. 713–714); for either choice the formula reduces to the usual Crocco–Busemann relation when $Pr_T = 1$ or $Pr = 1$. Alternatively, $\bar{T}$ may be obtained from the energy equation (3.9) together with the momentum equation (3.8). Substituting (6.2*b*), (6.15) and (6.25) into (3.8)–(3.9), we have the coupled equations for $\bar{T}(\eta^\dagger)$ with the eddy viscosity $\mu_t(\eta^\dagger)$ and an auxiliary function $\bar{G}(\eta^\dagger)$ as,

$$\begin{cases} \dfrac{1}{Pr_T}\dfrac{\mathrm{d}}{\mathrm{d}\eta^\dagger}\mu_t\dfrac{\mathrm{d}\bar{T}}{\mathrm{d}\eta^\dagger} + \bar{G}\dfrac{\mathrm{d}\bar{T}}{\mathrm{d}\eta^\dagger} + (\gamma-1)Ma^2\mu_t\dfrac{\mathrm{d}\bar{U}}{\mathrm{d}\eta^\dagger}\dfrac{\mathrm{d}\bar{U}}{\mathrm{d}\eta^\dagger} = 0, & (6.29a) \\ \dfrac{\mathrm{d}}{\mathrm{d}\eta^\dagger}\mu_t\dfrac{\mathrm{d}\bar{U}}{\mathrm{d}\eta^\dagger} + \bar{G}\dfrac{\mathrm{d}\bar{U}}{\mathrm{d}\eta^\dagger} = 0, & (6.29b) \\ \dfrac{\mathrm{d}\bar{G}}{\mathrm{d}\eta^\dagger} = \dfrac{\bar{U}}{\bar{T}}\dot{\delta}, & (6.29c) \end{cases}$$

subject to the boundary conditions

$$\bar{T} \to \bar{T}_\pm \quad \text{as } \eta^\dagger \to \pm\infty; \qquad (\mu_t, \bar{G}) \to (1, \bar{G}_+(\eta^\dagger)\dot{\delta}) \quad \text{as } \eta^\dagger \to \infty, \quad (6.30a,b)$$

with

$$\bar{G}_+(\eta^\dagger) = (\bar{U}_+/\bar{T}_+)(\eta^\dagger - \eta^\dagger_{c,0}) + \mathscr{C}_T^+ + \mathscr{C}_0/(\bar{U}_+ - \bar{U}_-) - \mathscr{C}_h. \quad (6.31)$$

Here, we select a velocity profile $f(\eta^\dagger)$ as

$$f(\eta^\dagger) = (1 + q_c\mathrm{sech}^2\eta^\dagger)\tanh\eta^\dagger, \quad (6.32)$$

where the parameter q_c characterising the shape of the mean-flow profile is assigned a value to fit experimental data (Wu & Zhuang 2016).

For a given similarity profile F, which may represent $\bar{U}$, $\bar{T}$, $\bar{U}''$ and so on, its streamwise derivative is found as

$$F_1 = \sigma\bar{\lambda}^{2/3}c\left.\frac{\partial F}{\partial\tilde{x}}\right|_{\tilde{x}=0} = \sigma\bar{\lambda}^{2/3}c\frac{\mathrm{d}F}{\mathrm{d}\eta^\dagger}\left.\frac{\partial\eta^\dagger}{\partial\tilde{x}}\right|_{\tilde{x}=0} = -\sigma\bar{\lambda}^{2/3}c[\dot{y}_0 + (\eta^\dagger - \eta^\dagger_{c,0})\dot{\delta}]F'. \quad (6.33)$$

https://doi.org/10.1017/jfm.2019.909 Published online by Cambridge University Press

Inserting them into (3.41) shows that J_0 can be written as $J_0 = \hat{J}_0\dot{\delta}$, where

$$\hat{J}_0 = -\sigma\bar{\lambda}^{2/3}c\int_{-\infty}^{\infty}\frac{\bar{T}}{(\bar{U}-c)^2}(\hat{\mathcal{G}}_{01}\hat{p}_0'\hat{p}_0+\alpha^2\hat{\mathcal{G}}_{02}\hat{p}_0^2)\left(\eta^\dagger-\eta_{c,0}^\dagger+\frac{\dot{y}_0}{\dot{\delta}}\right)\mathrm{d}\eta^\dagger, \tag{6.34}$$

with

$$\hat{\mathcal{G}}_{01}=\frac{2[\bar{U}'\bar{U}'-(\bar{U}-c)\bar{U}'']}{(\bar{U}-c)^2}-\frac{\bar{T}'\bar{T}'-\bar{T}\bar{T}''}{\bar{T}^2},\quad \hat{\mathcal{G}}_{02}=\frac{Ma^2(\bar{U}-c)}{\bar{T}^2}[2\bar{U}'\bar{T}-(\bar{U}-c)\bar{T}']. \tag{6.35a,b}$$

Thus, the parameters characterising the non-parallelism are all proportional to $\dot{\delta}$ or $\hat{\delta}$, which is related to the physical quantity $\mathrm{d}\theta^*/\mathrm{d}x^*$ as (6.6) shows.

6.2. *Numerical methods*

The core numerical work is to solve the evolution system (4.3), which consists of the amplitude equation (4.27*a*) for $A^{(m)}$, the temperature equation (4.27*b*) for $T_n^{(m)}$ and the vorticity equation (4.27*c*) for $Q_n^{(m)}$, subject to the initial conditions (4.6), (4.7) and (4.13) as well as the boundary conditions (4.18)–(4.19). The system is truncated in the region $-10\leqslant\bar{x}\leqslant 20$ and $-80\leqslant\eta\leqslant 80$, with the step sizes $\Delta x=0.001$ and $\Delta\eta=0.005$. The Fourier series for T_n and Q_n consist of 20 harmonics, i.e. $-20\leqslant n\leqslant 20$. The calculations for sidebands are carried out for 8 modes on each side ($-8\leqslant m\leqslant 8$) in the discrete case, and for 64 sample points within a spectrum ($-32\leqslant m\leqslant 32$) in the continuous case for each harmonic. The equations for $T_n^{(m)}$ and $Q_n^{(m)}$ are discretised by the Crank–Nicolson scheme. The amplitude equation is marched downstream using a predictor–corrector scheme consisting of a three-step Adams explicit and two-step implicit schemes for the predictor and the corrector respectively.

For given mean velocity and temperature profiles (with the latter being obtained by using (6.28) for $Pr_T=1$), the compressible Rayleigh equation is solved numerically first to find the wavenumber α and eigenfunction of the neutral mode, and then the parameters such as $\mathscr{C}_0$, $\mathscr{C}_1$, $\mathscr{C}_T$, J_1, J_2 and $\hat{J}_0$ are evaluated. Among these, the integrands of J_1, J_2 and $\hat{J}_0$ consist of a singularity in the form of fourth-order pole $(\eta^\dagger-\eta_c^\dagger)^{-4}$, and these integrals must be interpreted as the Hadamard finite parts, which are defined according to the asymptotic behaviour of the integrand as follows. Let $f(t)$ be differentiable up to order $(n-1)$ at $t=s$. Then, one may define the finite part integral that

$$\int_a^b\frac{f(t)}{(t-s)^{n+1}}\,\mathrm{d}t=\lim_{\varepsilon\to 0}\left[\left(\int_a^{s-\varepsilon}+\int_{s+\varepsilon}^b\right)\frac{f(t)}{(t-s)^{n+1}}\,\mathrm{d}t-R_n(s,\varepsilon)\right], \tag{6.36}$$

where R_n are the divergent parts

$$R_0(s,\varepsilon)=0,\quad R_n(s,\varepsilon)=\sum_{k=0}^{n-1}\frac{f^{(k)}(s)}{k!}\left[\frac{1-(-1)^{n-k}}{(n-k)\varepsilon^{n-k}}\right]\quad\text{for } n>0. \tag{6.37a,b}$$

6.3. *Numerical results for single-frequency coherent structures*

The evolution system contains several parameters, which influence the dynamics of CS. These include the dimensionless velocity $\bar{U}_R$, the spreading rate of shear-layer thickness $\mathrm{d}\theta^*/\mathrm{d}x^*$ (represented by $\hat{\delta}$), the Mach number Ma, the Reynolds number Re

https://doi.org/10.1017/jfm.2019.909 Published online by Cambridge University Press

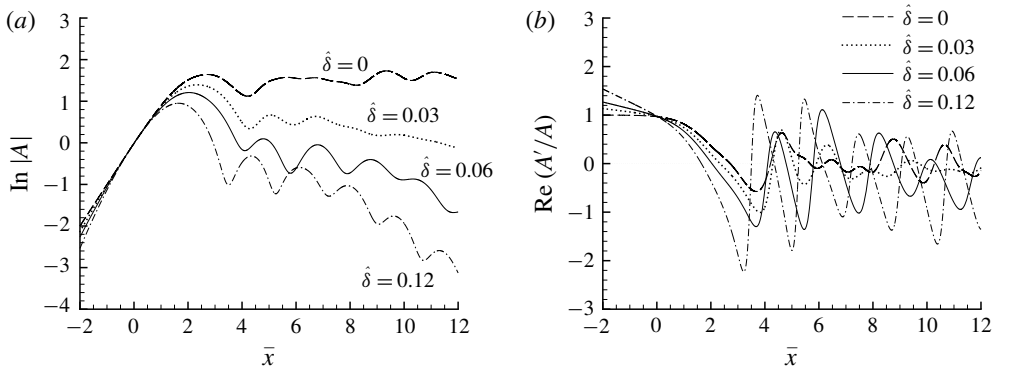

FIGURE 2. Nonlinear dynamics of CS for different spreading rates of the shear-layer momentum thickness $\hat{\delta}=0$, 0.03, 0.06 and 0.12. (*a*) The evolution of the amplitude A; (*b*) the instantaneous growth rate $\mathrm{Re}(A'/A)$.

(represented by $\bar{\lambda}$), the mean temperature ratio β_T, q_c controlling the velocity profile shape, Prandtl number Pr and the time delays $\hat{\tau}_1$ and $\hat{\tau}_2$. For the present closure model, it is necessary to restrict $\tilde{\lambda}_i \leqslant \bar{\lambda}_i$ $(i=1,\,2)$ if $\hat{\tau}_i \neq 0$ $(i=1,\,2)$. We choose the limit condition $\tilde{\lambda}_i = \bar{\lambda}_i$ $(i=1,\,2)$ to allow for maximum effects of small-scale fluctuations (cf. Wu & Zhuang 2016). The Mach number Ma is related to the Mach number of the fast upstream, Ma_1, via $Ma = Ma_1/(\bar{U}_R+1)$. Other physical parameters are simply taken to be $\gamma=1.4$, $Pr=0.7$ and $Pr_T=1$, as their values do not vary or affect the dynamics significantly. The remaining coefficients are assigned reasonable values, for example $\sigma=1$, $S_0=[\mathrm{Re}(\mathrm{i}/c_g)]^{-1}$, which amounts to rescaling the linear growth rate to unity for different cases, and $\epsilon=0.09$.

6.3.1. *The development of the coherent structure amplitude*

Unless stated otherwise, the parameters in the following cases take the values in the baseline marked '$\mathcal{F}$', including the dimensionless velocity $\bar{U}_R=7/3$, the Mach number $Ma_1=0.3$, the temperature ratio $\beta_T=7/8$, the viscosity coefficient $\bar{\lambda}=0.005$, the phase lags, which are transformed from the time delays, $\hat{\theta}_1=\hat{\theta}_2=\pi/5$ $(\hat{\theta}_i=\alpha c\hat{\tau}_i)$, the spreading rate of the shear-layer thickness $\hat{\delta}=0.06$ and the shape parameter $q_c=0.67$.

As mentioned above, the non-parallelism is associated with $\hat{\delta}$: the greater its value is, the stronger is the non-parallelism. In order to study its effect, calculations were carried out for $\hat{\delta}=0$, 0.03, 0.06 and 0.12. The amplitude evolution and the instantaneous growth rate are shown in figure 2. With the parallel-flow assumption $(\hat{\delta}=0)$, the amplitude undergoes oscillatory saturation. The combined effect of nonlinearity and non-parallelism leads to its oscillatory decay. Non-parallelism suppresses the amplitude, causing it to attenuate below the value attained in the parallel case. The oscillatory character of the amplitude and the repeated change of the sign of the instantaneous growth rate indicate significant jittering, which is important for acoustic radiation.

The compressibility is measured by Ma. The amplitude development for different $Ma_1<1$ is displayed in figure 3(*a*) for two spreading rates of the shear layer. Compressibility exerts little influence in the linear stage, but enhances appreciably the amplitude of CS in the nonlinear regime. Compressibility causes a greater degree of undulation if non-parallelism is suppressed, but does not if the latter is included.

https://doi.org/10.1017/jfm.2019.909 Published online by Cambridge University Press

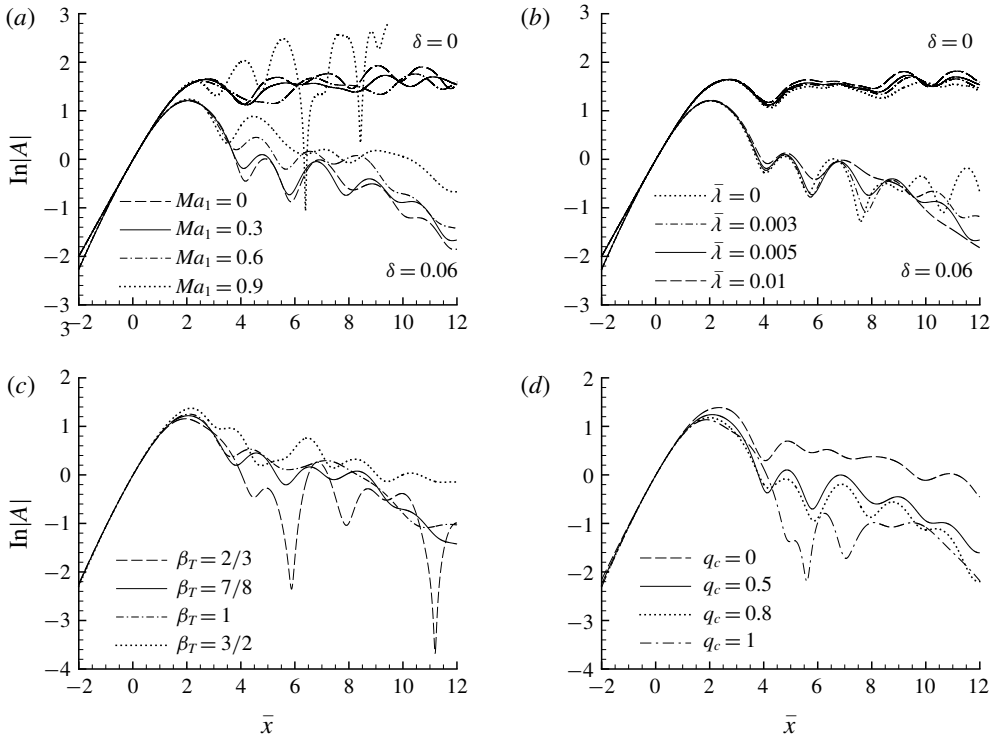

FIGURE 3. The evolution of the amplitude A for different parameter values: (a) Mach numbers of the fast upstream $Ma_1 = 0$, 0.3, 0.6 and 0.9; (b) viscosity parameter $\bar{\lambda} = 0$, 0.003, 0.005 and 0.01; (c) temperature ratios $\beta_T = 2/3$, 7/8, 1 and 3/2; (d) turbulent intensities $q_c = 0$, 0.5, 0.8 and 1. In (a,b), the upper four curves represent the results for $\hat{\delta} = 0$ (parallel-flow assumption), and the lower four curved represent the results for $\hat{\delta} = 0.06$ (non-parallelism included).

Viscous effects are characterised by Re or equivalently $\bar{\lambda}$ (see (3.4)). As shown in figure 3(b), with non-parallelism being accounted for, increase of $\bar{\lambda}$ (i.e. viscosity) has the effect of decreasing the amplitude and suppressing its oscillations, namely, viscosity plays a stabilising role. However, if non-parallelism is ignored, i.e. $\hat{\delta} = 0$, viscosity plays a destabilising role, as it does in the incompressible regime (Goldstein & Hultgren 1988; Wu & Zhuang 2016).

The temperature ratio β_T is an important parameter characterising the mean flow. Figure 3(c) shows that deviation of β_T away from 1, i.e. the difference of the free-stream temperatures, enhances the oscillation of the amplitude.

The parameter q_c characterises the turbulence intensity, which influences the velocity profile. The amplitude evolution for different q_c is displayed in figure 3(d). The qualitative behaviours remain similar, but appreciable quantitative differences exist. For higher q_c, the amplitude is smaller.

Calculations were also performed for different phase lags $\hat{\theta}_1$ and $\hat{\theta}_2$. Neither is found to have any significant influence, and so the results are not presented.

https://doi.org/10.1017/jfm.2019.909 Published online by Cambridge University Press

6.3.2. *Vorticity and temperature roll-up, and development of harmonics*

The nonlinear dynamics of CS can be illustrated by the temperature and vorticity fields in the critical layer. The total temperature in the critical layer is

$$T_{total,c} = T_{\langle 0\rangle} + \epsilon^{1/2} T_{\langle 1/2\rangle} + \epsilon T_{\langle 1\rangle} + \cdots . \tag{6.38}$$

Recalling (3.13) and (3.60), we have $T_{\langle 0\rangle} = \bar{T}_c$, $T_{\langle 1/2\rangle} = \bar{T}_{1,c}\bar{x}$ and

$$\begin{aligned} T_{\langle 1\rangle} \;=\; & \frac{1}{2}\bar{T}_c'' Y^2 + \bar{T}_{1,c}'\bar{x}Y + \frac{1}{2}\bar{T}_{2,c}\bar{x}^2 + \bar{T}_{cM}' Y \\ & + T^\dagger + \left[\frac{\bar{T}_c''}{\bar{U}_c'} + (\gamma-1)Ma^2\bar{U}_c'\right] A^\dagger \mathrm{e}^{\mathrm{i}\alpha\zeta} + \text{c.c.} \end{aligned} \tag{6.39}$$

Similarly, the total vorticity in the critical layer is

$$\Omega_{total,c} = \frac{\partial V_{total,c}}{\partial x} - \frac{\partial U_{total,c}}{\partial y} = -\Omega_{\langle 0\rangle} - \epsilon^{1/2}\Omega_{\langle 1/2\rangle} - \epsilon\Omega_{\langle 1\rangle} - \cdots , \tag{6.40}$$

with $V_{total,c} = \epsilon\bar{V}_c + \epsilon\tilde{v}_0 + \epsilon^{3/2}\tilde{v}_1$ and

$$\begin{aligned} U_{total,c} \;=\; & \bar{U}_c + \epsilon^{1/2}(\bar{U}_c' Y + \bar{U}_{1,c}\bar{x}) + \epsilon\left(\bar{U}_{1,c}'\bar{x}Y + \frac{\bar{U}_{2,c}}{2}\bar{x}^2 + \tilde{u}_0\right) \\ & + \epsilon^{3/2}\left(\frac{\bar{U}_c'''}{6}Y^3 + \frac{\bar{U}_{1,c}''}{2}\bar{x}Y^2 + \frac{\bar{U}_{2,c}'}{2}\bar{x}^2 Y + \frac{\bar{U}_{3,c}}{6}\bar{x}^3 + \frac{\bar{U}_{cM}''}{2}Y^2 + \tilde{u}_1\right). \end{aligned} \tag{6.41}$$

Making use of (3.55*a*), (3.56) and (3.65), we have $\Omega_{\langle 0\rangle} = \bar{U}_c'$, $\Omega_{\langle 1/2\rangle} = \bar{U}_{1,c}'\bar{x}$ and

$$\begin{aligned} \Omega_{\langle 1\rangle} \;=\; & \frac{\bar{U}_c'''}{2}Y^2 + \bar{U}_{1,c}''\bar{x}Y + \frac{\bar{U}_{2,c}'}{2}\bar{x}^2 + \bar{U}_{cM}'' Y \\ & + Q^\dagger + \left(\frac{\bar{U}_c'''}{\bar{U}_c'} - \frac{\bar{T}_c''}{\bar{T}_c} + \frac{Ma^2\bar{U}_c'^2}{\bar{T}_c}\right) A^\dagger \mathrm{e}^{\mathrm{i}\alpha\zeta} + \text{c.c.} \end{aligned} \tag{6.42}$$

Noting the re-scaling (4.1) and expansions (4.15), we can write the (renormalised) total temperature and vorticity in the critical layer as $(\bar{T}_c + \epsilon^{1/2}\bar{T}_{1,c}\bar{x} + \epsilon\bar{T}_\chi + \epsilon T_c)$ and $(-\bar{U}_c' - \epsilon^{1/2}\bar{U}_{1,c}'\bar{x} - \epsilon\bar{U}_\chi - \epsilon p_Q\Omega_c)$ respectively, where $\bar{T}_\chi$ and $\bar{U}_\chi$ denote the terms independent of η. The temperature and vorticity variations are represented by T_c and Ω_c,

$$\begin{aligned} T_c(\tau,\bar{x},\eta,\bar{\zeta}) \;=\; & \frac{\bar{T}_c'''}{2\alpha^2\bar{U}_c'^2}(\eta+S_0)^2 + \left(\frac{\bar{T}_{cM}'}{\alpha\bar{U}_c'} + \chi_1\bar{x}\right)(\eta+S_0) + \sum_{n=-\infty}^{\infty} T_n(\tau,\bar{x},\eta)\mathrm{e}^{\mathrm{i}n(\bar{\zeta}-S_0\tau)} \\ & + \left\{\left[\frac{\bar{T}_c''}{\bar{U}_c'} + (\gamma-1)Ma^2\bar{U}_c'\right]\frac{A(\bar{x})}{\alpha^2\bar{U}_c'}\mathrm{e}^{\mathrm{i}(\bar{\zeta}-S_0\tau)} + \text{c.c.}\right\}, \end{aligned} \tag{6.43}$$

https://doi.org/10.1017/jfm.2019.909 Published online by Cambridge University Press

$$\Omega_c(\tau,\bar{x},\eta,\bar{\zeta}) = \frac{\bar{U}_c'''}{2\alpha^2\bar{U}_c'^2 p_Q}(\eta+S_0)^2 + \left(\frac{\bar{U}_{cM}''}{\alpha\bar{U}_c' p_Q} + \frac{\bar{U}_c'\bar{U}_{1,c}'' - \bar{U}_{1,c}\bar{U}_c'''}{\alpha\bar{U}_c'^2 p_Q}\bar{x}\right)(\eta+S_0) + \sum_{n=-\infty}^{\infty} Q_n(\tau,\bar{x},\eta)\mathrm{e}^{\mathrm{i}n(\bar{\zeta}-S_0\tau)} + \left[\left(\frac{\bar{U}_c'''}{\bar{U}_c'} - \frac{\bar{T}_c''}{\bar{T}_c} + \frac{Ma^2\bar{U}_c'^2}{\bar{T}_c}\right)\frac{A(\bar{x})}{\alpha^2\bar{U}_c' p_Q}\mathrm{e}^{\mathrm{i}(\bar{\zeta}-S_0\tau)} + \mathrm{c.c.}\right]. \tag{6.44}$$

These quantities will be plotted.

Physically, roll-up is associated with the simultaneous appearance of high harmonics, which are generated by nonlinear interactions. The harmonics in the main shear layer arise due to the forcing through the streamwise velocity jumps ($\hat{u}_1^{\langle n\rangle+} - \hat{u}_1^{\langle n\rangle-}$). According to the asymptotic analysis,

$$\hat{u}_1^{\langle n\rangle+} - \hat{u}_1^{\langle n\rangle-} = \frac{n\alpha}{2\pi}\int_{-\infty}^{\infty}\int_{0}^{2\pi/n\alpha} Q^{\dagger}\mathrm{e}^{-\mathrm{i}n\alpha\zeta}\,\mathrm{d}\zeta\,\mathrm{d}Y, \tag{6.45}$$

and hence we take

$$H_n = \int_{-\infty}^{\infty} Q_n\,\mathrm{d}\eta \tag{6.46}$$

as a measure of harmonics.

Figure 4 shows the renormalised critical-layer temperature and vorticity contours at four different streamwise locations $\bar{x}=0$, 1, 2 and 6, as well as the profiles of the mean-flow distortion (Q_0), the fundamental component (Q_1) and the first harmonic (Q_2). At $\bar{x}=0$, the temperature and vorticity contours exhibit rather simple patterns. The fundamental component Q_1 has the largest magnitude. As $\bar{x}$ increases, Q_0 and Q_2 are excited and amplify gradually, and the first harmonic Q_2 is smaller than the mean-flow distortion Q_0. At $\bar{x}=1$, Q_0 becomes almost comparable with Q_1, and the contours start to roll up with a roller structure taking its shape. After this point, the mean-flow distortion, the fundamental component and the first harmonic continue to grow, and they have all reached nearly the same level at $\bar{x}=2$, where the contours of the temperature and vorticity have fully rolled up, and a complete CS appears. At this position, the peak of Q_0 is greater than that of Q_1, whilst Q_2 also increases to a considerable level here. Between $\bar{x}=2$ and 6, the CS maintains its overall appearance and some fine-scale features emerge: rapid variations occur near the top and bottom of the roller. At $\bar{x}=6$, the rollers become tilted towards the streamwise direction, the braid region between the neighbouring eddies becomes diffused. Here, the mean-flow distortion maintains both its magnitude and distribution characteristics at the previous positions, but the fundamental component and the first harmonic decay gradually.

Figure 5 shows the streamwise development of the first five harmonics which are measured by $H_n(n=2\sim 6)$ as defined by (6.46). The harmonics are excited simultaneously after the neutral position. For $\bar{x}\geqslant 2$, the first five harmonics have more or less the same magnitude. They are responsible for the roll-up and other nonlinear phenomena of CS.

Further numerical results indicate that roll-up of CS is a robust phenomenon, exhibiting similar characteristics in various conditions. This is illustrated for four cases. Besides the case $\mathcal{F}$, $\mathcal{F}-\bar{\lambda}$, $\mathcal{F}-\hat{\delta}$ and $\mathcal{F}-Ma$ represent the cases of high

https://doi.org/10.1017/jfm.2019.909 Published online by Cambridge University Press

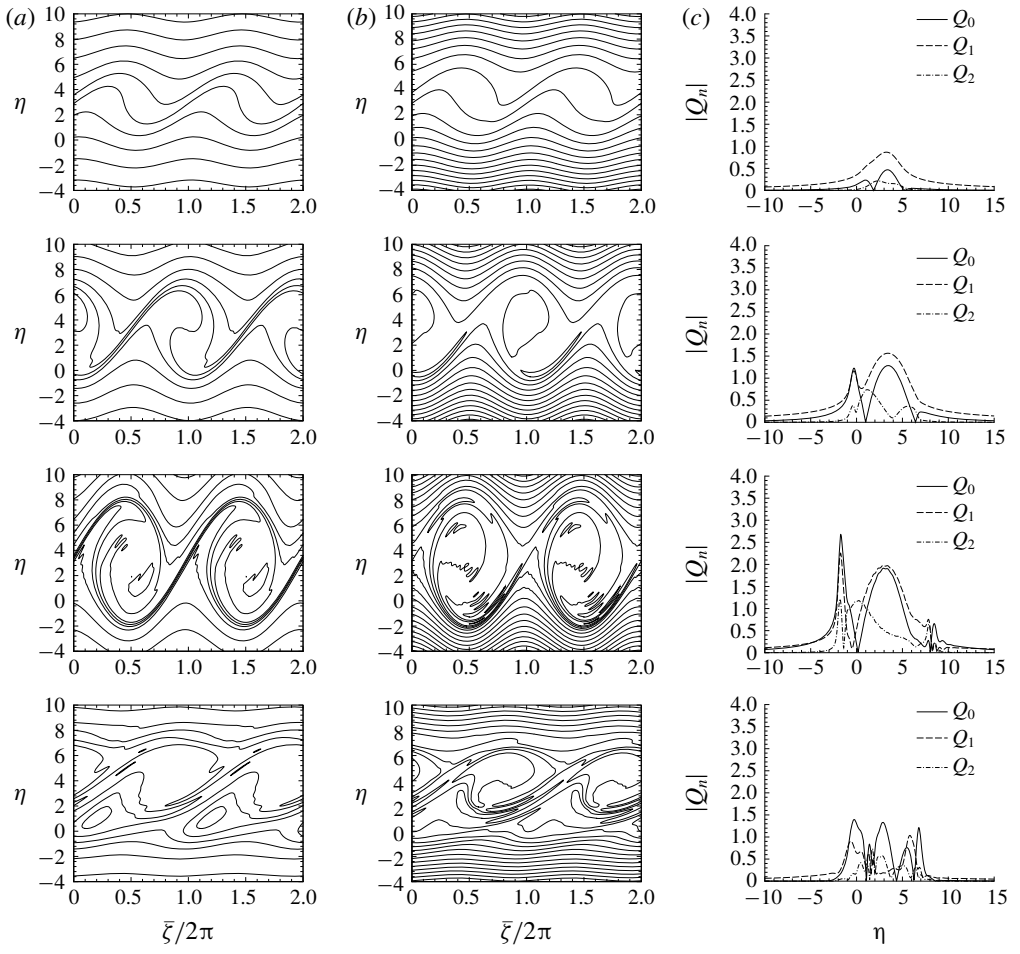

FIGURE 4. The (*a*) temperature and (*b*) vorticity contours of CS, and (*c*) the profiles of the harmonics at different streamwise positions: $\bar{x}=0$ (the first row), 1 (the second row), 2 (the third row) and 6 (the fourth row) in case $\mathcal{F}$.

viscosity ($\bar{\lambda}=0.01$), strong non-parallelism ($\hat{\delta}=0.12$), and moderate compressibility ($Ma_1=0.6$) respectively. In order to make a clear comparison, the same coordinate scale for the harmonic distributions and the same contour levels are selected in all cases. The (renormalised) critical-layer temperature and vorticity contours as well as the harmonic distributions at $\bar{x}=3$ are displayed in figure 6. The structures appear broadly similar. The high viscosity (the second row) and stronger non-parallelism (the third row) cases show less small-scale oscillations of the harmonics, and the contours look smooth, which is expected since viscosity and non-parallelism tend to play a stabilising and smoothing role. The moderately increased compressibility (the fourth row) does not change the temperature and vorticity fields appreciably. At this location $\bar{x}=3$, the temperature and vorticity fluctuations persist, and the roll-up intensifies, exhibiting more prominent small-scale features than at upstream locations.

https://doi.org/10.1017/jfm.2019.909 Published online by Cambridge University Press

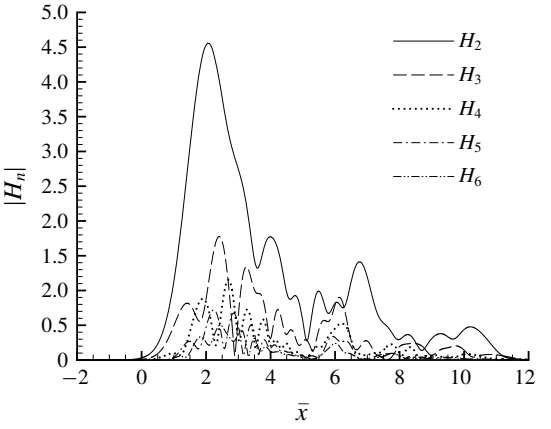

FIGURE 5. The development of the higher-order harmonics ($n = 2, 3, 4, 5, 6$).

6.4. *Numerical results for coherent structures with discrete-sideband modes*

A CS may be better represented by a wavetrain consisting of multi-frequencies. A simple case is a wavetrain comprised of a central mode with frequency ω_0 and one or two sideband modes $\omega_0 \pm \omega_\nu$ with $\omega_\nu \ll 1$. The nonlinear evolution of such a wavetrain is now investigated. The phenomena of the excitation and interaction of higher-order sidebands will be described.

In order to analyse the spectrum of the flow field, it is convenient to introduce the double-Fourier components $\widetilde{u}_n^{(m)}(\bar{x}, \eta)$ with respect to both $\bar{\zeta}$ and τ of the inner solution for velocity $\tilde{u}$,

$$\tilde{u}(\tau, \bar{x}, \eta, \bar{\zeta}) = \sum_{n=-\infty}^{\infty} \sum_{m=-\infty}^{\infty} \widetilde{u}_n^{(m)}(\bar{x}, \eta) \mathrm{e}^{\mathrm{i}n(\bar{\zeta} - S_0\tau) - \mathrm{i}m\Delta\tau} + \text{c.c.}, \tag{6.47}$$

whose exponent could be also written as $[\mathrm{i}n\alpha x - \mathrm{i}(n\alpha c + \epsilon^{1/2} n S_0 + \epsilon^{1/2} m\Delta)t]$. Obviously, $\widetilde{u}_n^{(m)}(\bar{x}, \eta)$ represents the strength of the component with frequency $[n\omega_0 + m\omega_\nu]$.

Using the outer and inner solutions, (3.15) and (3.53), as well as the relationship between $\tilde{u}$ and Q, (3.65), we can construct a composite solution for $\tilde{u}_n^{(m)}$ accurate up to and including $O(\epsilon^{3/2})$. The nonlinearly generated mean-flow distortion ($n = 0$) and harmonics are found as

$$\widetilde{u}_0^{(m)}(\bar{x}, \eta) = \epsilon^{3/2} \frac{p_Q}{\alpha \bar{U}_c'} \int_{-\infty}^{\eta} Q_0^{(m)}(\bar{x}, \eta^\star)\, \mathrm{d}\eta^\star, \tag{6.48}$$

$$\widetilde{u}_n^{(m)}(\bar{x}, \eta) = \epsilon^{3/2} \left[\frac{p_Q}{\alpha \bar{U}_c'} \int_{-\infty}^{\eta} Q_n^{(m)}\, \mathrm{d}\eta^\star + \hat{u}_1^{\langle n\rangle -} \Big|^{(m)} \right] \quad (n = 2, 3, \ldots), \tag{6.49}$$

where the superscript (m) for $\hat{u}_1^{\langle n\rangle -}$ indicates the mth-order sideband of the $(n-1)$th harmonic in the outer solution (3.15). The fundamental component ($n = 1$) is derived from (3.56) and (3.65). Considering the integration domain $(-\tilde{H}, \tilde{H})$ defined previously, we have

https://doi.org/10.1017/jfm.2019.909 Published online by Cambridge University Press

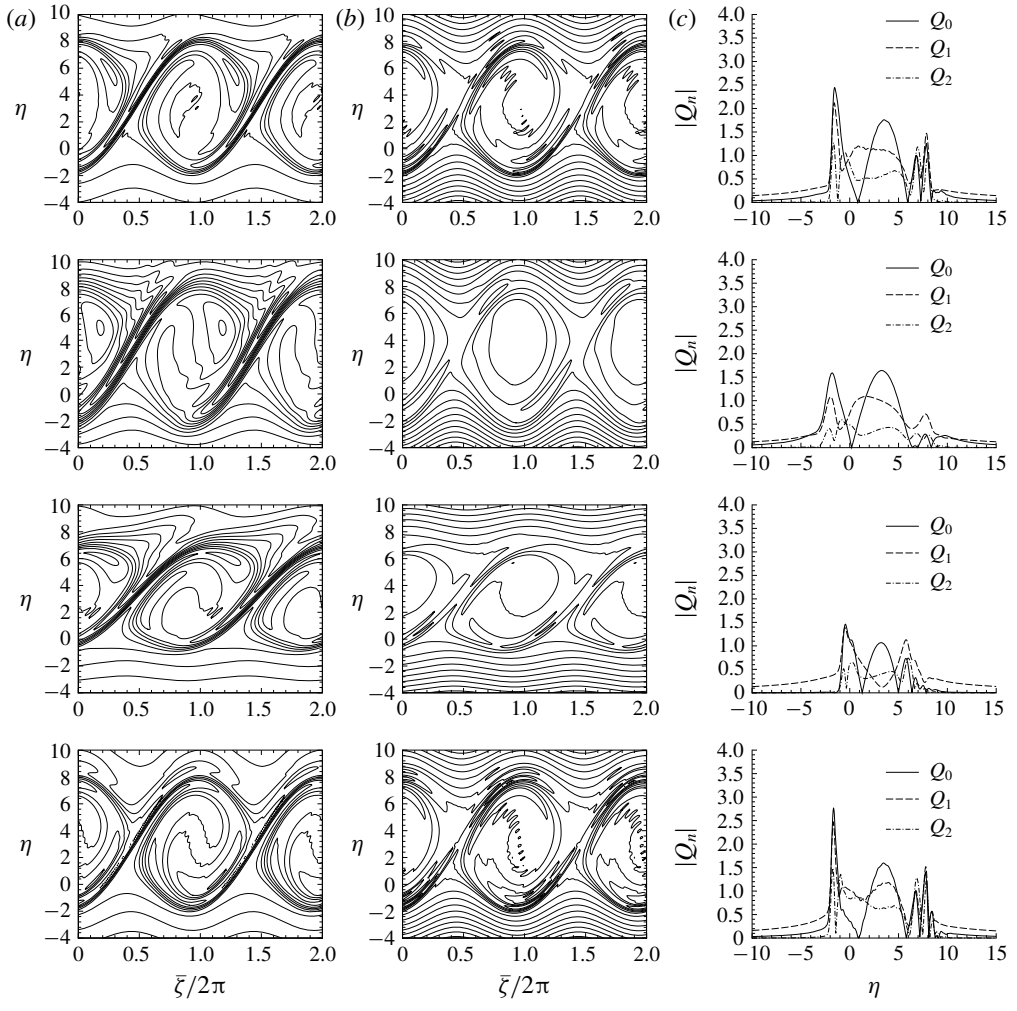

FIGURE 6. The (*a*) temperature and (*b*) vorticity contours of CS, and (*c*) the profiles of the harmonics in different cases: $\mathcal{F}$ (the first row), $\mathcal{F}-\bar{\lambda}$ (the second row), $\mathcal{F}-\hat{\delta}$ (the third row) and $\mathcal{F}-Ma$ (the fourth row) at the streamwise position $\bar{x}=3$.

$$\begin{aligned}\widetilde{u}_1^{(m)}(\bar{x},\eta) \;=\; & -\frac{\epsilon b_1}{\alpha^2\bar{U}_c'}A^{(m)}+\epsilon^{3/2}\frac{p_Q}{\alpha\bar{U}_c'}\left[\left(\mathrm{i}\frac{\partial}{\partial\bar{x}}+m\Delta+S_0+\chi_2\bar{x}\right)A^{(m)}\ln\frac{\epsilon^{1/2}}{\alpha\bar{U}_c'}\right]\\ & +\epsilon^{3/2}\frac{p_Q}{\alpha\bar{U}_c'}\lim_{\tilde{H}\to\infty}\left[\left(\mathrm{i}\frac{\partial}{\partial\bar{x}}+m\Delta+S_0+\chi_2\bar{x}\right)A^{(m)}\ln|\tilde{H}|+\int_{-\tilde{H}}^{\eta}Q_1^{(m)}\,\mathrm{d}\eta^{\star}\right]\\ & +\epsilon^{3/2}\left[\left(\alpha^2+\frac{\bar{U}_c'''}{\bar{U}_c'}-\frac{\bar{T}_c''}{\bar{T}_c}+\frac{Ma^2\bar{U}_c'^2}{\bar{T}_c}\right)\frac{(\eta+S_0)}{\alpha^2\bar{U}_c'}A^{(m)}+\hat{u}_1^{\langle 1\rangle-}\Big|^{(m)}\right]. \qquad (6.50)\end{aligned}$$

Furthermore, in order to show the temporal modulation, we will monitor the central velocity $\tilde{u}_c(t,\bar{x})=\tilde{u}(\tau,\bar{x},0,\bar{\zeta})$, as well as the modulus function $a(t,\bar{x})$ and phase

https://doi.org/10.1017/jfm.2019.909 Published online by Cambridge University Press

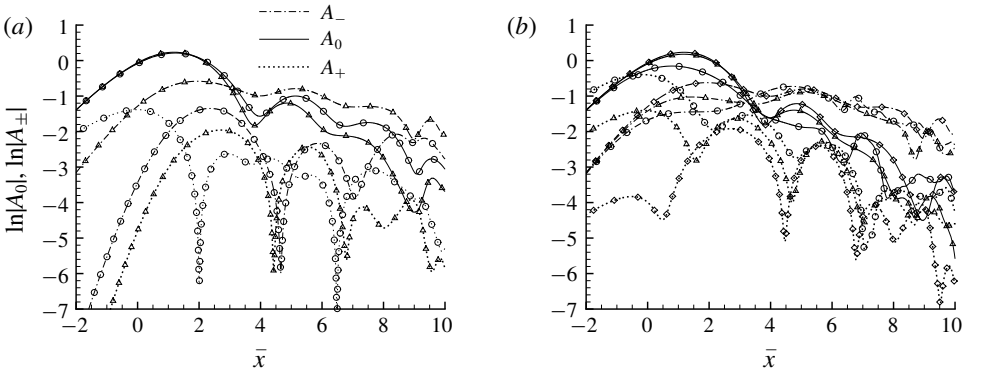

FIGURE 7. The evolution of CS consisting of sideband components. (*a*) Cases where only the lower sideband is seeded ($a_0^+ = 0$, triangles) or the upper sideband is seeded ($a_0^- = 0$, circles). (*b*) Effects of the initial amplitude ratio $a_0^+/a_0^- = 0.3$ (diamonds), 1.0 (triangles) and 3.0 (circles).

function $\psi(t, \bar{x})$ of the complex amplitude function,

$$\widetilde{A}(\tau, \bar{x}) = \sum_{m=-\infty}^{\infty} A^{(m)}(\bar{x}) \mathrm{e}^{-\mathrm{i}m\Delta\tau - \mathrm{i}S_0\tau} \overset{\text{def.}}{=\!=} a(t, \bar{x}) \mathrm{e}^{\mathrm{i}2\pi\psi(t,\bar{x})}. \tag{6.51}$$

6.4.1. *The amplitude evolution of sideband perturbations*

As an example, calculations are performed for case $\mathcal{H}$', which is the case $\mathcal{F}$ with the added sideband components with phases $\varphi_0^- = -\pi/3$ and $\varphi_0^+ = \pi/6$; see (4.29). We take $\Delta = |S_0|/2$ with S_0 being substituted by $\epsilon^{-1/2}\alpha c/6$. The amplitudes of the central, upper- and lower-sideband modes will be represented by A_0, A_+ and A_-, which correspond to $A^{(0)}$, $A^{(+1)}$ and $A^{(-1)}$ in the expansion (4.25), respectively.

In order to investigate excitation of discrete-sideband modes, calculations were preformed first for the extreme cases where the initial amplitude of one of the two sideband components was set to zero. As figure 7(*a*) shows, the development of the dominate central mode is not significantly influenced by the sideband modes. The unseeded sideband mode in either case is soon excited and reaches a comparable level. In the early stage of the development, the growth rate of one sideband exceeds its linear growth rate due to the nonlinear interactions. Furthermore, after the excitation and transient adjustment, the upper and lower sidebands both undergo similar nonlinear attenuation, as the central mode does. The lower sideband amplitude is higher than those of the central and upper modes, i.e. the lower-frequency component eventually becomes dominant. Figure 7(*b*) shows the development of sideband modes for three representative ratios $a_0^+/a_0^- = 0.3$, 1 and 3. The initial ratio of the sideband amplitudes causes significant differences in the early and intermediate stages. The overall feature of the later stage for these conventional ratios is the similar to the extreme cases: after the rapid excitation, the amplitude of the lower sideband is always higher than those of the upper sideband and the central mode. The emergence and development of the lower sideband is a phenomenon of energy back scattering. Although not shown here, the same occurs in various cases with different initial phases $\varphi_0^{\pm}$, $\bar{\lambda}$, $\hat{\delta}$ and so on.

https://doi.org/10.1017/jfm.2019.909 Published online by Cambridge University Press

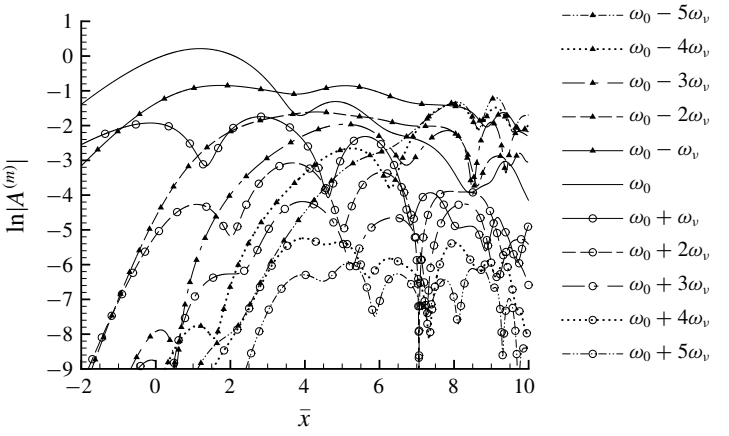

FIGURE 8. The development of $A^{(m)}$, the amplitudes of the harmonics with frequencies $\omega_0 \pm m\omega_v$ $(m = 0, 1, \ldots, 5)$ in case $\mathcal{H}$.

6.4.2. *Spectral evolution and broadening*

Figure 8 shows the evolution of the fundamental and its sideband components. The first-order upper and lower sidebands ($m = \pm 1$) interact the central mode to suppress/enhance the upper/lower sideband. The amplitude of the latter exceeds eventually that of the central mode and becomes the dominant part of the disturbance. At the same time, the second- and higher-order sideband components ($m = \pm 2, \pm 3, \ldots$) are excited. At each order, the upper sidebands are initially stronger than the lower ones, but the latter have higher growth rates and hence rise rapidly to reach considerable magnitudes, which is also a manifestation of energy back scattering. As a result, the spectrum of the perturbation broadens gradually around ω_0.

As with the evolution of CS with a single frequency, higher harmonics here are simultaneously excited due to the strong nonlinearity, and grow in turn. Figure 9 shows the evolution of the first harmonic ($n = 2$) together with its sideband components. The evolution feature is similar to that of the fundamental frequency component (see figure 8): the central mode has a relatively large amplitude in the initial stage, and then attenuates to lose its dominant status as the sidebands develop, with the lower sidebands increasing more rapidly from lower initial amplitudes. Higher harmonics, as well as their sidebands, develop similarly and the spectrum broadens around them.

Moreover, the mean-flow distortion ($\omega = 0$) and near-zero-frequency components are generated as is shown in figure 10. Unlike harmonics, these components have larger amplitudes and attenuate very slowly. This theoretical conclusion is consistent with experimental observations (cf. Miksad 1973). As will be shown in § 5, it is these components that emit sound. Note that their amplification and attenuation are not monotonic, but display a series of jitterings, a feature that may enhance acoustic radiation. The spectrum of the perturbation at three streamwise positions $\bar{x} = 0, 2, 5$ is shown in figure 11. As stated before, the component $\widetilde{u}_0^{(0)}$ attenuates slowly, and is thus used to re-scale the amplitudes of the others. In order to display the results clearly, the spectrum curves at $\bar{x} = 2$ and 5 are moved four and eight units down in the vertical direction respectively. Several features are worth emphasising: due to the strong nonlinearity, all harmonics ($n\omega_0$, $n = 2, 3, \ldots$) are excited at the same order

https://doi.org/10.1017/jfm.2019.909 Published online by Cambridge University Press

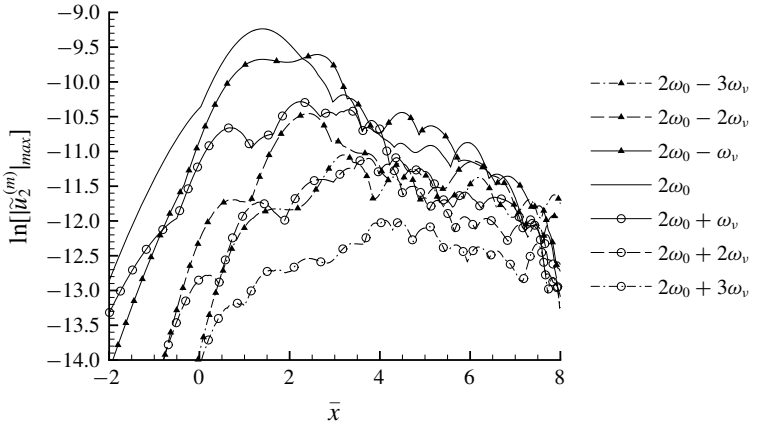

FIGURE 9. The development of the maximum streamwise velocity of the first-order harmonic as well as its sideband components ($\widetilde{u}_2^{(m)}$, $m = 0, \pm1, \pm2, \pm3$) in case $\mathcal{H}$.

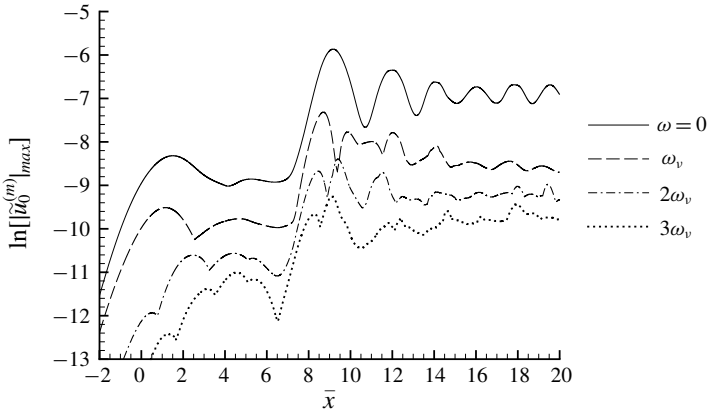

FIGURE 10. The development of the maximum streamwise velocity $\widetilde{u}_0^{(m)}$, representing the mean-flow distortion and its sidebands (at the frequencies $m\omega_v$, $m = 0, 1, 2, 3$), in case $\mathcal{H}$.

and the energy is transferred to the higher-frequency components; the mean-flow distortion and the main difference frequency mode ω_v may attain amplitudes larger than those of the seeded modes; the sidebands ($n\omega_0 \pm m\omega_v$) between harmonics are gradually filled up, leading to spectral broadening.

6.4.3. *Amplitude-phase modulation in case* $\mathcal{H}$

A wavetrain consisting of two harmonic components with frequencies ω_1 and ω_2, which differ by a small amount ($|\omega_0 - \omega_1| \ll 1$), exhibits the behaviour known as 'amplitude-phase modulation': the time trace varies rapidly with a high frequency $(\omega_0 + \omega_1)/2 \approx \omega_0$ but its amplitude and phase change slowly on the longer time scale $2\pi/\omega_v$, where $\omega_v = |\omega_0 - \omega_1|$. It is the components with frequencies $m\omega_v$ ($m = 1, 2, \ldots$) that constitute the unsteady mean flow and play the role of sound source as we will show later. Here, we focus on the slow temporal modulation.

https://doi.org/10.1017/jfm.2019.909 Published online by Cambridge University Press

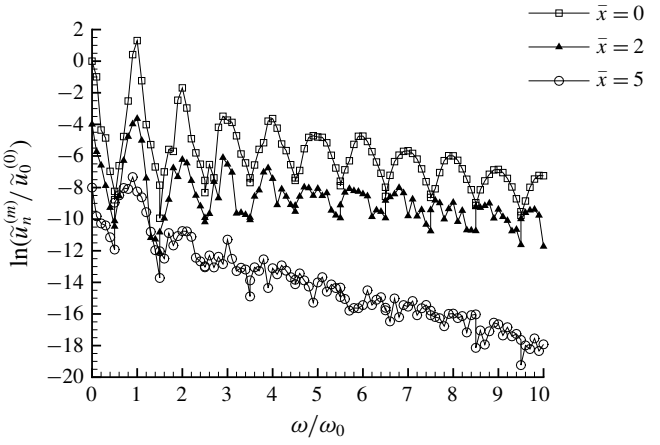

FIGURE 11. The spectrum of the streamwise velocity at positions $\bar{x}=0,\,2,\,5$ in case $\mathcal{H}$ with curves moved four (for $\bar{x}=2$) and eight (for $\bar{x}=5$) units down.

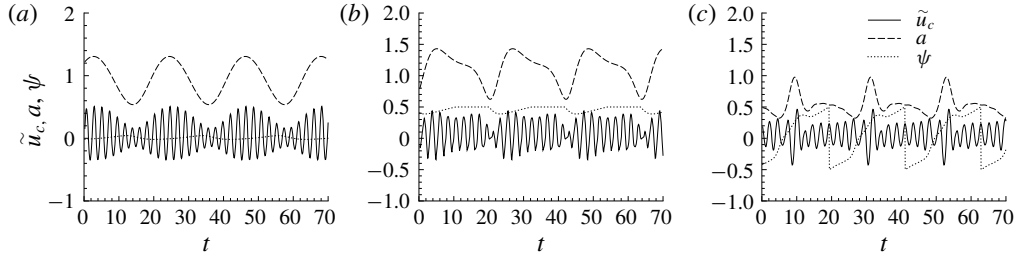

FIGURE 12. The amplitude-phase modulation at three streamwise positions (*a*) $\bar{x}=0$, (*b*) $\bar{x}=2$ and (*c*) $\bar{x}=5$ in case $\mathcal{H}$.

Figure 12 shows the time trace of $\tilde{u}_c$, the velocity at the critical level, which features a sequence of wavetrains or wavepackets at $\bar{x}=0$ and 2. The envelope modulates the slow time scale of $2\pi/\omega_v$, and as do the modulus a and phase ψ of the complex amplitude $\tilde{A}(\tau,\,\bar{x})$. This is a typical amplitude-phase modulation phenomenon. Downstream of $\bar{x}=2$, $\tilde{u}_c$ is still modulated on the slow time variable, while the modulus and phase of the wavepacket envelope become less regular and exhibit a relaxation type of oscillation. At $\bar{x}=5$, the wavepacket envelope jitters rather violently, and both a and ψ oscillate rapidly. As a result, the time series appears more irregular.

Figure 13 displays the profiles of the first harmonic $\widetilde{u}_2^{(0)}$ and its sidebands $\widetilde{u}_2^{(m)}$ ($m=\pm1,\,\pm2,\,\pm3$), as well as the profiles of the mean-flow distortion $\widetilde{u}_0^{(0)}$ and the low-frequency sidebands $\widetilde{u}_0^{(m)}$ ($m=1,\,2,\,3$). The lower sideband $\widetilde{u}_2^{(-1)}$ is always stronger than the upper one $\widetilde{u}_2^{(1)}$. At $\bar{x}=0$, the sidebands are all weaker than their own central components. At $\bar{x}=2$, the harmonics and their sidebands increase rapidly. The component $\widetilde{u}_0^{(1)}$ rises to a considerable level, which distorts the envelop as figure 12 shows. At $\bar{x}=5$, the harmonics and their sidebands have attenuated considerably, but the mean-flow distortion and its sidebands $\widetilde{u}_0^{(m)}$ retain significant magnitudes. These behaviours are consistent with those shown in figure 10.

https://doi.org/10.1017/jfm.2019.909 Published online by Cambridge University Press

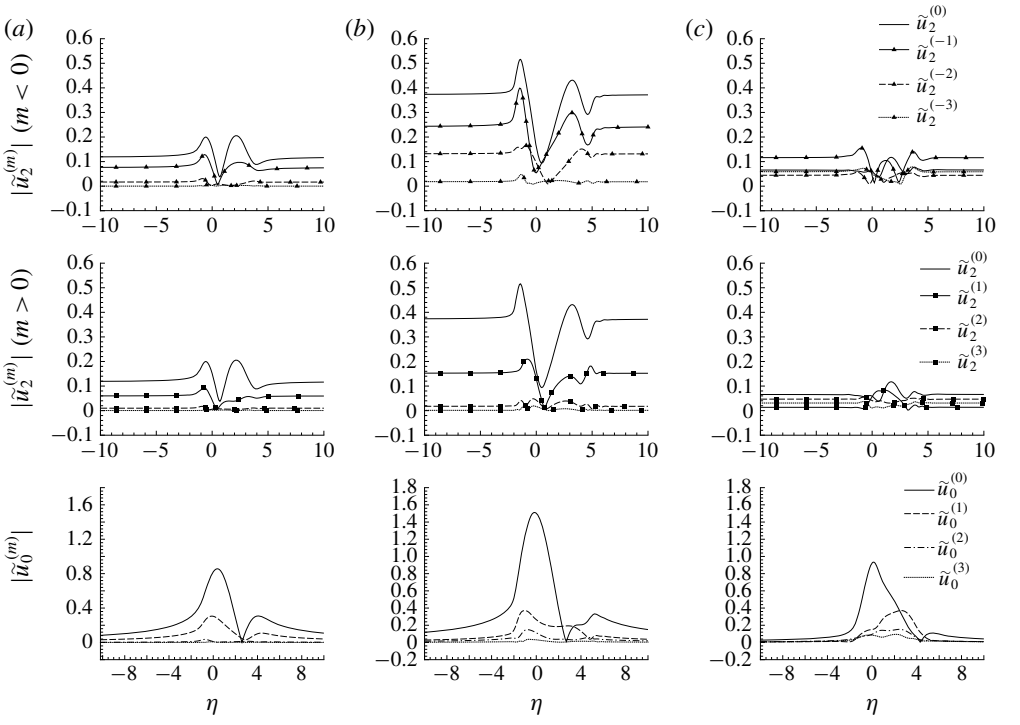

FIGURE 13. The profiles of the first harmonic $\widetilde{u}_2^{(0)}$ and its sidebands $\widetilde{u}_2^{(m)}$ $(m=\pm1, \pm2, \pm3)$ as well as the mean-flow distortion $\widetilde{u}_0^{(0)}$ and the low-frequency sidebands $\widetilde{u}_0^{(m)}$ $(m=1, 2, 3)$ at three streamwise positions (*a*) $\bar{x}=0$, (*b*) $\bar{x}=2$ and (*c*) $\bar{x}=5$ in case $\mathcal{H}$.

The critical-layer temperature and vorticity of a CS are modulated periodically over the long period $T=2\pi/\omega_v$. This is illustrated in figure 14, which displays the temperature and vorticity contours at $\bar{x}=3$ and at instants $\tau=T/6$, $T/2$ and $5T/6$. A CS at a fixed location changes its shape and intensity appreciably with time.

It is interesting to note that, due to the combined effects of temporal modulation and nonlinearity, the signature of CS is rather intermittent (figure 12). The fundamental and sideband components in a wavepacket contain supersonic Fourier components, whose amplitudes are exponentially small with respect to the ratio of the modulation length scale to the acoustic wavelength (Tam & Morris 1980; Crighton & Huerre 1990). Such components, each radiating a sound wave, are rather weak for a mildly modulated wavepacket, which is the case if nonlinearity is neglected. However, owing to the oscillatory nonlinear attenuation as shown in figure 8, their magnitudes could be considerable in practice, and accordingly the radiated low-angle sound waves may be significant (cf. Cavalieri *et al.* 2011; Cavalieri & Agarwal 2014). It would be of interest to assess this linear radiation mechanism for the developing wavepackets with the predicted jittering. However, our focus in this paper is on the nonlinear radiation mechanism associated with the sidebands close to zero frequency, the oscillatory attenuation of which, shown in figure 10, implies strong radiation of low-frequency sound waves.

https://doi.org/10.1017/jfm.2019.909 Published online by Cambridge University Press

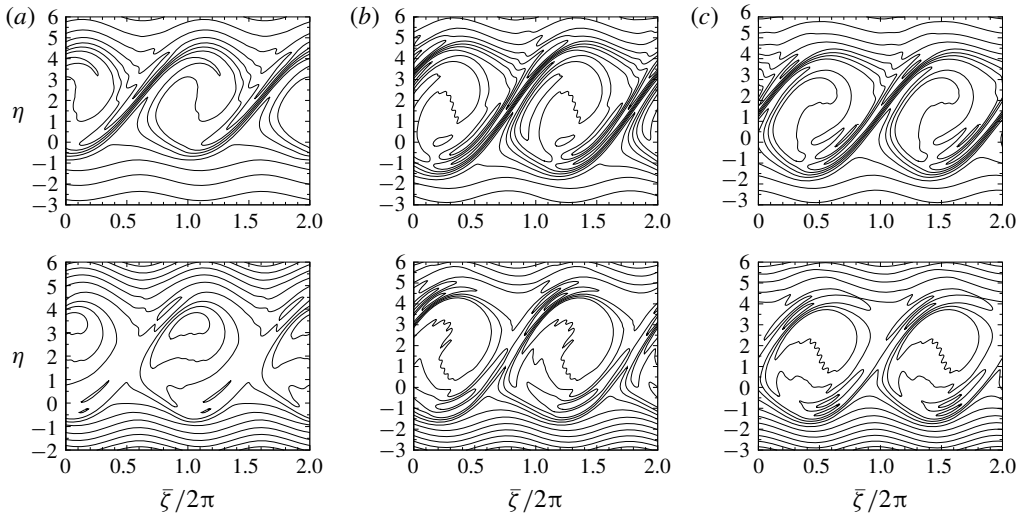

FIGURE 14. Temporal modulation of the temperature (the first row) and vorticity (the second row) of the CS consisting of sidebands at $\bar{x} = 3$: contours at different instants (*a*) $\tau = T/6$, (*b*) $\tau = T/2$ and (*c*) $\tau = 5T/6$ in a period in case $\mathcal{H}$.

6.5. *Numerical results of acoustic radiation by CS*

As was shown in § 5, a CS in the form of a wavepacket interacts nonlinearly to provide a mean-flow distortion that varies slowly in time and space. The modulated mean-flow distortion would lead an $O(\epsilon^{5/2})$ pressure and vertical velocity perturbation at the outer edges of the main shear layer, and thus emits low-frequency sound to the far fields. Here we examine the directivity and spectrum of the sound field.

In our calculations, we first find the Fourier transforms of the physical sources $\mathcal{S}(\tau, \bar{x}, y)$, $\mathcal{U}(\tau, \bar{x})$ and $\mathcal{Y}(\tau, \bar{x})$

$$\widehat{\mathcal{S}}(\omega, \kappa, y) = \frac{\widehat{\bar{B}}_0}{\alpha^4 \bar{U}_c'^2}\left[\frac{\kappa^2}{c^2}\left(\frac{2\bar{T}'}{\alpha^2}J_{y1}^{\pm} + \tilde{\mathcal{S}}_1\right) - (\omega-\kappa)^2\left(-\frac{2Ma^2\bar{U}'}{\alpha^2}J_{y2}^{\pm} + \tilde{\mathcal{S}}_2\right) + \frac{(\omega-\kappa)\kappa}{c}\left(\frac{2Ma^2\bar{U}'}{\alpha^2}J_{y1}^{\pm} - \frac{2\bar{T}'}{\alpha^2}J_{y2}^{\pm} + \tilde{\mathcal{S}}_3\right)\right], \tag{6.52}$$

$$\widehat{\mathcal{U}}(\omega, \kappa) = \frac{p_Q}{\alpha^2 \bar{U}_c'^2}\left[\mathrm{i}p_3(\omega-\kappa)\int_{-\infty}^{\infty}\eta\widehat{\bar{T}}_0\,\mathrm{d}\eta - (\Lambda_1\omega - \Lambda_2\kappa)\widehat{\bar{B}}_0\right], \tag{6.53}$$

$$\widehat{\mathcal{Y}}(\omega, \kappa) = \frac{\mathrm{i}}{\alpha^4 \bar{U}_c'^2}\left[(\widehat{\bar{B}}_1 - \widehat{\bar{B}}_1^*)\tilde{\mathcal{Y}}_1 + (\widehat{\bar{B}}_2 - \widehat{\bar{B}}_2^*)\tilde{\mathcal{Y}}_2 + \frac{\partial\widehat{\bar{B}}_0}{\partial\kappa}\tilde{\mathcal{Y}}_0\right], \tag{6.54}$$

where $\widehat{\bar{B}}_j$ denotes the Fourier transform of $B_j \equiv \alpha^4 \bar{U}_c'^2 B_j^{\dagger}$ and $\widehat{\bar{B}}_j^*(\omega, \kappa) = \widehat{\bar{B}}_j^{\,*}(-\omega, -\kappa)$ $(j = 0, 1, 2)$ with $B_j^{\dagger}$ being defined in (5.8*a*) and (5.17).

In the discrete-sideband case, B_j can be written as a Fourier series,

$$B_j(\tau, \bar{x}) = \sum_{m=-\infty}^{\infty} B_j^{(m)}(\bar{x})\mathrm{e}^{-\mathrm{i}m\Delta\tau}, \tag{6.55}$$

https://doi.org/10.1017/jfm.2019.909 Published online by Cambridge University Press

where

$$\left.\begin{aligned} B_0^{(m)}(\bar{x}) &= \sum_{k=-\infty}^{\infty} A^{(k)*}(\bar{x})A^{(m+k)}(\bar{x}), \quad B_1^{(m)}(\bar{x}) = c^{-1}\sum_{k=-\infty}^{\infty} A^{(k)*}(\bar{x})\frac{\partial A^{(m+k)}(\bar{x})}{\partial \bar{x}}, \\ B_2^{(m)}(\bar{x}) &= \sum_{k=-\infty}^{\infty} A^{(k)*}(\bar{x})\left[\frac{\partial}{\partial \bar{x}} - \mathrm{i}(m+k)\Delta\right]A^{(m+k)}(\bar{x}). \end{aligned}\right\} \tag{6.56}$$

It follows that the Fourier transform of B_j is

$$\hat{\hat{B}}_j(\omega, \kappa) = 2\pi\delta(m\omega_v - \omega)\mathscr{F}_{\bar{x}\to\kappa}[B_j^{(m)}(\bar{x})] \quad (j = 0, 1, 2). \tag{6.57}$$

Similarly, the Fourier transform of T_0 is

$$\hat{\hat{T}}_0(\omega, \kappa, \eta) = 2\pi\delta(m\omega_v - \omega)\mathscr{F}_{\bar{x}\to\kappa}[T_0^{(m)}(\bar{x}, \eta)]. \tag{6.58}$$

It is possible and informative to express $\mathscr{S}_\pm$ and $\mathscr{D}_\pm$ in terms of $\mathscr{S}_\pm^{(m)}(\bar{\theta})$ and $\mathscr{D}_\pm^{(m)}(\bar{\theta})$, which are defined for each frequency $\omega_m = m\omega_v$. Obviously, $\mathscr{S}_\pm$ are functions of $\mathcal{U}$, $\mathcal{S}$ and $\mathcal{Y}$, which are all functions of $B_j(\tau, \bar{x})$. When B_j is written as a Fourier series (6.55), so are $\mathcal{U}$, $\mathcal{S}$ and $\mathcal{Y}$. Correspondingly, the Fourier integral (5.46) becomes a Fourier series as well with $\mathscr{S}_\pm$ taking discrete values $\mathscr{S}_\pm^{(m)}(\bar{\theta})$, selected by the Dirac function $\delta(m\Delta - \omega)$ $(m = 0, \pm1, \pm2, \ldots)$. It follows that $\mathscr{D}_\pm$ (see (5.48)) can be written as

$$\mathscr{D}_\pm(\bar{\theta}) = \sqrt{\sum_{m=-\infty}^{\infty}[\mathscr{D}_\pm^{(m)}(\bar{\theta})]^2}, \quad \mathscr{D}_\pm^{(m)}(\bar{\theta}) = |\Theta(\bar{\theta})||\mathscr{S}_\pm^{(m)}(\bar{\theta})|\omega_v. \tag{6.59a,b}$$

In the case of a continuous sideband, solving the evolution system by Fourier transform with respect to τ, we have $\widehat{A}(\omega, \bar{x})$, $\partial\widehat{A}(\omega, \bar{x})/\partial\bar{x}$ and $\widehat{T}(\omega, \bar{x})$. Then performing convolution, we evaluate $\widehat{B}_j(\omega, \bar{x})$:

$$\left.\begin{aligned} \widehat{B}_0(\omega, \bar{x}) &= \widehat{A}^*(\omega, \bar{x}) * \widehat{A}(\omega, \bar{x}), \quad \widehat{B}_1(\omega, \bar{x}) = c^{-1}\widehat{A}^*(\omega, \bar{x}) * \frac{\partial\widehat{A}(\omega, \bar{x})}{\partial\bar{x}}, \\ \widehat{B}_2(\omega, \bar{x}) &= \widehat{A}^*(\omega, \bar{x}) * \left[\left(\frac{\partial}{\partial\bar{x}} - \mathrm{i}\omega\right)\widehat{A}(\omega, \bar{x})\right]. \end{aligned}\right\} \tag{6.60}$$

Further Fourier transforms of $\widehat{B}_j$ and $\widehat{T}_0$ with respect to $\bar{x}$ give

$$\hat{\hat{B}}_j(\omega, \kappa) = \mathscr{F}_{\bar{x}\to\kappa}[\widehat{B}_j(\omega, \bar{x})] \quad (j = 0, 1, 2), \quad \hat{\hat{T}}_0(\omega, \kappa) = \mathscr{F}_{\bar{x}\to\kappa}[\widehat{T}_0(\omega, \bar{x})], \tag{6.61a,b}$$

which are then used in (6.52)–(6.54) to calculate the physical sources of sound.

Figure 15(*a*) shows the directivity of the sound waves with different frequencies $\omega_m = m\omega_v$ $(m = 1, 2, 3, 4)$ in case $\mathcal{H}$. The acoustic field features broadly a four-lobed directivity pattern, characteristic of quadrupole radiation that the acoustic analogy theory would predict, and indeed such four- or multi-lobed patterns were predicted for sound waves generated by vortex pairing (Colonius, Lele & Moin 1997; Cheung & Lele 2009). However, the connection of the present theoretical result with a quadrupole is somewhat fortuitous, because the source, the slowly modulated mean

https://doi.org/10.1017/jfm.2019.909 Published online by Cambridge University Press

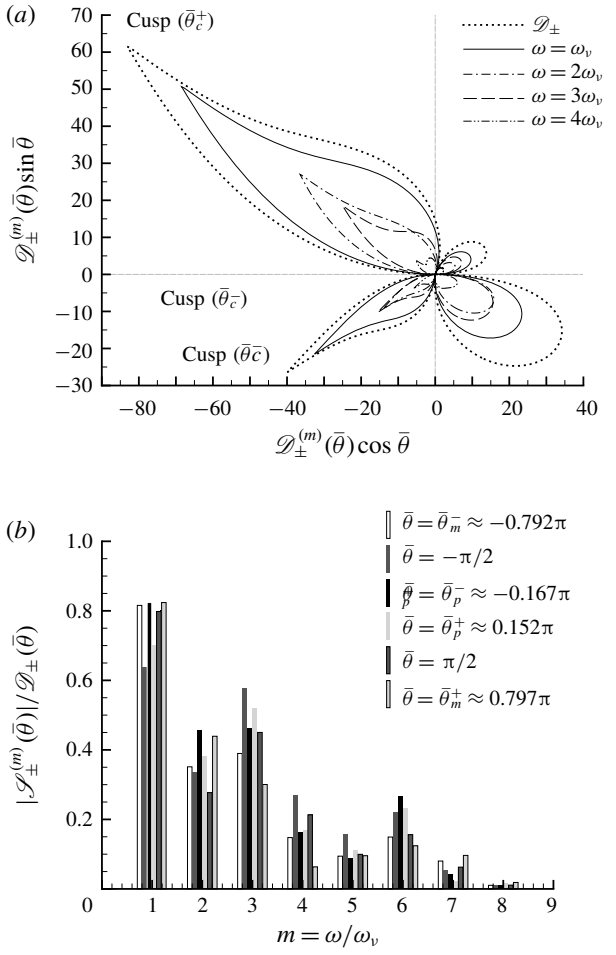

FIGURE 15. The acoustic field radiated from a modulated CS with discrete sidebands in case $\mathcal{H}$. (*a*) Directivity of the sound wave emitted by each low-frequency sideband with $\omega_m = m\omega_v$ $(m = 1, 2, 3, 4)$. The overall directivity of the acoustic field is also shown. (*b*) Spectrum at different radiation directions $\bar{\theta} = \bar{\theta}_p^\pm$, $\bar{\theta}_m^\pm$ (the directions of maximal $\mathscr{D}_\pm$) and $\pm\pi/2$.

flow, is non-compact, for which a multipolar interpretation of radiation is not attainable in general. The two downstream beaming lobes in the first and fourth quadrants are smooth. Interestingly, the two upstream beaming lobes in the second and third quadrants each display a cusp. This is caused by the acoustic interactions between $\bar{y} > 0$ and $\bar{y} < 0$ regions. When the radiation direction $\bar{\theta} \in (143.50°, 180.00°)$ in the upper half-plane, $\widehat{\mathcal{E}}_+$ remains an imaginary number, but $\widehat{\mathcal{E}}_-$ becomes a real number. Physically, when $\bar{\theta}$ crosses the angle $\bar{\theta}_c^+ \approx 143.50°$, the corresponding $\widehat{P^-}$ is no longer a travelling wave at this wavenumber κ_s^+ and instead decays exponentially in the normal direction, so that the directivity is distorted. The cusp in the lower half-plane appears for a similar reason. Basically, whenever $[Ma^2(\bar{U}_\pm/c - \omega/\kappa_s^\mp)^2 - \bar{T}_\pm/c^2]$ change their signs, a cusp appears in the other half-plane. Obviously, the angles of the cusps are only determined by the property of the main shear layer. Contrary

https://doi.org/10.1017/jfm.2019.909 Published online by Cambridge University Press

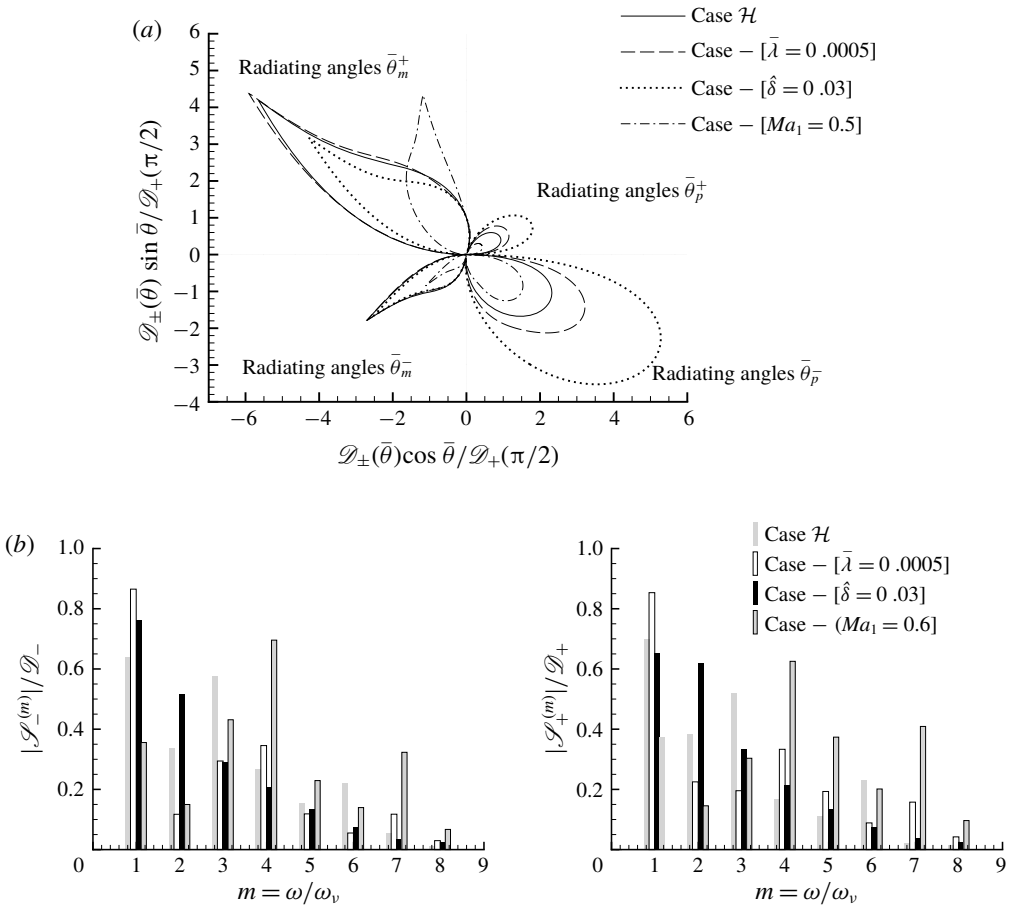

FIGURE 16. The overall acoustic field radiated by modulated CS with discrete sidebands in different cases: case $\mathcal{H}$, case $-$ [$\bar{\lambda} = 0.0005$], case $-$ [$\hat{\delta} = 0.03$], case $-$ [$Ma_1 = 0.5$]. (*a*) Directivity. (*b*) The spectrum at the radiating angles $\bar{\theta} = -\pi/2$ (left) and $\bar{\theta} = \bar{\theta}_p^+$ (right) in different cases.

to one's intuition, the acoustic radiations to the upper and lower far fields are not passive or independent, but interfere with each other. This is possible because they both act to influence the equivalent sources. The directivity of different low-frequency components appears familiar. The radiated sound waves concentrate in a beam with an angle of $\bar{\theta}_p^+ \approx 27.3^\circ$ in $\bar{y} > 0$ region and of $\bar{\theta}_p^- \approx -30.0^\circ$ in $\bar{y} < 0$ region respectively. The directivity of the overall acoustic fields is also shown in figure 15(*a*).

Furthermore, the spectrum of the sound at different angles could be also found. We select the radiating angles $\bar{\theta}_p^\pm$ and $\bar{\theta}_m^\pm$, the directions of the beams, as well as $\pm\pi/2$ in the following presentations. Figure 15(*b*) shows the spectrum at these angles. Because of the significant strength difference at different angles, the spectrum is normalised by $\mathscr{D}_\pm$. The first three components have strong magnitudes, of which $\omega_1 = \omega_v$ is the strongest.

It is of interest to examine how the flow parameters affect the radiation qualitatively. The effects of Ma, $\hat{\delta}$ and $\bar{\lambda}$ are shown in figure 16(*a*). As the sound strength ($\tilde{P}_{rms}^\pm$) varies by several orders of magnitude from case to case, we present the directivity

https://doi.org/10.1017/jfm.2019.909 Published online by Cambridge University Press

Cases	$\bar{\theta}_p^+$	$\bar{\theta}_p^-$	$\bar{\theta}_m^+$	$\bar{\theta}_m^-$	$\mathrm{SPL}_{max}(\bar{R}=10\delta)$
Case $\mathcal{H}$	27.3°	−30.0°	143.5°	−146.6°	152.86 dB
Case – $[\bar{\lambda}=0.0005]$	28.9°	−28.4°	143.5°	−146.6°	174.80 dB
Case – $[\hat{\delta}=0.03]$	25.1°	−28.1°	143.5°	−146.6°	153.07 dB
Case – $[Ma_1=0.5]$	30.7°	−36.6°	105.2°	−142.5°	175.87 dB

TABLE 1. Beam angles $\bar{\theta}_p^{\pm}$ and $\bar{\theta}_m^{\pm}$ and the maximum sound pressure level at the distance $\bar{R}=10\delta$ of the acoustic field radiated by modulated CS with discrete sidebands in different cases.

Cases	$\bar{\theta}_p^+$	$\bar{\theta}_p^-$	$\mathrm{SPL}_{max}(\bar{R}=10\delta)$
$6d=0.125\omega_0$	28.9°	−30.8°	108.98 dB
$6d=0.25\omega_0$	28.5°	−30.9°	117.17 dB
$6d=0.5\omega_0$	28.1°	−30.8°	126.86 dB
$6d=0.75\omega_0$	26.9°	−29.2°	129.18 dB

TABLE 2. Beam angles $\bar{\theta}_p^{\pm}$ and the maximum sound pressure level at the distance $\bar{R}=10\delta$ of the acoustic field radiated by the modulated CS with continous sidebands for different initial bandwidths.

normalised by $\mathscr{D}_{\pm}(\pi/2)$ in each case. Table 1 lists the main characteristics of the acoustic fields for the four cases considered. Obviously, the Mach number, Ma_1 or Ma, has a greater effect than the other two parameters. Figure 16(*b*) shows the normalised spectrum in the four different cases at radiating angles $\bar{\theta}=-\pi/2$ and $\bar{\theta}=\bar{\theta}_p^+$. The peak radiation occurs at ω_v for $\bar{\lambda}=0.0005$ and $\hat{\delta}=0.03$ cases, but shifts to a higher frequency $4\omega_v$ for $Ma_1=0.5$.

The acoustic field generated by a CS with a continuum of sidebands is also calculated. As the calculation becomes much more costly, only one set of results is given to show the qualitative characteristics here. As indicated by (4.36), a continuous-sideband CS is characterised by d, the rescaled bandwidth of the initial spectrum, and the unscaled bandwidth is $\epsilon^{1/2}d$. Here we take $6d=0.125\omega_0$, $0.25\omega_0$, $0.5\omega_0$ and $0.75\omega_0$, where $6d$ is given by the '3σ law' in the Gaussian distribution (4.36), and ω_0 is the frequency of the fundamental disturbance.

The directivity for each of these initial-spectrum bandwidths is displayed in figure 17(*a*). Clearly, the bandwidth has little influence on the beam angles. The main features of the acoustic field are summarised in table 2. The overall initial intensity remains 1 as d varies, but the radiated strength increases with the bandwidth. The latter may be explained by the fact that for a broader sideband, more components would interact nonlinearly with each other, causing more severe jittering of the wavepacket. In the opposite limit of $d\to 0$, the CS tends to be a single-frequency perturbation, which does not radiate any sound wave.

The rescaled spectra are displayed in figure 17(*b*). Instead of ω, here we introduce the Strouhal number,

$$St(\omega)=\epsilon^{1/2}L_0^*f^*/U_0^*=\epsilon^{1/2}\omega/(2\pi), \tag{6.62}$$

with $\epsilon^{1/2}f^*$ being the physical frequency of the radiated sound waves in Hertz (Hz). The radiating frequency band covers $St\approx 0\sim 0.05$, whereas the carrier wave

https://doi.org/10.1017/jfm.2019.909 Published online by Cambridge University Press

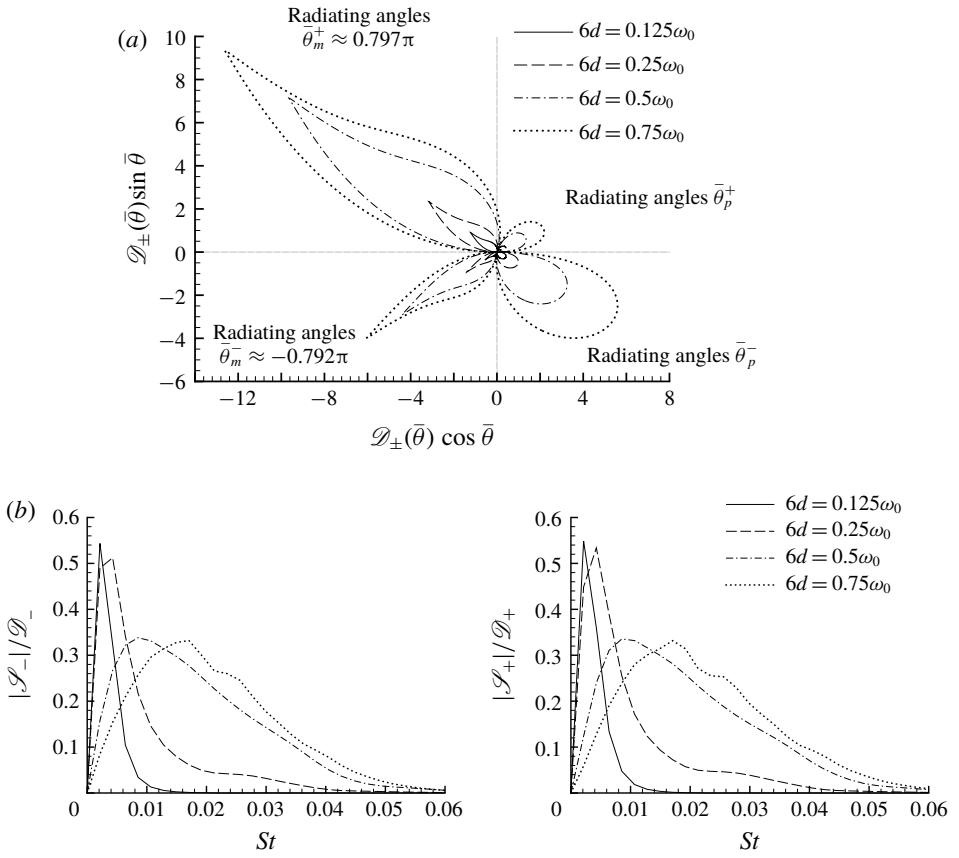

FIGURE 17. The acoustic field radiated by a modulated CS with continuous sidebands for different initial bandwidths $6d = 0.125\omega_0$, $0.25\omega_0$, $0.5\omega_0$ and $0.75\omega_0$. (*a*) Directivity. (*b*) The spectrum at radiating angles $\bar{\theta} = -\pi/2$ (left) and $\bar{\theta} = \bar{\theta}_p^+$ (right).

of the wavepacket has the Strouhal number $\epsilon^{-1/2}St_0 = \omega_0/(2\pi) \approx 0.46$ in all the cases displayed. In the directions $\bar{\theta} = -\pi/2$ and $\bar{\theta}_p^+$, the radiation shifts to higher frequencies with the increase of the bandwidth. As expected, in the case of a very narrow initial bandwidth $6d = 0.125\omega_0$, radiation is restricted to a small band of very low frequencies.

7. Conclusions and discussion

7.1. *Summary and conclusions*

In this paper, a mathematical theory was developed to describe the nonlinear dynamics of CS in a subsonic turbulent free shear layer, by adopting the semi-empirical model that CS can be treated as instability waves, or wavepackets, as a first approximation. The strongly nonlinear–non-equilibrium critical-layer theory for laminar flows was applied to turbulent mixing layers to derive an evolution system, which consists of the amplitude equation, the temperature and vorticity equations supplemented by appropriate initial and boundary conditions. The present work was an extension of the incompressible coherent-structure theory (Wu & Zhuang 2016) to the compressible case. It is also an extension of the unified theory for subsonic instability modes

https://doi.org/10.1017/jfm.2019.909 Published online by Cambridge University Press

(Sparks & Wu 2008) to turbulent flows. Furthermore, the acoustic radiation process is analysed, leading to identification of the real acoustic sources, and a theory was developed to predict the directivity and spectrum of the radiated acoustic field.

Concerning the dynamics of CS, the theoretical development took several steps. First, through the Favre phase average the flow field is decomposed into three parts: the mean flow, the CS and small-scale fluctuations. Second, the effect of small-scale fluctuations on CS is accounted for by using a generalised gradient closure model, which allows for possible time-delay effects. Third, the nonlinear development of the CS is analysed based on the large-Reynolds-number assumption. The asymptotic scalings were chosen such that non-equilibrium, viscous and nonlinear effects all appear at leading order in the critical layer. Most significantly, particular attention is paid to the fact that turbulent shear flows develop in the streamwise direction rather rapidly, and so the associated non-parallelism is retained at leading order in the governing system. Specifically, as part of the non-parallel-flow effects, the transverse velocity of the mean flow is found to play a leading-order role, and its profile was deduced from the continuity and momentum equations by matching the main mixing layer with the far field. The Fourier-component forms of the governing equations for the amplitude, temperature and vorticity were deduced, and so were the appropriate initial and boundary conditions. A suitable velocity profile was chosen to mimic the mean flow in practice. The required parameters such as neutral wavenumber and frequency were obtained by solving the compressible Rayleigh equation.

Numerical solutions of the evolution system for a single-frequency wave showed that the theory captured the most important features in the development of CS: roll-up and attenuation of large-scale vortices. We studied the influence of key parameters on the evolution of CS, including the non-parallelism (which also causes a transverse drift of the critical level), viscosity, compressibility, temperature ratio and turbulence intensity (represented by q_c). Among these, non-parallelism, viscosity and incompressibility were found to inhibit CS.

A study was also made of more general and realistic CS consisting of sidebands, with particular attention to their spectral evolution and amplitude-phase modulation. Numerical results showed that if only one sideband was seeded upstream, the other one would soon be excited, and the interactions of sidebands in the early stage of the evolution lead to the enhancement of one sideband. The amplitude of the lower-frequency sideband of the fundamental mode exceeded those of the central mode causing its upper sideband to become the dominant component. The excitation and evolution of high harmonics and their sidebands were also monitored. The upper sideband of each harmonic is stronger than the lower one at the beginning, but its growth rate is lower than that of the latter, which rises rapidly, overtaking the central harmonics and upper sidebands. In this process, a mean-flow distortion and low-frequency components are generated, and they acquire fairly large magnitudes before attenuating rather slowly. The development of these components leads to the broadening of the coherent-structure spectrum. The nonlinear dynamics involves a forward energy transfer from the fundamental to harmonics, a local inverse cascade from each harmonic to its lower sidebands and a global back scatting from the fundamental, harmonics and their sidebands to the mean flow and low-frequency fluctuations. The nonlinear behaviour may also be characterised by the amplitude and phase of the complex amplitude of CS being modulated over the time scale $2\pi/\omega_{\nu}$. The modulation is rather gradual and regular upstream but becomes increasingly abrupt and irregular as the disturbance propagates downstream. The roller structures of the CS, as represented by the critical-layer temperature and vorticity, undergo periodic breathing, and change their appearance appreciably.

https://doi.org/10.1017/jfm.2019.909 Published online by Cambridge University Press

By analysing the far-field asymptotic behaviour of the perturbation, we elucidated how CS radiate sound waves. The fast-varying unsteady components such as the fundamental and its harmonics as well as their sidebands all remain trapped within the shear layer without generating any sound waves. The slowly varying mean-flow distortion, driven by the nonlinear interaction of the wavepacket, emits low-frequency sound waves. The physical source was found to consist of these parts: the transverse velocity jump across the critical layer, induced by the nonlinear interactions in the critical layer, the transverse velocity and pressure jumps across the main shear layer, both induced by the wavepacket interactions in the main layer. Our asymptotic analysis shows that the transverse velocities at the outer edges of the shear layer appear in the Neumann boundary condition on the acoustic wave equation, and thus may be interpreted as the equivalent sources in the context of Lighthill type acoustic analogy. However, contrary to the premise of the classical acoustics analogy, the equivalent sound sources cannot be pre-determined before solving the acoustic equation, and have to be determined along with the radiated sound. This may be interpreted as the latter acting back on the sources. As a result, the radiation processes to the upper and lower far fields are inter-dependent, which leads to a cusp appearing on each of the two upstream beams. Numerical results are presented to show the directivity and spectrum of the sound radiated by modulated CS. The acoustic fields feature a four-lobed directivity pattern that is characteristic of quadrupole radiation despite the fact that the sources are not compact, for which the concept of acoustic multipoles is not, strictly speaking, applicable.

The present paper focuses on the low-frequency sound waves emitted by the nonlinear interactions of wavepackets. In general, the acoustic field consists of also the directly radiated sound waves, whose frequencies are comparable with that of the carries wave (Tam & Morris 1980; Cavalieri *et al.* 2012). The effectiveness of both radiation mechanisms is influenced by jittering, which is in turn controlled by nonlinear effects. With increased jittering the spectrum of the low-frequency sound waves extends towards higher frequencies while the direct radiation becomes stronger.

7.2. *Reflection and prospect*

The theory presented in this paper is fairly general, valid for any shear flow that is inviscidly unstable, in the incompressible or compressible regime. With the eddy conductivity and viscosity being set to zero, it is applicable to laminar flows. After substituting the parameters of the mean flow and making minor modifications to the governing equations, the theory can be applied to planar jets and wakes, and indeed to wall-bounded shear flows as well, laminar or turbulent. Turbulent circular jets arise in various applications, and the CS play a significant role in fluid mixing and noise generation. Extension to that case is in progress.

However, several assumptions made in the paper may be improved. For the phase-averaged Reynolds stresses of small-scale fluctuations, we employed the gradient models with the eddy conductivity and viscosity, which included the effects of time relaxations. A better closure model needs to be developed by treating the shear stresses as independent variables and coupling them with the flow quantities. The spreading rate of the shear-layer momentum thickness, which measures non-parallelism, is not always a constant in practice, but is influenced by the CS as well. Future research would consider coupling it with the evolution of the CS. The present theory was based on the high-Reynolds-number assumption and made extensive use of matched asymptotic expansion and multiple scale methods.

https://doi.org/10.1017/jfm.2019.909 Published online by Cambridge University Press

The theory has, on the one hand, the advantage that it probes into the radiation process and identifies the true physical sources of sound, thereby predicting the sound emission on that basis. It has revealed several features different from what the existing acoustic analogy approach envisages, the implication of which requires further investigation. On the other hand, for engineering applications it would be of interest to develop a simpler approach which captures the features and effects revealed here, but does not involve all of the complicated asymptotic analysis. One possibility is to use the nonlinear PSE approach to predict the nonlinear evolution of the CS, but retain the formalism for the acoustic radiation including the expressions for the physical sources. The data from the PSE calculations could be used to evaluate these sources directly whereby predicting the acoustic far field.

Acknowledgements

This investigation was supported by the Natural Science Foundation of China (NSFC grant no. 11472190). We would like to thank the reviewers for their comments and suggestions, which helped us improve the manuscript.

Appendix A. Outer solution for the velocities, temperature and density in terms of $\hat{p}_0$

The leading-order solution for the velocity, temperature and density is found from (3.16)–(3.20) as,

$$\hat{v}_0 = \frac{\mathrm{i}\bar{T}}{\alpha(\bar{U}-c)}\hat{p}_0', \quad \hat{u}_0 = -\frac{\bar{T}}{\bar{U}-c}\hat{p}_0 - \frac{\bar{T}\bar{U}'}{\alpha^2(\bar{U}-c)^2}\hat{p}_0', \tag{A 1a,b}$$

$$\hat{T}_0 = -\frac{\bar{T}\bar{T}'}{\alpha^2(\bar{U}-c)^2}\hat{p}_0' + (\gamma-1)Ma^2\bar{T}\hat{p}_0, \tag{A 2}$$

$$\hat{\rho}_0 = \frac{\bar{T}'}{\alpha^2(\bar{U}-c)^2\bar{T}}\hat{p}_0' + \frac{Ma^2}{\bar{T}}\hat{p}_0. \tag{A 3}$$

The second-order solution for $\hat{q}_1^{\langle 1\rangle}$ in (3.15) is found from (3.29)–(3.33) as,

$$\hat{v}_1^{\langle 1\rangle} = \frac{\mathrm{i}\bar{T}}{\alpha(\bar{U}-c)}\hat{p}_1^{\langle 1\rangle\prime} - \frac{\bar{T}\hat{p}_0'}{\alpha^2(\bar{U}-c)^2}\mathcal{D}_1A^\dagger - \frac{\mathrm{i}\bar{T}\hat{p}_0'}{\alpha(\bar{U}-c)}\left(\frac{\bar{U}_1}{\bar{U}-c} - \frac{\bar{T}_1}{\bar{T}}\right)\bar{x}A^\dagger, \tag{A 4}$$

$$\begin{aligned}\hat{u}_1^{\langle 1\rangle} = {} & -\frac{\bar{T}}{\bar{U}-c}\hat{p}_1^{\langle 1\rangle} - \frac{\bar{T}\bar{U}'}{\alpha^2(\bar{U}-c)^2}\hat{p}_1^{\langle 1\rangle\prime} \\ & - \left[\frac{\mathrm{i}\bar{T}\hat{p}_0}{\alpha(\bar{U}-c)^2} + \frac{2\mathrm{i}\bar{T}\bar{U}'\hat{p}_0'}{\alpha^3(\bar{U}-c)^3}\right]\mathcal{D}_1A^\dagger + \frac{\mathrm{i}\bar{T}\hat{p}_0}{\alpha c(\bar{U}-c)}\frac{\partial A^\dagger}{\partial\bar{x}} \\ & + \left[\left(\frac{\bar{U}_1\bar{T}}{\bar{U}-c} - \bar{T}_1\right)\frac{\hat{p}_0}{\bar{U}-c} + \left(\frac{2\bar{U}_1}{\bar{U}-c} - \frac{\bar{U}_1'}{\bar{U}'} - \frac{\bar{T}_1}{\bar{T}}\right)\frac{\bar{T}\bar{U}'\hat{p}_0'}{\alpha^2(\bar{U}-c)^2}\right]\bar{x}A^\dagger,\end{aligned} \tag{A 5}$$

https://doi.org/10.1017/jfm.2019.909 Published online by Cambridge University Press

$$\hat{T}_1^{\langle 1\rangle} = -\frac{\bar{T}\bar{T}'}{\alpha^2(\bar{U}-c)^2}\hat{p}_1^{\langle 1\rangle\prime} + (\gamma-1)Ma^2\bar{T}\hat{p}_1^{\langle 1\rangle} - \frac{2\mathrm{i}\bar{T}'\bar{T}\hat{p}_0'}{\alpha^3(\bar{U}-c)^3}\mathcal{D}_1A^\dagger + \left[(\gamma-1)Ma^2\bar{T}_1\hat{p}_0 + \left(\frac{2\bar{U}_1\bar{T}'}{\bar{U}-c} - \frac{\bar{T}_1\bar{T}'+\bar{T}_1'\bar{T}}{\bar{T}}\right)\frac{\bar{T}\hat{p}_0'}{\alpha^2(\bar{U}-c)^2}\right]\bar{x}A^\dagger, \quad \text{(A 6)}$$

$$\hat{\rho}_1^{\langle 1\rangle} = \frac{\bar{T}'}{\alpha^2(\bar{U}-c)^2\bar{T}}\hat{p}_1^{\langle 1\rangle\prime} + \frac{Ma^2}{\bar{T}}\hat{p}_1^{\langle 1\rangle} + \frac{2\mathrm{i}\bar{T}'\hat{p}_0'}{\alpha^3(\bar{U}-c)^3\bar{T}}\mathcal{D}_1A^\dagger - \frac{1}{\bar{T}^2}\left[\gamma Ma^2\bar{T}_1\hat{p}_0 + \left(\frac{2\bar{U}_1\bar{T}'}{\bar{U}-c} - \frac{\bar{T}_1}{\bar{T}}\right)\frac{\bar{T}\hat{p}_0'}{\alpha^2(\bar{U}-c)^2}\right]\bar{x}A^\dagger. \quad \text{(A 7)}$$

Note that $\hat{p}_1^{\langle 1\rangle}$, the inhomogeneous solution to (3.35), can be expressed in terms of $\hat{p}_0$, as (3.37) indicates.

Appendix B. Coefficients in (4.23)

The coefficients in the truncated amplitude equation (4.23) are as follows:

$$\left.\begin{aligned}
\tilde{\Lambda}_1 &= (q_1 - q_2\bar{x})[\Lambda_1 - 2\mathrm{i}(S_0 + p_1p_3\chi + \chi_2\bar{x})/\tilde{H}] \\
&\quad + \frac{2}{\tilde{H}}\left\{l_1 + l_2\bar{x} - \frac{\Lambda_d}{\Lambda_2}\left[(\Lambda_0 - 2p_3\chi_1\chi/\tilde{H})\bar{x} - S_1\right] + \frac{2\mathrm{i}\chi_2\Lambda_d}{\tilde{H}\Lambda_2}\right\}, \\
\tilde{\Lambda}_2 &= (q_1 - q_2\bar{x})[\Lambda_2 - 2\mathrm{i}(S_0 + p_1p_3\chi + \chi_2\bar{x})/\tilde{H}] + 2(l_1 + l_2\bar{x})/\tilde{H}, \\
\tilde{\Lambda}_{d,j} &= \frac{2\Lambda_d}{\tilde{H}\Lambda_2}[\Lambda_2 - 2\mathrm{i}(S_0 + p_1p_3\chi + \chi_2\bar{x})/\tilde{H} + \Lambda_j] \quad (j=1,2), \\
\tilde{\Lambda}_0 &= (q_1 - q_2\bar{x})[(\Lambda_0 - 2p_3\chi_1\chi/\tilde{H})\bar{x} - S_1 - 2\mathrm{i}\chi_2/\tilde{H}] + 2(r_1 + r_2\bar{x})/\tilde{H},
\end{aligned}\right\} \quad \text{(B 1)}$$

with

$$\left.\begin{aligned}
S_1 &= 2(\mathrm{i}S_0\Lambda_1 + S_0p_1p_3\chi + p_2p_3\chi)/\tilde{H}, \\
q_1 &= \Lambda_2 - \frac{2\mathrm{i}}{\tilde{H}}(S_0 + p_1p_3\chi) - \frac{4}{\Lambda_2} + \frac{2S_1}{\tilde{H}\Lambda_2}, \quad q_2 = \frac{2\mathrm{i}\chi_2}{\tilde{H}} + \frac{2}{\tilde{H}\Lambda_2}\left(\Lambda_0 - \frac{2p_3\chi_1\chi}{\tilde{H}}\right), \\
l_1 &= -2\tilde{H} + S_1 - \frac{4\mathrm{i}}{\Lambda_2}(S_0 + p_1p_3\chi) + \frac{4}{\tilde{H}\Lambda_2}\left(\Lambda_0 - \frac{2p_3\chi_1\chi}{\tilde{H}}\right) + \frac{4\mathrm{i}\chi_2}{\tilde{H}}, \\
l_2 &= -(\Lambda_0 - 2p_3\chi_1\chi/\tilde{H}) - 4\mathrm{i}\chi_2/\Lambda_2, \\
r_1 &= 2\mathrm{i}(S_0 + p_1p_3\chi)\tilde{H} - (\Lambda_0 - 2p_3\chi_1\chi/\tilde{H}) - 4\mathrm{i}\chi_2/\Lambda_2, \quad r_2 = 2\mathrm{i}\chi_2\tilde{H}.
\end{aligned}\right\} \quad \text{(B 2)}$$

Appendix C. Expressions for the functions in $\mathcal{S}$ and $\mathcal{Y}$

In the analysis of acoustic radiation, the physical acoustic sources, $\widehat{\mathcal{S}}$ (see (5.7)) and $\widehat{\mathcal{Y}}$ (see (5.15)) involve functions $S_{ik}^\dagger(y)$ and $G_{jk}^\dagger(y)$ $(i,k=1,2,3;\ j=0,1,2)$. They are expressed in terms of the mean-flow profiles $(\bar{U},\ \bar{T})$, the eigenvalue α and the associated eigenfunction $\hat{p}_0(y)$ as follows.

https://doi.org/10.1017/jfm.2019.909 Published online by Cambridge University Press

C.1. *Expressions for the functions in* $\mathcal{S}$

Inserting (A 1)–(A 7) and $\hat{p}_1^{(1)}(y)$ into (5.6), we have the functions $S_{ik}^{\dagger}(y)$ in (5.7),

$$\left.\begin{aligned}
S_{11}^{\dagger}(y) &= (\gamma+1)Ma^2\bar{T} - \frac{\bar{T}^2}{(\bar{U}-c)^2} - (2\gamma+1)Ma^4(\bar{U}-c)^2,\\
S_{12}^{\dagger}(y) &= \frac{\bar{U}''\bar{T}^2}{\alpha^4(\bar{U}-c)^3} + \frac{\bar{T}^2}{\alpha^2(\bar{U}-c)^2} - \frac{\bar{U}'^2\bar{T}^2}{\alpha^4(\bar{U}-c)^4} + \frac{2\bar{U}'\bar{T}'\bar{T}}{\alpha^2(\bar{U}-c)^3} - \frac{3Ma^2\bar{T}}{\alpha^2},\\
S_{13}^{\dagger}(y) &= \frac{5\bar{T}'\bar{T}}{\alpha^2(\bar{U}-c)^2} - \frac{2\bar{U}'\bar{T}^2}{\alpha^2(\bar{U}-c)^3} - \frac{2\bar{U}'\bar{T}Ma^2}{\alpha^2(\bar{U}-c)} - \frac{(\gamma+3)Ma^2\bar{T}'}{\alpha^2};\\
S_{21}^{\dagger}(y) &= -\frac{Ma^2\bar{T}}{(\bar{U}-c)^2} - (\gamma-2)Ma^4, \quad S_{22}^{\dagger}(y) = \frac{\bar{T}'^2}{\alpha^4(\bar{U}-c)^4} - \frac{3Ma^2\bar{T}}{\alpha^2(\bar{U}-c)^2},\\
S_{23}^{\dagger}(y) &= \frac{4\bar{T}'\bar{T}}{\alpha^2(\bar{U}-c)^4} - \frac{2(\gamma+1)Ma^2\bar{U}'\bar{T}}{\alpha^2(\bar{U}-c)^3} - \frac{6Ma^4\bar{T}'}{\alpha^2(\bar{U}-c)^2};\\
S_{31}^{\dagger}(y) &= -(3\gamma-1)Ma^4(\bar{U}-c) - \frac{(\gamma-1)\bar{T}Ma^2}{\bar{U}-c},\\
S_{32}^{\dagger}(y) &= \frac{\bar{U}''\bar{T}^2}{\alpha^4(\bar{U}-c)^4} - \frac{6Ma^2\bar{T}}{\alpha^2(\bar{U}-c)} + \frac{\bar{T}'^2}{\alpha^4(\bar{U}-c)^3} + \frac{2\bar{T}'\bar{U}'\bar{T}}{\alpha^2(\bar{U}-c)^4},\\
S_{33}^{\dagger}(y) &= \frac{8\bar{T}'\bar{T}}{\alpha^2(\bar{U}-c)^3} + \frac{(\gamma-9)Ma^2\bar{T}'}{\alpha^2(\bar{U}-c)} - \frac{2(\gamma+2)Ma^2\bar{U}'\bar{T}}{\alpha^2(\bar{U}-c)^2}.
\end{aligned}\right\} \tag{C 1}$$

C.2. *Expressions for the functions in* $\mathcal{Y}$

Following the similar procedure for (5.13), we obtain the functions $G_{jk}^{\dagger}(y)$ in (5.16),

$$\left.\begin{aligned}
G_{11}^{\dagger}(y) &= \frac{\bar{T}\hat{p}_0'^2}{\alpha^3(\bar{U}-c)^2}\left(\frac{\bar{T}'}{\bar{T}} - \frac{2\bar{U}'}{\bar{U}-c}\right),\\
G_{12}^{\dagger}(y) &= \frac{2}{\alpha}\left[1 - \frac{Ma^2(\bar{U}-c)^2}{\bar{T}}\right] - \frac{2\hat{p}_0'}{\alpha^3\hat{p}_0}\left(\frac{\bar{T}'}{\bar{T}} - \frac{2\bar{U}'}{\bar{U}-c}\right),\\
G_{13}^{\dagger}(y) &= \frac{4\hat{p}_0'}{\alpha}\left[\frac{\bar{T}}{(\bar{U}-c)^2} - Ma^2\right] - \frac{2\bar{T}\hat{p}_0'^2}{\alpha^3(\bar{U}-c)^2\hat{p}_0}\left(\frac{\bar{T}'}{\bar{T}} - \frac{2\bar{U}'}{\bar{U}-c}\right);\\
G_{21}^{\dagger}(y) &= \frac{\bar{T}\hat{p}_0'^2}{\alpha^3(\bar{U}-c)^3}\left(\frac{\bar{T}'}{\bar{T}} - \frac{3\bar{U}'}{\bar{U}-c}\right) - \frac{2\bar{T}\hat{p}_0\hat{p}_0'}{\alpha(\bar{U}-c)^3},\\
G_{22}^{\dagger}(y) &= \frac{2}{\alpha}\left[\frac{Ma^2(\bar{U}-c)^2}{\bar{T}} - 1\right] + \frac{2\hat{p}_0'}{\alpha^3\hat{p}_0}\left(2 - \frac{\bar{T}'}{\bar{T}} - \frac{2\bar{U}'}{\bar{U}-c}\right),\\
G_{23}^{\dagger}(y) &= \frac{4\hat{p}_0'}{\alpha}\left[Ma^2 - \frac{\bar{T}}{(\bar{U}-c)^2}\right] + \frac{2\bar{T}\hat{p}_0'^2}{\alpha^3(\bar{U}-c)^2\hat{p}_0}\left(2 - \frac{\bar{T}'}{\bar{T}} - \frac{2\bar{U}'}{\bar{U}-c}\right);\\
G_{01}^{\dagger}(y) &= \frac{\bar{T}\hat{p}_0'^2}{\alpha^2(\bar{U}-c)^2}\left[\frac{3\bar{U}'\bar{U}_1}{(\bar{U}-c)^2} - \frac{\bar{T}'\bar{U}_1}{(\bar{U}-c)\bar{T}} - \frac{2\bar{T}'\bar{T}_1}{\bar{T}} - \frac{\bar{U}_1'}{\bar{U}-c} + \frac{\bar{T}_1'}{\bar{T}}\right]\\
&\quad + \hat{p}_0'\hat{p}_0\left[\frac{2\bar{U}_1\bar{T}}{(\bar{U}-c)^3} + (\gamma+1)\frac{Ma^2\bar{T}_1}{\bar{T}}\right],\\
G_{02}^{\dagger}(y) &= 1 - \frac{Ma^2(\bar{U}-c)^2}{\bar{T}} + \frac{\hat{p}_0'}{\alpha^2\hat{p}_0}\left(\frac{2\bar{U}'}{\bar{U}-c} + \frac{\bar{T}'}{\bar{T}} - 2\right),\\
G_{03}^{\dagger}(y) &= 2\hat{p}_0'\left[\frac{\bar{T}}{(\bar{U}-c)^2} - Ma^2\right] + \frac{\bar{T}\hat{p}_0'^2}{\alpha^2(\bar{U}-c)^2\hat{p}_0}\left(\frac{2\bar{U}'}{\bar{U}-c} + \frac{\bar{T}'}{\bar{T}} - 2\right).
\end{aligned}\right\} \tag{C 2}$$

https://doi.org/10.1017/jfm.2019.909 Published online by Cambridge University Press

REFERENCES

ANTONIA, R. A., CHAMBERS, A. J., BRITZ, D. & BROWNE, L. W. B. 1986 Organized structures in a turbulent plane jet: topology and contribution to momentum and heat transport. *J. Fluid Mech.* **172**, 211–229.

BAQUI, Y. B., AGARWAL, A., CAVALIERI, A. V. G. & SINAYOKO, S. 2015 A coherence-matched linear source mechanism for subsonic jet noise. *J. Fluid Mech.* **776**, 235–267.

BECHERT, D. & PFIZENMAIER, E. 1975 On the amplification of broad band jet noise by a pure tone excitation. *J. Sound Vib.* **43** (3), 581–587.

BECHERT, D. W. & PFIZENMAIER, E. 1977 Amplification of jet noise by a higher-mode acoustical excitation. *AIAA J.* **15** (9), 1268–1271.

BENEDDINE, S., SIPP, D., ARNAULT, A., DANDOIS, J. & LESSHAFFT, L. 2016 Conditions for validity of mean flow stability analysis. *J. Fluid Mech.* **798**, 485–504.

BRADSHAW, P. 1977 Compressible turbulent shear layers. *Annu. Rev. Fluid Mech.* **9** (1), 33–52.

BRIDGES, J. & HUSSAIN, F. 1992 Direct evaluation of aeroacoustic theory in a jet. *J. Fluid Mech.* **240**, 469–501.

BRIDGES, J. E. & HUSSAIN, A. K. M. F. 1987 Roles of initial condition and vortex pairing in jet noise. *J. Sound Vib.* **117** (2), 289–311.

BROWN, G. L. & ROSHKO, A. 1974 On density effects and large structure in turbulent mixing layers. *J. Fluid Mech.* **64**, 775–816.

CANTWELL, B. J. 1981 Organized motion in turbulent flow. *Annu. Rev. Fluid Mech.* **13**, 457–515.

CAVALIERI, A. V. G. & AGARWAL, A. 2014 Coherence decay and its impact on sound radiation by wavepackets. *J. Fluid Mech.* **748**, 399–415.

CAVALIERI, A. V. G., JORDAN, P., AGARWAL, A. & GERVAIS, Y. 2011 Jittering wave-packet models for subsonic jet noise. *J. Sound Vib.* **330** (18–19), 4474–4492.

CAVALIERI, A. V. G., JORDAN, P., COLONIUS, T. & GERVAIS, Y. 2012 Axisymmetric superdirectivity in subsonic jets. *J. Fluid Mech.* **704**, 388–420.

CAVALIERI, A. V. G., JORDAN, P., GERVAIS, Y., WEI, M. & FREUND, J. B. 2010 Intermittent sound generation and its control in a free-shear flow. *Phys. Fluids* **22** (11), 115113.

CAVALIERI, A. V. G., JORDAN, P. & LESSHAFFT, L. 2019 Wave-packet models for jet dynamics and sound radiation. *Appl. Mech. Rev.* **71** (2), 020820.

CAVALIERI, A. V. G., RODRIGUEZ, D., JORDAN, P., COLONIUS, T. & GERVAIS, Y. 2013 Wavepackets in the velocity field of turbulent jets. *J. Fluid Mech.* **730**, 559–592.

CHEUNG, L. C. & LELE, S. K. 2009 Linear and nonlinear processes in two-dimensional mixing layer dynamics and sound radiation. *J. Fluid Mech.* **625**, 321–351.

CLEMENS, N., MUNGAL, M., BERGER, T. & VANDSBURGER, U. 1990 Visualizations of the structure of the turbulent mixing layer under compressible conditions. *AIAA Paper* 1990-0709.

CLEMENS, N. T. & MUNGAL, M. G. 1992 Two- and three-dimensional effects in the supersonic mixing layer. *AIAA J.* **30** (4), 973–981.

CLEMENS, N. T. & MUNGAL, M. G. 1995 Large-scale structure and entrainment in the supersonic mixing layer. *J. Fluid Mech.* **284**, 171–216.

COHEN, J., MARASLI, B. & LEVINSKI, V. 1994 The interaction between the mean flow and coherent structures in turbulent mixing layers. *J. Fluid Mech.* **260**, 81–94.

COLONIUS, T., LELE, S. K. & MOIN, P. 1997 Sound generation in a mixing layer. *J. Fluid Mech.* **330**, 375–409.

COWLEY, S. J. 1985 Pulsatile flow through distorted channels: low-Strouhal-number and translating-critical-layer effects. *Q. J. Mech. Appl. Maths.* **38** (4), 589–619.

CRAWLEY, M., GEFEN, L., KUO, C. W., SAMIMY, M. & CAMUSSI, R. 2018 Vortex dynamics and sound emission in excited high-speed jets. *J. Fluid Mech.* **839**, 313–347.

CRIGHTON, D. G. & HUERRE, P. 1990 Shear-layer pressure fluctuations and superdirective acoustic sources. *J. Fluid Mech.* **220**, 355–368.

CROW, S. C. 1970 Aerodynamic sound emission as a singular perturbation problem. *Stud. Appl. Maths* **49** (1), 21–46.

CROW, S. C. & CHAMPAGNE, F. H. 1971 Orderly structure in jet turbulence. *J. Fluid Mech.* **48**, 547–591.

https://doi.org/10.1017/jfm.2019.909 Published online by Cambridge University Press

DIMOTAKIS, P. E. & BROWN, G. L. 1976 The mixing layer at high Reynolds number: large-structure dynamics and entrainment. *J. Fluid Mech.* **78**, 535–560.

ELLIOTT, G. S. & SAMIMY, M. 1990 Compressibility effects in free shear layers. *Phys. Fluids* A **2** (7), 1231–1240.

ELLIOTT, G. S., SAMIMY, M. & ARNETTE, S. A. 1995 The characteristics and evolution of large-scale structures in compressible mixing layers. *Phys. Fluids* **7** (4), 864–876.

FFOWCS WILLIAMS, J. E. & KEMPTON, A. J. 1978 The noise from the large-scale structure of a jet. In *Structure and Mechanisms of Turbulence II*, pp. 265–272. Springer.

FU, Z., AGARWAL, A., CAVALIERI, A. V. G., JORDAN, P. & BRÈS, G. A. 2017 Turbulent jet noise in the absence of coherent structures. *Phys. Rev. Fluids* **2** (6), 064601.

FUCHS, H. V. & MICHEL, U. 1978 Experimental evidence of turbulent source coherence affecting jet noise. *AIAA J.* **16** (9), 871–872.

GARNAUD, X., LESSHAFFT, L., SCHMID, P. J. & HUERRE, P. 2013 The preferred mode of incompressible jets: linear frequency response analysis. *J. Fluid Mech.* **716**, 189–202.

GASTER, M., KIT, E. & WYGNANSKI, I. 1985 Large-scale structures in a forced turbulent mixing layer. *J. Fluid Mech.* **150**, 23–39.

GOLDSTEIN, M. E. 1984 Aeroacoustics of turbulent shear flows. *Annu. Rev. Fluid Mech.* **16** (1), 263–285.

GOLDSTEIN, M. E. & HULTGREN, L. S. 1988 Nonlinear spatial evolution of an externally excited instability wave in a free shear layer. *J. Fluid Mech.* **197**, 295–330.

GOLDSTEIN, M. E. & LEIB, S. J. 1988 Nonlinear roll-up of externally excited free shear layers. *J. Fluid Mech.* **191**, 481–515.

GOLDSTEIN, M. E. & LEIB, S. J. 1989 Nonlinear evolution of oblique waves on compressible shear layers. *J. Fluid Mech.* **207**, 73–96.

GUDMUNDSSON, K. & COLONIUS, T. 2011 Instability wave models for the near-field fluctuations of turbulent jets. *J. Fluid Mech.* **689**, 97–128.

HABERMAN, R. 1972 Critical layers in parallel shear flows. *Stud. Appl. Maths* **51**, 139–161.

HALL, P. & SHERWIN, S. 2010 Streamwise vortices in shear flows: harbingers of transition and the skeleton of coherent structures. *J. Fluid Mech.* **661**, 178–205.

HAYNES, P. H. & COWLEY, S. J. 1986 The evolution of an unsteady translating nonlinear Rossby-wave critical layer. *Geophys. Astrophys. Fluid Dyn.* **35** (1–4), 1–55.

HILEMAN, J. I., THUROW, B. S., CARABALLO, E. J. & SAMIMY, M. 2005 Large-scale structure evolution and sound emission in high-speed jets: real-time visualization with simultaneous acoustic measurements. *J. Fluid Mech.* **544**, 277–307.

HULTGREN, L. S. 1992 Nonlinear spatial equilibration of an externally excited instability wave in a free shear layer. *J. Fluid Mech.* **236**, 635–664.

HUSSAIN, A. K. M. F. 1983 Coherent structures – reality and myth. *Phys. Fluids* **26**, 2816–2850.

HUSSAIN, A. K. M. F. & CLARK, A. R. 1981 On the coherent structure of the axisymmetric mixing layer: a flow-visualization study. *J. Fluid Mech.* **104**, 263–294.

HUSSAIN, A. K. M. F. & HASAN, M. A. Z. 1985 Turbulence suppression in free turbulent shear flows under controlled excitation. Part 2. Jet-noise reduction. *J. Fluid Mech.* **150**, 159–168.

HUSSAIN, A. K. M. F. & REYNOLDS, W. C. 1970 The mechanics of an organized wave in turbulent shear flow. *J. Fluid Mech.* **41**, 241–258.

HUSSAIN, A. K. M. F. & REYNOLDS, W. C. 1972 The mechanics of an organized wave in turbulent shear flow. Part 2. Experimental results. *J. Fluid Mech.* **54**, 241–261.

HUSSAIN, A. K. M. F. & THOMPSON, C. A. 1980 Controlled symmetric perturbation of the plane jet: an experimental study in the initial region. *J. Fluid Mech.* **100**, 397–431.

HUSSAIN, A. K. M. F. & ZAMAN, K. B. M. Q. 1981 The 'preferred mode' of the axisymmetric jet. *J. Fluid Mech.* **110**, 39–71.

HUSSAIN, A. K. M. F. & ZAMAN, K. B. M. Q. 1985 An experimental study of organized motions in the turbulent plane mixing layer. *J. Fluid Mech.* **159**, 85–104.

JACKSON, T. L. & GROSCH, C. E. 1989 *Effect of Heat Release and Equivalence Ratio on the Inviscid Spatial Stability of a Supersonic Reacting Mixing Layer*. Springer.

https://doi.org/10.1017/jfm.2019.909 Published online by Cambridge University Press

JEUN, J., NICHOLS, J. W. & JOVANOVIĆ, M. R. 2016 Input-output analysis of high-speed axisymmetric isothermal jet noise. *Phys. Fluids* **28** (4), 047101.

JORDAN, P. & COLONIUS, T. 2013 Wave packets and turbulent jet noise. *Annu. Rev. Fluid Mech.* **45**, 173–195.

JORDAN, P., ZHANG, M., LEHNASCH, G. & CAVALIERI, A. V. G. 2017 Modal and non-modal linear wavepacket dynamics in turbulent jets. In *23rd AIAA/CEAS Aeroacoustics Conference*. American Institute of Aeronautics and Astronautics.

JUVÉ, D., SUNYACH, M. & COMTE-BELLOT, G. 1980 Intermittency of the noise emission in subsonic cold jets. *J. Sound Vib.* **71** (3), 319–332.

KAWAHARA, G., UHLMANN, M. & VAN VEEN, L. 2012 The significance of simple invariant solutions in turbulent flows. *Annu. Rev. Fluid Mech.* **44** (1), 203–225.

KEARNEY-FISCHER, M., SINHA, A. & SAMIMY, M. 2013 Intermittent nature of subsonic jet noise. *AIAA J.* **51** (5), 1142–1155.

KERHERVÉ, F., JORDAN, P., CAVALIERI, A. V. G., DELVILLE, J., BOGEY, C. & JUVÉ, D. 2012 Educing the source mechanism associated with downstream radiation in subsonic jets. *J. Fluid Mech.* **710**, 606–640.

KERSWELL, R. R. 2005 Recent progress in understanding the transition to turbulence in a pipe. *Nonlinearity* **18** (6), R17–R44.

KIBENS, V. 1980 Discrete noise spectrum generated by acoustically excited jet. *AIAA J.* **18** (4), 434–441.

LEIB, S. J. 1991 Nonlinear evolution of subsonic and supersonic disturbances on a compressible free shear layer. *J. Fluid Mech.* **224**, 551–578.

LIU, J. T. C. 1974 Developing large-scale wavelike eddies and the near jet noise field. *J. Fluid Mech.* **62**, 437–464.

LIU, J. T. C. 1989 Cohenrent structures in transitional and turbulent free shear flows. *Annu. Rev. Fluid Mech.* **21**, 285–315.

MARASLI, B., CHAMPAGNE, F. H. & WYGNANSKI, I. J. 1989 Modal decomposition of velocity signals in a plane, turbulent wake. *J. Fluid Mech.* **198**, 255–273.

MARASLI, B., CHAMPAGNE, F. H. & WYGNANSKI, I. J. 1991 On linear evolution of unstable disturbances in a plane turbulent wake. *Phys. Fluids* **3**, 665–674.

MCKEON, B. J. 2017 The engine behind (wall) turbulence: perspectives on scale interactions. *J. Fluid Mech.* **817**, P1.

MCKEON, B. J. & SHARMA, A. S. 2010 A critical-layer framework for turbulent pipe flow. *J. Fluid Mech.* **658**, 336–382.

MEYER, T. R., DUTTON, J. C. & LUCHT, R. P. 2006 Coherent structures and turbulent molecular mixing in gaseous planar shear layers. *J. Fluid Mech.* **558**, 179–205.

MIKSAD, R. W. 1973 Experiments on nonlinear interactions in the transition of a free shear layer. *J. Fluid Mech.* **59**, 1–21.

MOORE, C. J. 1977 The role of shear-layer instability waves in jet exhaust noise. *J. Fluid Mech.* **80**, 321–367.

NICHOLAS, J. W. & LELE, S. K. 2011 Global modes and transient response of a cold supersonic jet. *J. Fluid Mech.* **669**, 225–241.

PAPAMOSCHOU, D. & ROSHKO, A. 1988 The compressible turbulent shear layer: an experimental study. *J. Fluid Mech.* **197**, 453–477.

PERSH, J. & LEE, R. 1956 Tabulation of compressible turbulent boundary layer parameters. *Tech. Rep.* NAVORD Rep. 4282 (Aeroballistic Res. Rep. 337), U.S. Naval Ordnance Laboratory.

RAGAB, S. A. & WU, J. L. 1989 Linear instability waves in supersonic turbulent shear layer. *AIAA J.* **27** (6), 677–686.

REYNOLDS, W. C. & HUSSAIN, A. K. M. F. 1972 The mechanics of an organized wave in turbulent shear flow. Part 3. Theoretical models and comparisons with experiments. *J. Fluid Mech.* **54**, 263–288.

ROBINSON, S. K. 1991 Coherent motions in the turbulent boundary layer. *Annu. Rev. Fluid Mech.* **23** (1), 601–639.

https://doi.org/10.1017/jfm.2019.909 Published online by Cambridge University Press

SAMIMY, M., KIM, J. H., KEARNEY-FISCHER, M. & SINHA, A. 2010 Acoustic and flow fields of an excited high Reynolds number axisymmetric supersonic jet. *J. Fluid Mech.* **656**, 507–529.

SAMIMY, M., REEDER, M. F. & ELLIOTT, G. S. 1992 Compressibility effects on large structures in free shear flows. *Phys. Fluids* A **4** (6), 1251–1258.

SANDHAM, N. D., MORFEY, C. L. & HU, Z. W. 2006 Sound radiation from exponentially growing and decaying surface waves. *J. Sound Vib.* **294** (1–2), 355–361.

SANDHAM, N. D. & REYNOLDS, W. C. 1991 Three-dimensional simulations of large eddies in the compressible mixing layer. *J. Fluid Mech.* **224**, 133–158.

SANDHAM, N. D. & SALGADO, A. M. 2008 Nonlinear interaction model of subsonic jet noise. *Phil. Trans. R. Soc. Lond.* A **366** (1876), 2745–2760.

SASAKI, K., CAVALIERI, A. V. G., JORDAN, P., SCHMIDT, O. T., COLONIUS, T. & BRÈS, G. A. 2017 High-frequency wavepackets in turbulent jets. *J. Fluid Mech.* **830**, R2.

SCARANO, F. & VAN OUDHEUSDEN, B. W. 2003 Planar velocity measurements of a two-dimensional compressible wake. *Exp. Fluids* **34** (3), 430–441.

SCHLICHTING, H. 1979 *Boundary-layer Theory*, 7th edn. McGraw Hill.

SCHMIDT, O. T., TOWNE, A., COLONIUS, T., CAVALIERI, A. V. G., JORDAN, P. & BRÈS, G. A. 2017 Wavepackets and trapped acoustic modes in a turbulent jet: coherent structure eduction and global stability. *J. Fluid Mech.* **825**, 1153–1181.

SHARMA, A. S. & MCKEON, B. J. 2013 On coherent structure in wall turbulence. *J. Fluid Mech.* **728**, 196–238.

SINHA, A., RODRÍGUEZ, D., BRÈS, G. A. & COLONIUS, T. 2014 Wavepacket models for supersonic jet noise. *J. Fluid Mech.* **742**, 71–95.

SPARKS, C. A. & WU, X. 2008 Nonlinear development of subsonic modes on compressible mixing layers: a unified strongly nonlinear critical-layer theory. *J. Fluid Mech.* **614**, 105–144.

SUPONITSKY, V., SANDHAM, N. D. & MORFEY, C. L. 2010 Linear and nonlinear mechanisms of sound radiation by instability waves in subsonic jets. *J. Fluid Mech.* **658**, 509–538.

SUZUKI, T. & COLONIUS, T. 2006 Instability waves in a subsonic round jet detected using a near-field phased microphone array. *J. Fluid Mech.* **565**, 197–226.

TAM, C. K. W. 1991 Broadband shock-associated noise from supersonic jets in flight. *J. Sound Vib.* **151** (1), 131–147.

TAM, C. K. W. & BURTON, D. E. 1984 Sound generated by instability waves of supersonic flow. Part 2. Axisymmetric jets. *J. Fluid Mech.* **138**, 273–295.

TAM, C. K. W. & MORRIS, P. J. 1980 The radiation of sound by the instability waves of a compressible plane turbulent shear layer. *J. Fluid Mech.* **98**, 349–381.

THUROW, B., SAMIMY, M. & LEMPERT, W. 2003 Compressibility effects on turbulence structures of axisymmetric mixing layers. *Phys. Fluids* **15** (6), 1755–1765.

TISSOT, G., ZHANG, M., LAJÚS, F. C., CAVALIERI, A. V. G. & JORDAN, P. 2016 Sensitivity of wavepackets in jets to nonlinear effects: the role of the critical layer. *J. Fluid Mech.* **811**, 95–137.

TOWNE, A., COLONIUS, T., JORDAN, P., CAVALIERI, A. V. & BRÈS, G. A. 2015 Stochastic and nonlinear forcing of wavepackets in a Mach 0.9 jet. In *21st AIAA/CEAS Aeroacoustics Conference*. American Institute of Aeronautics and Astronautics.

VAN DRIEST, E. R. 1951 Turbulent boundary layer in compressible fluids. *J. Aero. Sci.* **18** (3), 145–160; 216.

WU, X. 2005 Mach wave radiation of nonlinearly evolving supersonic instability modes in shear layers. *J. Fluid Mech.* **523**, 121–159.

WU, X. 2011 On generation of sound in wall-bounded shear flows: back action of sound and global acoustic coupling. *J. Fluid Mech.* **689**, 279–316.

WU, X. 2019 Nonlinear theories for shear-flow instabilities: physical insights and practical implications. *Annu. Rev. Fluid Mech.* **51**, 421–485.

WU, X. & HOGG, L. W. 2006 Acoustic radiation of Tollmien–Schlichting waves as they undergo rapid distortion. *J. Fluid Mech.* **550**, 307–347.

WU, X. & HUERRE, P. 2009 Low-frequency sound radiated by a nonlinear modulated wavepacket of helical modes on a subsonic circular jet. *J. Fluid Mech.* **637**, 173–211.

https://doi.org/10.1017/jfm.2019.909 Published online by Cambridge University Press

WU, X. & TIAN, F. 2012 Spectral broadening and flow randomization in free shear layers. *J. Fluid Mech.* **706**, 431–469.

WU, X. & ZHOU, H. 1989 Linear instability of turbulent boundary layer as a mechanism for the generation of large scale coherent structures. *Chinese Sci. Bull.* **34** (20), 1685–1688.

WU, X. & ZHUANG, X. 2016 Nonlinear dynamics of large-scale coherent structures in turbulent free shear layers. *J. Fluid Mech.* **787**, 396–439.

WYGNANSKI, I. J. & PETERSEN, R. A. 1987 Coherent motion in excited free shear flows. *AIAA J.* **25**, 201–213.

ZAMAN, K. B. M. Q. 1985 Far-field noise of a subsonic jet under controlled excitation. *J. Fluid Mech.* **152**, 83–111.

ZAMAN, K. B. M. Q. & HUSSAIN, A. K. M. F. 1980 Vortex pairing in a circular jet under controlled excitation. Part 1. General jet response. *J. Fluid Mech.* **101**, 449–491.

https://doi.org/10.1017/jfm.2019.909 Published online by Cambridge University Press